



**HAL**  
open science

# Development and application of optical diagnostic techniques for assessing the effects of preferential evaporation of multi-component fuels under engine-relevant conditions

Lama Itani

► **To cite this version:**

Lama Itani. Development and application of optical diagnostic techniques for assessing the effects of preferential evaporation of multi-component fuels under engine-relevant conditions. Electric power. Université Paris Saclay (COMUE); Universität Duisburg-Essen, 2015. English. NNT : 2015SACL018 . tel-01304205

**HAL Id: tel-01304205**

**<https://theses.hal.science/tel-01304205>**

Submitted on 19 Apr 2016

**HAL** is a multi-disciplinary open access archive for the deposit and dissemination of scientific research documents, whether they are published or not. The documents may come from teaching and research institutions in France or abroad, or from public or private research centers.

L'archive ouverte pluridisciplinaire **HAL**, est destinée au dépôt et à la diffusion de documents scientifiques de niveau recherche, publiés ou non, émanant des établissements d'enseignement et de recherche français ou étrangers, des laboratoires publics ou privés.

NNT: 2015SACL018



THESE DE DOCTORAT  
DE  
L'UNIVERSITE DE DUISBURG  
ET DE  
L'UNIVERSITE PARIS-SACLAY PREPAREE A  
CENTRALESUPELEC

ECOLE DOCTORALE N° 579  
Sciences Mécaniques et Énergétiques, Matériaux et Géosciences

Spécialité de doctorat : Energétique

Par

**Mme Lama ITANI**

**Development and application of optical diagnostic techniques for assessing  
the effects of preferential evaporation of multi-component fuels under  
engine-relevant conditions**

**Thèse présentée et soutenue à Duisbourg, le 14 décembre 2015 :**

**Composition du Jury :**

Christof SCHULZ	Professeur, Université de Duisbourg-Essen	Directeur de thèse
Gilles BRUNEAUX	Expert, IFPEN	Directeur de thèse
Frédéric GRISCH	Professeur, INSA Rouen	Rapporteur
Fabrice FOUCHER	Professeur, Université d'Orléans	Rapporteur
Sebastian KAISER	Professeur, Université de Duisbourg-Essen	Examineur

**Titre :** Development and application of optical diagnostic techniques for assessing the effects of preferential evaporation of multi-component fuels under engine-relevant conditions

**Mots clés :** jet, essence, LIF, multi-composants, évaporation

**Résumé :** Dans le cadre de cette thèse, une technique de diagnostic optique a été développée pour mesurer simultanément l'évaporation différentielle, la distribution de température, et la concentration massique de fuel dans un jet multi-composant. Cette technique a été examinée dans les conditions d'un moteur essence. La technique de mesure est basée sur l'utilisation des deux traceurs excités par une seule longueur d'onde.

Pour pouvoir examiner l'évaporation différentielle d'un carburant multi-composant, deux traceurs ont été sélectionnés : le p-difluorobenzène et le 1-méthyl-naphtalène. Ces traceurs reproduisent deux types de volatilité : faible et moyenne à élevée. Les traceurs choisis fluorescent dans deux régions spectrales distinctes ce qui rend l'application de cette technique possible. Une étude photophysique a été menée pour caractériser les deux traceurs, indépendamment puis en mélange, pour différentes conditions de pression, température, et composition du bain gazeux. L'étude photophysique est essentielle pour pouvoir mesurer quantitativement l'évaporation différentielle. Les résultats photophysiques montrent que le spectre du 1-méthyl-naphtalène est sensible à la température. Cette caractéristique permet de mesurer la distribution en température dans le jet.

Les essais ont été réalisés dans une cellule haute pression / haute température, capable de simuler les conditions d'un moteur thermique. Des sprays générés par un injecteur ECN Spray G et un piézo-électrique d'une ouverture annulaire ont été étudiés. Des mesures initiales ont été menées avec chaque traceur pour pouvoir fixer la proportion de mélange des traceurs. La précision de la méthode de mesure a été calculée suivant une configuration de filtres identiques. Ensuite, les champs de température calculés par la LIF et ceux déterminés depuis les champs de concentration massique, ont été comparés. Les résultats démontrent que la température est homogène ce qui signifie que les mesures d'évaporation différentielle n'ont pas influencé par la distribution de température dans le jet.

Les images obtenues en détectant les signaux depuis le mélange de traceurs ont permis de localiser l'évaporation différentielle. Une variation en distribution spatiale des composants est observée 550–600 K. Cet effet disparaît en augmentant la température, ce qui explique que l'évaporation est plus rapide à haute température. La localisation de l'évaporation différentielle varie avec le type d'injecteur. La géométrie du nez ainsi que la structure du jet a donc un impact sur la formation du mélange.

**Title :** Development and application of optical diagnostic techniques for assessing the effects of preferential evaporation of multi-component fuels under engine-relevant conditions

**Keywords:** jet, gasoline, LIF, multi-component, evaporation

**Abstract:** A non-intrusive quantitative laser-induced fluorescence (LIF) technique capable of simultaneously measuring preferential evaporation, temperature distribution, and fuel-mass concentration across a multi-component vaporized spray has been developed and investigated under engine-relevant conditions. The measurement technique is based on two-tracer LIF with single wavelength excitation.

To assess preferential evaporation, a tracer pair with suitable co-evaporation and spectral properties was selected based on vapor-liquid equilibrium calculations representative for gasoline fuels. Evaporation studies have shown that one tracer (p-difluorobenzene) co-evaporates with the high-to-medium-volatility end of the multi-component fuel while the other (1-methylnaphthalene) co-evaporates with the low-volatility end. For quantitative measurements the photo-physical properties of both tracers (each tracer separately and the combined tracers) were determined under a wide range of pressure, temperature, and bath-gas composition conditions. 1-Methylnaphthalene LIF shows a strong red-shift with temperature which enables measurements of the temperature distribution across the spray.

Spray evaporation and vapor mixing experiments were performed in a high-pressure high-temperature vessel capable of simulating in-cylinder conditions. An ECN Spray-G and a

piezo-electric outward opening injector were used in this study. Initial measurements were carried out with each tracer added separately to the fuel to assess signal cross-talk and to determine the best tracer concentrations. Once the proportions were determined, accuracy and precision of the method were calculated from the LIF-signal ratio of spray images within identical spectral bands. Temperature fields, obtained by two-color 1-methylnaphthalene LIF and derived from fuel concentration maps based on the assumption of adiabatic evaporation, were examined for inhomogeneities in the area of interest since fluctuations potentially influence the two-color method. It was shown that the temperature is homogeneous in the measurement volume.

To localize preferential evaporation, two-color two-tracer LIF images were evaluated. Taking into account the measurement accuracy and precision, variations in the spatial distribution of the fuel volatility classes were observed for 550–600 K. At higher temperatures, the effect is less pronounced, which is consistent with the fact that evaporation is faster. The localization of preferential evaporation varied with each injector used indicating the impact of injector nozzle geometry and jet structure on mixture formation.

**Titel :** Entwicklung und Anwendung optischer Diagnostiktechniken zur Untersuchung des Effektes der preferentialen Verdampfung von multikomponenten Kraftstoffen unter motorisch-relevanten Bedingungen

**Stichwörter:** Strahl, Benzin, LIF, multikomponenten, Verdampfung

**Kurzfassung:** Eine berührungsfreies quantitatives Verfahren auf Basis von laserinduzierter Fluoreszenz (LIF) wurde entwickelt, um simultan präferenzielle Verdampfung, Temperaturverteilung und Kraftstoffkonzentration im verdampften Bereich eines Mehrkomponenten-Kraftstoffsprays unter motorrelevanten Bedingungen zu messen. Verfahren beruht auf Zwei-tracer-LIF mit Anregung mit einem Laser.

Es wurde ein Tracer-Paar mit geeigneten Verdampfungs- und spektralen Eigenschaften auf Basis von Dampf-Flüssigkeits-Gleichgewichtsrechnungen für Otto-Kraftstoffe ausgewählt. Verdampfungsmessungen haben gezeigt, dass ein Tracer (p-Difluorbenzol) gleichzeitig mit dem mittel- und höherflüchtigen Siedeklassen verdampft, während der andere (1-Methylnaphthalin) den schwerflüchtigen Komponenten folgt. Für quantitative Messungen wurden die photophysikalischen Eigenschaften beider Tracer (einzeln und als Kombination) in einem weiten Bereich von Druck, Temperatur und Gaszusammensetzung bestimmt. 1-Methylnaphthalin-LIF zeigt eine starke Rotverschiebung mit der Temperatur, die Messungen der Temperaturverteilung ermöglicht.

Es wurde ein Tracer-Paar mit geeigneten Verdampfungs- und spektralen Eigenschaften auf Basis von Dampf-Flüssigkeits-Gleichgewichtsrechnungen für Otto-Kraftstoffe ausgewählt. Verdampfungsmessungen haben gezeigt, dass ein Tracer (p-Difluorbenzol) gleichzeitig mit dem mittel- und höherflüchtigen Siedeklassen verdampft, während der andere (1-Methylnaphthalin) den schwerflüchtigen Komponenten folgt. Für quantitative Messungen wurden die photophysikalischen Eigenschaften beider Tracer (einzeln und als Kombination) in einem weiten Bereich von Druck, Temperatur und Gaszusammensetzung bestimmt. 1-Methylnaphthalin-LIF zeigt eine starke Rotverschiebung mit der Temperatur, die Messungen der Temperaturverteilung ermöglicht.

**This thesis is submitted in fulfilment of the requirements for the degrees Doctor of Philosophy (CentraleSupélec) and Dr.-Ing. (University of Duisburg-Essen) in a joint dissertation program between University of Duisburg-Essen and CentraleSupélec.**

## Acknowledgements

**“It doesn’t matter how beautiful your theory is, it doesn’t matter how smart you are. If it doesn’t agree with experiment, its wrong.” ~Richard Feynman**

So, this is it! My PhD journey has finally come to an end. And yes, it has been definitely a journey like no other indeed, or more like a rollercoaster ride if you might ask me. This ride has not been easy, it has been filled with ups and downs, highs and lows, thrills and scares but towards the end you manage to get off of it feeling a lot stronger, a tad wiser, and surely humbler.

I want to start off by thanking my parents, mom and dad, for their unconditional support and their firm belief in the power of education. My brothers, whom regardless of their constant mockery of my nerdy side still think the world of me. My sister, Nadine, whom I believe has helped in shaping my character in every way possible. Throughout this PhD she has been nothing but my #1 supporter and for that I’ll be forever thankful.

Another group of people that I would like to thank is my co-musketeers at IFPE. I’ll start with Federico and Haïfa who managed to put up with me for the past three years. You guys have definitely put some color into my gloomy days ☺. I won’t forget to thank Sophie and Betty for their genuine kindness and their support through tough times. Big thanks to Karl and Mickael, aka “the chemists”, for their quirky sense of humor and their constant reminder that combustion is chemistry! I won’t forget to thank my “one of a kind” PhD WhatsApp group which includes Elias, Benjamin, Valerio, Eleferis and once again Federico and Karl. In this group we exchanged thoughts about everything BUT science which ended up making discussions comical. I don’t want to leave out my co-works at Duisburg who also made the year I spent in Germany a very enriching experience. Simon, thank you for your patience, support, and professional input on my PhD work. Thorsten, thank you for being my photophysics guru during the experimental campaign that we performed together.

And of course, it didn’t slip my mind to thank my advisors! Christof, you are definitely my definition of a perfectionist. Working with you have taught me to be meticulous. Thank you for your patience and I’m sorry if I gave you a hard time with my manuscript ☺. Gilles, thank you for being the voice of reason and for being my mentor throughout my research work. This work and this whole experience wouldn’t have been the same without you ☺. A huge thanks to Clément and Laurent for helping out with my experiments. My gasoline sprays wouldn’t have looked so “bright” without your assistance! A special thanks to the CORIA team, particularly Bjorn Rossow, for sharing his experimental findings and expertise with me.

I would also like to extend my gratitude to the jury members for taking the time to examine my research work.

## Table of contents

Abstract .....	vi
Kurzfassung.....	vi
Résumé .....	vi
Acknowledgements.....	vi
List of abbreviations.....	ix
List of symbols.....	x
1 Introduction.....	1
2 Background .....	3
2.1 Importance of fuel/air mixing in internal combustion engines.....	3
2.1.1 Injection systems and injector technology .....	3
2.1.2 Evaporation and mixing effects of multi-component fuels .....	8
2.2 Laser-based combustion diagnostics .....	14
2.2.1 Overview of tracer-LIF diagnostics .....	14
2.2.2 Types of fluorescence tracers .....	15
2.2.3 Photophysics of fluorescence tracers .....	19
2.3 Scientific question and measurement strategy in this work.....	30
3 Photophysical measurements of <i>p</i> -difluorobenzene and 1-methylnaphthalene .....	33
3.1 Investigation of tracer fluorescence.....	33
3.1.1 Fluorescence lifetime measurements of <i>p</i> -DFB and 1-MN.....	33
3.1.2 Evaluation of effective fluorescence lifetime of tracers .....	37
3.1.3 Fluorescence spectra measurements of <i>p</i> -DFB and 1-MN .....	39
3.1.4 Evaluation of tracer fluorescence spectra.....	42
3.2 Spectroscopic characterization of tracers.....	44
3.2.1 <i>p</i> -Difluorobenzene.....	44
3.2.2 1-Methylnaphthalene.....	47
3.2.3 Tracer mixture .....	50
4 Quantitative two-tracer LIF for simultaneous imaging of preferential evaporation effects, temperature, and fuel concentration .....	52
4.1 Measurement strategy .....	52
4.1.1 Choice of injector technology .....	53
4.1.2 Choice of surrogate fuel and tracers.....	54
4.1.3 Operating conditions .....	56

4.1.4 Experimental and optical arrangement .....	59
4.2 Experimental methods and image post-processing .....	65
4.2.1 Normalization method to obtain spatially-resolved fuel concentration maps.....	65
4.2.2 Calculation of temperature fields based on an adiabatic mixing model.....	67
4.2.3 Simultaneously imaging of preferential evaporation and temperature using two-tracer LIF .....	69
4.2.4 Error assessment and system calibration .....	70
4.3 Results and discussion .....	74
4.3.1 Error Assessment.....	74
4.3.2 Spatially-resolved fuel concentration maps and their corresponding temperature fields .....	86
4.3.3 Impact of nozzle geometry on preferential evaporation and spray formation.....	107
4.3.4 Impact of temperature on preferential evaporation .....	111
4.3.5 Impact of density on preferential evaporation .....	114
5 Outlook .....	116
6 Conclusions .....	117
7 References .....	120

## List of abbreviations

Abs.	Absolute
1-MN	1-Methylnaphthalene
aSOI	After start of injection
a.u.	Arbitrary unit
BP	Bandpass
CEM	Controlled evaporator mixer
DI	Direct injection
DISI	Direct inject spark ignition
ECN	Engine combustion network
ISC	Intersystem crossing
FAR	Fuel/air ratio
FARLIF	Fuel/air-ratio laser-induced fluorescence
FRET	Fluorescence resonance energy transfer
HOMO	Highest occupied molecular orbitals
HPLC	High-pressure liquid chromatography
IC	Internal conversion
ICCD	Intensified charged coupled device
ICE	Internal combustion engine
KrF	Krypton Fluoride
LIEF	Laser-induced exciplex fluorescence
LFM	Liquid flow meter
LPG	Liquefied petroleum gas
Nd:YAG	Neodymium-doped yttrium aluminium garnet
Norm.	Normalized signal
PDF	Probability density function
<i>p</i> -DFB	<i>p</i> -Difluorobenzene
PFI	Port-fuel injection
UV	Ultra-violet
vol%	Volume percent
VR	Vibrational relaxation
VVT	Variable valve trains
SG-DISI	Spray-guided direct-injection spark-ignition
SMD	Small droplet diameter

## List of symbols

$\alpha$	Rotation angle
$C_{\text{fuel}}$	Fuel concentration
$c_{p,a}$	Specific heat of ambient gas at constant pressure
$c_{p,Fv}$	Ambient gas molar specific heat of the gas fuel
$c_{p,Fl}$	Ambient gas molar specific heat of the liquid fuel
$E$	energy
$E_{\text{laser}}$	Normalized fluence distribution
$\eta'$	Normalization factor
$FAR_m$	Fuel-air ratio by mass
$h$	Planck constant
$h_{v,T_{\text{ini}}}$	Latent heat of vaporization at $T_{\text{int}}$
$I_v$	Volume LIF-signal intensity
$k_{\text{abs}}$	Rate of evaporation
$k_{\text{coll}}$	Rate of vibrational relaxation
$k_{\text{fl}}$	Rate of spontaneous fluorescence
$k_{\text{IC}}$	Rate of internal conversion
$k_{\text{ISC}}$	Rate of intersystem crossing
$k_{\text{nr}}$	Rate of non-radiative depopulation process
$\tilde{k}_q$	Rate coefficient of collisional quenching
$k_{\text{tot}}$	Total rate of all depopulation processes of electronically excited state
$M_a$	Molar mass of air
$M_f$	Molar mass of fuel
$m_{\text{fuel}}$	Total injected fuel mass
$N$	Scaling factor
$n_q$	Number density of quenching species
$R$	Ideal gas constant
$R$	Ratio
$S_{\text{fl}}$	Absolute LIF signal
$S_{\text{fl}}^0$	Fluorescence signal intensity in the absence of collisional quenching
$T$	Temperature
$\mathbf{T}$	Transformation matrix
$T_{\text{thermocouple}}$	Temperature measured by thermocouples
$T_{\text{jet}}$	Jet temperature
$T_{\text{amb}}$	Ambient temperature

$T_{\text{mix}}$	Adiabatic mixing temperature
$T_{\text{int}}$	Intermediate temperature at which the fuel vaporizes
$T_{\text{Fl,ini}}$	Initial temperature of the liquid fuel
$t_x$	Horizontal translation scalar
$t_y$	Vertical translation scalar
$\sigma_T$	Temperature precision
$\sigma_R$	Standard deviation derived from a LIF-ratio image
$\Phi_{\text{fl}}$	Fluorescence quantum yield
$\Omega/4\pi$	Solid angle of detection
$\tau_{\text{eff}}$	Effective lifetime
$\tau_{\text{rad}}$	Radiative lifetime
$Z_{\text{coll}}$	Collision rate



# 1 Introduction

To achieve fuel-efficient low-emission internal combustion engines, a detailed understanding of the physical processes occurring in the combustion chamber is required. Acquiring knowledge regarding mixture formation, combustion, and pollutant formation is essential for advancing the design of the combustion chamber and optimizing engine operation. An improved understanding of these processes can also assist in further improving the predictive quality of numerical simulations. These objectives can be met by performing quantitative measurements under conditions similar to real-life conditions (i.e., high pressure, high temperature, realistic fuel composition, and injection duration, etc.).

Laser-based methods have been supplying combustion research with non-intrusive, *in situ*, spatially- and temporally-resolved measurements of numerous quantities related to internal combustion engines. Mixture formation is one of the most critical processes that take place in internal combustion engines because the resulting mixture composition plays an important role in ignition, combustion, and pollutant formation. Mixture formation is not only influenced by the ambient conditions in the combustion chamber but also by the fuel composition. Different volatility groups of the fuel can evaporate at different time intervals and locations in the cylinder thus creating inhomogeneous distribution of the various fuel components. Controlling the mixing process and understanding the influence of the fuel composition allows us therefore to achieve substantial improvements in terms of reduced fuel consumption and engine-out raw emissions. The major challenge, however, is to perform highly precise measurements under engine-relevant conditions (i.e., unsteady and turbulent flows, elevated pressure, steep temperature gradients, etc.).

The objective of this PhD work is to develop a laser diagnostics technique capable of performing simultaneous quantitative imaging measurements of the effects of preferential evaporation, unburned gas temperature, and fuel mass concentration during the injection and evaporation of gasoline-like multi-component fuels. For this purpose, an equilibrium evaporation study was carried out aiming at formulating a multi-component surrogate fuel with evaporation characteristics similar to gasoline. Vapor-liquid equilibrium calculations also assisted in selecting a tracer pair with suitable co-evaporation properties. Note that these calculations were not carried out as a part of this work and therefore only their findings were reported here. After selecting the tracer pair, spectroscopic measurements were conducted to characterize each tracer over a wide range of engine-relevant conditions which later on allowed for quantitative diagnostics. The tracer mixture

was investigated for potential photophysical interaction influencing emission spectra and signal intensities. The knowledge acquired from the thermodynamic and spectroscopic study was used to design an optical diagnostics technique based on laser-induced fluorescence (LIF) that enables localizing two different volatility classes of the multi-component fuel and to simultaneously obtain the temperature and fuel mass distribution across the jet. Experiments were performed with two different types of fuel injectors for ambient densities and temperatures ranging between 3.5–12 kg/m<sup>3</sup> and 550–800 K respectively.

This thesis is organized in the following manner. A literature review (Chapter 2) covers injection systems and spray evaporation with the aim to demonstrate the influence of injection technology and spray break-up on the mixing process. Chapter 2 also addresses laser-induced fluorescence and its capabilities in investigating the evaporation and the mixing effects of multi-component fuels. The literature survey also includes a review of the photophysics of fluorescence tracers which is important to the interpretation of results obtained in chapter 3.

In chapter 3, results of photophysical properties of the two-tracers used in this work is presented. Characterizing the tracers over a wide range of relevant-engine conditions is essential for performing quantitative measurements.

Chapter 4 is divided into two main sections. Firstly, the experimental methodology based on two-tracer LIF is explained in details. This technique was used to localize the effects of preferential evaporation by calculating the ratio image based on the simultaneous detection of two fuel tracers in the vaporized spray. The ratio indicates where each tracer is located. Temperature assessment was carried out using two-color LIF while fuel mass concentration fields were calculated by a normalization method. Since the measurement technique is quantitative, a detailed description of the methodology behind quantifying measurement accuracy and precision is also addressed. Secondly, the experimental apparatus and the measurement conditions are presented. Results obtained from two different injector technologies under various relevant engine conditions are presented.

## **2 Background**

### **2.1 Importance of fuel/air mixing in internal combustion engines**

A systematic control of the mixture formation with modern high-pressure injection systems allows for considerable improvements of the combustion process in terms of reduced fuel consumption and engine-out raw emissions. However, because of the growing number of free parameters due to more flexible injection systems and technologies such as variable valve trains (VVT), the application of different combustion concepts within different regions of the engine map, etc., the prediction of spray and mixture formation becomes increasingly complex. For this reason, extensive work has been carried out to optimize the mixture formation and the combustion process in order to fulfill the requirements of current emission standards.

To improve the efficiency of the combustion process in an engine, the injection strategy is sought to be optimized thus resulting in an improved mixture formation. Nowadays in spark-ignition direct injection engines, researchers are seeking to generate a well-mixed and well-targeted spray in a short period of time. By doing so, a globally stratified environment can be achieved while keeping the conditions (i.e., temperature, fuel compositions, air/fuel ratio, etc.) within the spray vicinity as homogenous as possible. Therefore, the current injector geometries and systems require further development to answer to the demands on high-efficiency low-emission combustion.

In this section, injection systems and technologies will be discussed. Their influence on mixture formation and the combustion process will be also addressed. Two injector types, which were the focus of this research work, will be presented and their impact on spray geometry will also be discussed.

#### **2.1.1 Injection systems and injector technology**

The internal combustion engine (ICE) is the most important energy conversion system for the majority of vehicles. The application of the ICE is not restricted to on-road applications. It is widely used to power construction machines, agricultural vehicles, locomotives, and ships. Since ICEs will hold their leading position in the foreseeable future, tremendous efforts are made towards improving their efficiency to fulfill future emission legislations.

In order to lower engine raw emissions, new-exhaust gas after-treatment techniques and clean fuels (e.g., liquefied petroleum gas (LPG) and low-ethanol blend fuels) were developed. One important prerequisite to reducing emissions and to adjust to new fuels is to improve the mixture formation and the combustion concepts. Fuel injection has a strong impact on the mixture formation and thus, combustion. Therefore, a deeper insight is required regarding the capabilities of current injection systems. This section will shed the light on different types of injection systems employed in gasoline engines and their impact on mixture formation and combustion.

### Injection systems

There are two main injection techniques in gasoline engines: port fuel injection and direct injection. The port fuel injection technique is divided into two categories (single- and multi-point injection) depending on the position and the number of injectors used (cf. Figure 2-1).

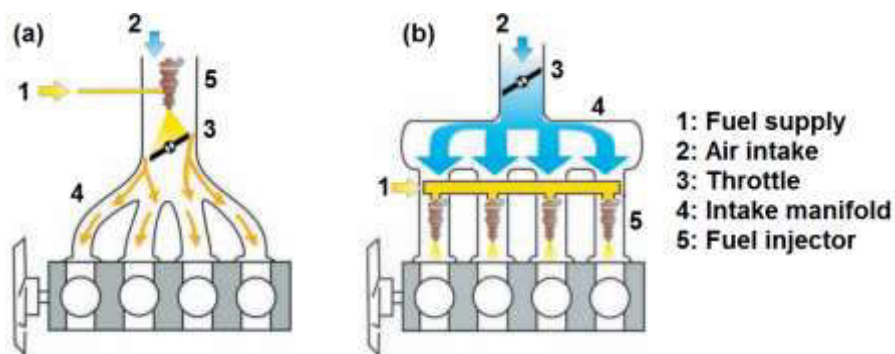


Figure 2-1: Schematics of a single-point (a) and a multi-point (b) port fuel injection system [1].

### Port fuel injection

For single-point injection, fuel is injected at a single point in the gas intake before a manifold distributes the mixture to the cylinders [1]. The injector is often mounted in the intake manifold runners, and the fuel remains there until one intake valve opens allowing the mixture to enter one cylinder. The fuel is partially deposited on the walls resulting in formation of liquid films. Therefore, changes in load result in variations of the wall-film thickness which consequently varies the fuel/air-mixture in quality and quantity during transient operation. Since the manifold is responsible for delivering the centrally prepared mixture to individual cylinders, it is often difficult to attain an equal distribution of the mixture in all cylinders. This is mainly due to the various parameters determining the

multiphase flow along the relatively long distance between the central injector and the cylinders and is also due to the complexity of the manifold geometry.

To overcome the non-uniform distribution of fuel into the individual cylinders, multi-point injection systems are used. Here, each cylinder has its own injector located upstream of the intake valve. The injection then takes place in the leg of the manifold that belongs to each individual cylinder. The mixture formation process for multi-point injection is similar to single-point injection and includes the evaporation of a wetted wall. However, the surface area of the fuel wall film is smaller for multi-point injection technique. This helps in precisely controlling the fuel quantity to the actual cycle which consequently improves fuel consumption and emission. The injectors used in port fuel injection systems have an injection pressure ranging between 5–15 bar.

### **Direct fuel injection**

The second injection technology is direct injection (DI) which is capable of enhancing the efficiency of the combustion process and thus decreasing CO<sub>2</sub> emissions. Common-rail injection systems are used in direct injection spark ignition (DISI) engines which are capable of providing a highly dispersed spray within the short time span available for spray disintegration and mixture formation inside the cylinder. In a DISI engine, injection takes place either during the intake stroke (homogenous mixture formation) or late during the compression stroke (stratified charge operation). The types of fuel injectors used for this injection technology will be discussed in the section below.

### **Injector technology**

Injectors exist in different nozzle types, yet, their basic operation remains the same. The spray structure, however, is highly influenced by the nozzle geometry, which also has a significant impact on the mixture formation. The two dominant types in current gasoline engines are solenoid multi-hole and piezo-actuated injectors. Multi-hole injectors generate full-cone sprays while piezo-actuated outward opening injectors result in hollow-cone sprays. In this section, the functionality and the spray shape of both types will be presented.

### **Solenoid multi-hole injector**

Figure 2-2 shows a schematic of a solenoid multi-hole injector. To maintain the injector closed, a spring presses the needle on the seal seat. To initiate injection, a current is supplied to the coil by a control unit which ascends the armature connected to the needle. A multi-hole injector is capable of generating a number of sprays with large droplet sizes

(SMD  $\sim 30 \mu\text{m}$  at 10 mm axial location from the nozzle exit [2]) and large penetration depths when spray injection takes place at a moderate liquid pressure in a at low gas density. Multi-hole injectors are widely used in a spray-guided DISI engine because the spray structure and cone angle remain intact with increasing back-pressure. However, a multi-hole injector produces a strongly inhomogeneous spray where fuel-rich spray plumes are separated by extremely lean regions. These inhomogeneities lead to large gradients in the burning velocity resulting in high pollutant emissions.

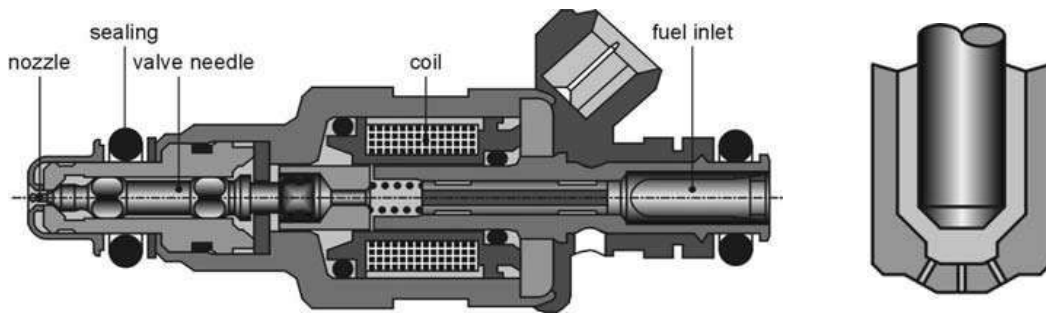


Figure 2-2: Schematics of a solenoid injector (left) and its multi-hole nozzle (right) [1].

Solenoid multi-hole injectors are characterized by having a full-cone spray structure (cf. Figure 2-3). Upon injection, the jet starts to break-up into a conical spray leading to large ligaments and droplets near the nozzle. This process is known as primary break-up. If injection pressure (of the liquid) is high, cavitation and turbulence are generated inside the injection holes. In the secondary break-up process, existing droplets become smaller due to aerodynamic forces that are induced by the relative velocity between the droplets and the ambient gases. Altogether, this results in a conical full-cone spray which is more and more diluted downstream the injector tip by air entrainment.

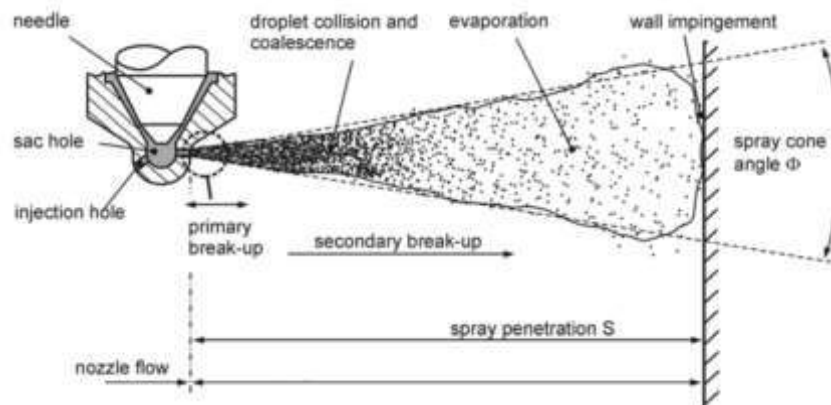


Figure 2-3: Break-up of a full-cone spray [1].

Note that in this work, a multi-hole ECN Spray G injector was used to visualize the mixture formation at different ambient pressures and temperatures (cf. section 4.1.3).

### Piezo-actuated outward opening injector

Piezo-actuated injectors have lately gained importance due to their high needle speeds and their accurate needle closing which helps in improving mixture formation. Unlike their solenoid counterparts, piezo injectors are capable of performing multiple injections with short injection timing. The piezo mechanism is based on the elongation of the piezo stack (Figure 2-4). The elongation is proportional to the voltage applied on the actuator, which allows fast and precise control.



Figure 2-4: Schematics of a directly-actuated piezo-electric outward-opening injector [3] (left) and of an outwardly opening nozzle [1].

There are two ways to control the needle, an indirect and a direct way. The advantage of direct needle actuation is the flexibility to attain partial needle lift that enables injection-rate shaping.

There are different nozzle geometries used in piezo injectors. Experiments in this work were performed with a directly actuated piezo-electric Bosch injector having an outward-opening nozzle. The injector characteristics are illustrated in [4]. An outward-opening nozzle produces a hollow-cone spray shape which is known for its short penetration depth, small droplet diameter ( $SMD \sim 10 \mu m$  [4]), and maximum dispersion (i.e. spray-cone angle) [5]. This consequently leads to fast evaporation and mixture formation.

The schematics of a hollow-cone spray formed by an outward-opening nozzle is given in Figure 2-5. The primary break-up of the spray is caused by turbulence and aerodynamic forces. A liquid film the forms as the spray departs from the nozzle, with an initial thickness  $h_s$  and a spray angle  $\alpha$  film becomes thinner due to the increasing radius and conservation of mass as it exits the nozzle. The secondary break-up is mainly due to aerodynamic forces which are similar to the ones described for the break-up mechanism of a full-cone spray. Droplet collisions can also occur in the spray because of the velocity difference between droplets. Since the spray is “hollow”, the area-to-volume ratio is higher than that of a full-cone spray leading to faster fuel/air mixing.

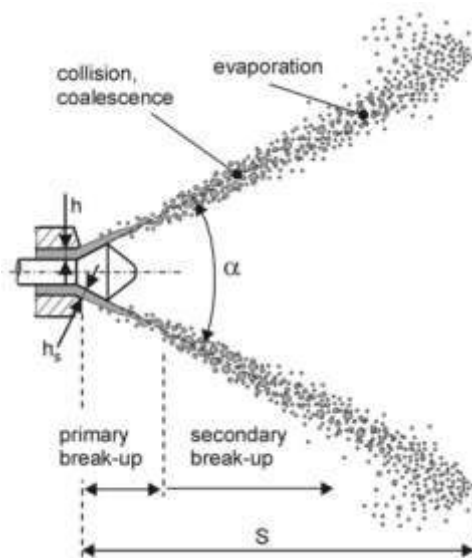


Figure 2-5: Break-up of a hollow-cone spray of an outward-opening nozzle [1].

### 2.1.2 Evaporation and mixing effects of multi-component fuels

To optimize the combustion process in spray-guided direct-injection spark-ignition engines (SG-DISI) it is important to acquire a detailed understanding of evaporation and mixing processes of gasoline sprays especially in complex high-pressure conditions. When describing the evaporation process of sprays, the first challenge is the choice of an adequate reference surrogate fuel that appropriately represents the relevant behavior of the real fuel with sufficient accuracy. Surrogate fuels are indispensable for quantitative measurements since commercial fuels contain numerous aromatic components which fluoresce simultaneously. However, each component in the commercial fuel has a fluorescence signal that depends on its concentration and also on temperature, pressure, and bath gas composition. The simultaneous detection of signal from various species

leads therefore to a complicated dependence of the integrated signal intensity on these variables. Signal can be used for qualitative imaging of the fuel cloud; quantitative interpretation of the signals is typically not feasible. Therefore, to perform quantitative analysis, it is preferred to introduce a well characterized (in terms of pressure, temperature, and bath gas composition) fluorescing trace into the surrogate fuel [6].

Surrogates are also preferred for simulations because they avoid handling the combined properties of hundreds of unknown species. In most spray experiments and CFD models, for instance, *iso*-octane ( $C_8H_{18}$ ) is primarily used to represent the relevant properties of gasoline. In reality, gasoline is comprised of almost 200 components [7]. This means that a single-component fuel (i.e., *iso*-octane) and a multi-component fuel (i.e., gasoline) do not undergo the same sub-processes during spray formation and evaporation, thus influencing ignition and combustion. Therefore, experiments and CFD simulations based on multi-component surrogate fuels are urgently required to enable a more realistic insight into the evaporation of gasoline fuel.

Efforts were made to formulate multi-component fuels with evaporation characteristics similar to gasoline. Styron et al. [8] developed a four-component fuel for Ford Motor Company and used this fuel for laser-induced exciplex fluorescence (LIEF) imaging in a port-fuel injection (PFI) engine. On the other hand, Scholz et al. [9] eliminated the less volatile component in standard gasoline and applied the gasoline in fuel/air-ratio measurement by LIF (FARLIF) which is based on quenching by oxygen. These studies focused on the comparison between the formulated multi-component fuels and real gasoline.

To understand the evaporation behavior of multi-component fuels and assess the effect of fuel properties on spray formation, Zigan et al. [10] analyzed the influence of different fuel components on spray formation of a hollow-cone piezo injector using Mie-scattering and LIF imaging. Experiments were conducted in a high-pressure high-temperature pre-combustion vessel at 15 bar and 473 K ambient pressure and temperature respectively. *iso*-octane and *n*-heptane were used as single-component fuels while a three-component fuel composed of 35 vol% *n*-hexane, 45 vol% *n*-heptane, and 25 vol% *n*-decane was used as a multi-component fuel. It was observed that single-component fuels could not sufficiently reproduce the gasoline spray structure, in particular, the spray shape. The fuel viscosity was found to influence the injection and the atomization process. Single-component fuels resulted in a finer spray with a droplet size distribution concentration

shifting towards smaller droplets. This observation does not apply for the multi-component fuel where sprays were found to have a larger droplet size and a higher momentum due to the presence of low-volatility component. For LIF experiments, 3-pentanone was used as tracer since its boiling point is comparable with *n*-heptane which makes up almost half of the multi-component fuel. LIF measurements showed signs of demixing (i.e., as a consequence of sequential evaporation of different fuel components from the spray). This proves the need of enhanced models capable of properly simulating the evaporation of multi-component fuels.

The influence of multi-component fuels on the mixing processes was studied by Kelly-Zion et al. [11] who used laser-induced-excimer fluorescence (LIEF) imaging to quantitatively investigate the mixing process and the vapor distribution of low- and high-volatility components in a port-injected SI engine. The experiments performed at early injection conditions showed that most of the liquid fuel entering the cylinder is composed of the low-volatility component implying that the high-volatility fuel component was initially released in the suction duct. This proves that low- and high-volatility ends of the fuel evaporate at different times and locations in the cylinder. The results presented in Ref. [11] also showed that large-scale gas motion that is induced during intake is critical for good mixing during the intake and compression strokes. High intake port velocity is important for initial droplet atomization, but does not guarantee complete mixing. This work, however, did not provide an accurate representation of both liquid and vapor phases of the fuel and both its light and heavy ends which is essential for drawing accurate conclusions from fuel distribution data.

Han and Steeper [12] analyzed the mass evaporation rate at early and late injection timings. Experiments showed that early injection timings promote homogenous air/fuel mixtures while late timings are characterized by incomplete mixing at ignition. Experiments were carried out with cyclohexane (mixture 2 in Figure 2-6) and a fuel mixture composed of 20 vol% cyclopentane and 70 vol% *iso*-octane (mixture 1). These mixtures represent exemplary single and two-component fuels respectively. Tracers were selected and matched to their corresponding components by matching boiling points. The two-component fuel was doped with three tracers with different volatility that were chosen to appropriately track the mass evaporation rate of the fuel. Figure 2-6 shows the probability density functions (PDFs) of equivalence ratios recorded for both fuel mixtures at various start-of-injection (SOI) timings in a plane 11 mm below the spark plug for fuel mixtures 1 and 2. For early injection (cf. Figure 2-6a), the PDFs of equivalence ratios of the two mixtures show a very similar shape and width, with the peak of the distribution

being close to the mean implying uniform mixing. For late injection timing (cf. Figure 2-6b), the PDFs of mixture 1 and 2 at -180 CAD are broader than the ones obtained for early injection timings indicating less uniform mixing. This indicates that mixture 1 with its two fuel components suffers from incomplete mixing compared to the single-fuel mixture. It can be concluded that the low-volatility end in the fuel mixture limits the time available for the mixing process.

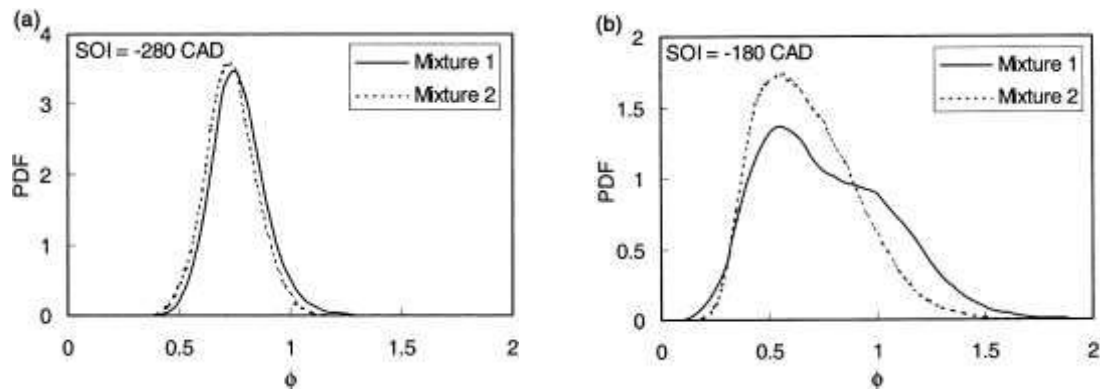


Figure 2-6: Probability density function (PDF) of equivalence ratios recorded at the time of ignition in a plane 11 mm below the spark plug for fuel mixtures 1 and 2. Two start-of-injection timings are presented: (a) SOI = -280 CAD and (b) SOI = -180 CAD. Each curve represents 32 LIF images.

Williams et al. [13] performed tracer-LIF imaging with a six-component fuel in a direct-injection engine. The fuel was composed of 30.4 vol% *n*-butane and *iso*-pentane (high-volatility group), 55 vol% *iso*-octane and *n*-octane (medium volatility group), and 14.6 vol% *iso*-dodecane and *n*-decane (low-volatility group) (the reference does not give numbers for the individual components). Three tracers were used to track the evaporation of the high, medium, and low-volatility group, respectively. This work was the first to introduce a co-evaporative fuel/tracer blend based on thermodynamic modeling rather than assuming that matching boiling points lead to a good representation of a fuel class by a specific tracer. However during measurements, the fuel was doped with one tracer at a time to avoid energy transfer between tracer classes. The measurements detected early inhomogeneity due to preferential evaporation initiated by the high-volatility fuel component. At later times of mixing, small differences in the spatial distribution of different volatility groups were identified. This is due to the long mixing time and the high turbulence for early injection operating points. However, introducing tracers separately and then observing the mixture formation based on single-tracer LIF does not provide a full knowledge of the mixing process.

Krämer et al. [14] imaged the fuel distributions of different volatility classes with three mixtures that contained combinations of two fluorescence tracers (toluene/acetone, *p*-xylene/acetone, and *p*-xylene/3-pentanone) that represented different volatility classes (i.e., high/medium, high/low, and medium/low, respectively). The tracers were matched to fuel components based on their boiling points. The selected tracers allowed to map low, medium, and high-volatility ends of the fuel and any combination of two classes. The experiments took place in a SI engine providing optical access. Instantaneous images showed that the distribution of different volatility classes may fluctuate significantly affecting the local mixing ratio and local gas composition. It was observed that the high-volatility fuel component mixes homogeneously early in the compression stroke. The medium and low-volatility components, however, were found to be strongly affected by the in-cylinder gas flow. It was mentioned that signal cross-talk between the tracers resulted in a 10% contribution of the aromatic tracer when collecting signal from the ketone which complicated the interpretation of the fuel distribution.

Until now, experiments performed in optical engines showed unanimously that preferential evaporation is more likely to take place at early injection conditions. It was seen that high- and low-volatility components may be potentially released at different times and locations in the cylinder. For late injection timings the fuel distribution in optical engines can be influenced by the turbulent cylinder flow which can lead to fast mixing of components thus resulting in co-evaporation of all volatility groups. High-pressure and high-temperature conditions (in late injection strategies) should be studied under constant injection conditions (i.e., in a high-pressure high-temperature pre-combustion vessel) where spray sub-processes can be investigated under well-controlled boundary conditions.

Egermann and Leipertz [15] examined the spray evaporation with Raman scattering for gasoline sprays in a high-temperature high-pressure constant volume chamber. The fuel was composed of 50 vol% benzene (as high-volatility component) and 50 vol% *n*-decane (as low-volatility component). Spray experiments, performed at 100 bar injection pressure, 30 bar ambient pressure, and 523 K ambient temperature, showed effects of preferential evaporation of the fuel components. Demixing is presented by a larger concentration of benzene evaporating at early observation times (i.e., 5 ms after start of injection). Consequently, a larger concentration of benzene was detected at the edge of the spray.

Myong et al. [16, 17] investigated the influence of multi-component fuels on spray penetration and spray angle by shadowgraphy and numerical simulations at 30 bar and 700 K. They found that the spray penetration depth and angle strongly depend on the fuel composition. In the case of non-evaporating sprays, the presence of high-volatility components increased the spray cone angle and decreased the penetration depth of the sprays. Numerical simulations showed that the fuel vapor distribution inside the spray is mainly influenced by low- and high-volatility components. The more volatile fuel component evaporated earlier and close to the nozzle where it was also found to be localized in the central portion of the spray. The less-volatile component was observed mainly around the spray tip.

Despite the numerous investigations aiming at increasing the knowledge of evaporation of multi-component fuels, there is still a lack of quantitative measurements of the mixture formation and evaporation for different injection regimes. This can hinder the validation of numerical models based on multi-component fuels consequently prohibiting the optimization of injection strategies. There is an ongoing need for an appropriate measurement strategy capable of observing mixture formation in non-fluorescing base fuels with well-characterized fluorescence tracers. The methodology developed in this work aims at localizing effects of preferential evaporation and at qualitatively determining the deviation from the case of equal distribution of the fuel components for gasoline-type fuels. The measurement strategy will be discussed in details in section 2.3.

## 2.2 Laser-based combustion diagnostics

Due to advances in laser technology and spectroscopy, laser-based diagnostics has become a powerful tool for characterizing the combustion process and analyzing non-reactive flows. Unlike physical probing, laser-based techniques enable non-intrusive *in situ* measurements in an environment with minimized interference between the environment and the measurement which makes it ideal for confined locations such as an ICE. Moreover, laser probing has no temperature threshold that limits its applicability. Temperature and species concentrations can be measured at high spatial and temporal resolution.

There is a number of techniques that permit temperature and species-concentration measurements such as Rayleigh scattering, spontaneous Raman scattering, coherent anti-Stokes Raman spectroscopy (CARS), and laser-induced fluorescence (LIF). It was argued that Rayleigh scattering requires no fuel tracer in order to quantify, for example, the composition of a fuel/air mixture for cases where the fuel-composition in the gas-phase does not vary [18]. Since the measurement methodology of this work is based on the use of multi-component surrogate fuels, Rayleigh scattering cannot be used for quantitative investigations of the mixing process. CARS, on the other hand, is also unsuitable for this work's measurement technique because it solely provides point-wise temperature measurements [19]. LIF can provide 2D images of two fuel components and temperature with high precision and accuracy [20–23]. LIF was thus considered to be more suitable for the objectives of this work. The methodology established in this work is solely based on tracer-LIF imaging measurements. Tracer-LIF diagnostics will be the only technique addressed in details in the overview section below.

### 2.2.1 Overview of tracer-LIF diagnostics

Laser-induced fluorescence is mostly applied to detect concentration [24, 25] and temperature [26–28] in a system of interest. A laser light-sheet can be formed thus illuminating a two-dimensional cross-section which is visualized by intensified charged-coupled device (ICCD) cameras.

Laser-induced fluorescence is initiated by absorption of laser light followed by spontaneous emission of fluorescence from electronically excited molecules or atoms. For most cases, excitation is in the ultraviolet and the subsequent emission occurs in the UV and visible spectral regions. The key to performing quantitative LIF measurements is to selectively detect the signal of a particular species. This, however, is considered unfeasible when measurements are performed using commercial fuels because they contain a large

number of fluorescing species. For quantitative investigations, these fuels are usually replaced by surrogates that have similar evaporation characteristics as the target commercial fuel. These surrogate fuels are transparent which means they emit either weak or no signal when exposed to laser light. Well-characterized fluorescing tracers can then be added to the surrogate fuels to enable quantitative measurements. These tracers should behave similarly to the fuel they are added to concerning spray formation, evaporation, convection, and diffusion. The choice of tracers depends on the application of the laser-induced fluorescence technique. For instance, if experiments are conducted with the intent to determine the temperature distribution across a gaseous flow, it is adequate to use a tracer that is characterized by a strong spectral red-shift with increasing temperatures therefore allowing for two-color LIF thermometry.

For quantitative measurements, the LIF-signal must be corrected for its dependence on local temperature, pressure, and bath gas composition. Therefore, the spectroscopic properties of the tracer must be known over a wide range of conditions.

### **2.2.2 Types of fluorescence tracers**

Tracer LIF has been widely used to investigate combustion processes and non-reactive flows. As discussed in section 2.2.1, tracers are selected based on their similarity of their combustion and gas-dynamics properties to those of the transparent surrogate fuel. For instance, a surrogate that simulate the evaporation of gasoline fuel is often doped with toluene as tracer due to the similarity in evaporation and combustion properties [26].

Organic molecules are vastly used as LIF tracers due their high vapor pressure which makes them good candidates for measurements carried out between room temperature and temperatures typical for the pre-combustion phase in engines. They absorb light in the UV spectral region and emit in the UV and visible region.

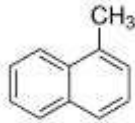
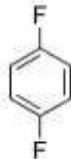
Aromatics and ketones are two groups of organic tracers that are frequently used for mixture diagnostics. The tracers that were used in this work were selected based on a thermodynamic model that simulates the evaporation of fuel components and their corresponding tracers based on the molecular structure of the components. Details of this procedure are explained in section 4.1.2. It was found that *p*-difluorobenzene and 1-methylnaphthalene co-evaporate with medium-to-high and low-volatility components respectively. The section below will describe only these two aromatic tracers which were in the focus of this work.

## Aromatics

### 1-Methylnaphthalene

1-Methylnaphthalene (1-MN) is frequently used as a tracer to study the evaporation of Diesel sprays [29, 30] since they both have similar physical properties which ensures co-evaporation. Information regarding the emission fluorescence spectra of 1-MN when excited at 266 nm were reported in [30]. Figure 2-7 shows that the fluorescence of 1-MN occurs between 310 and 400 nm, with a peak centered at around 340 nm. With increasing temperature, the emission spectrum red-shifts by about 1 nm/100 K. The full-width-half-maximum of the emission feature also increases with increasing temperature. The significant change of the shape and the position of the spectrum allows for temperature measurements by a single-tracer two-color detection technique where one optical filter selects the signal originating from the spectrum peak while another filter selects the signal from the long wavelength tail region. One drawback of 1-MN as tracer is the lack of absorption cross-section data available as a function of temperature which can pose limitations on quantitative measurements. Moreover, the spectral data presented in [30] are still insufficient to perform quantitative measurements. A full spectral characterization in a well-controlled environment of the tracer is necessary. Therefore, one of the objectives of this work was to spectrally characterize 1-MN as a function of temperature, pressure, and bath gas composition. Results will be reported in Chapter 3.

Table 2-1: Thermodynamic properties of 1-methylnaphthalene and *p*-difluorobenzene.

	1-Methylnaphthalene	<i>p</i> -Difluorobenzene
Chemical formula and structure	$C_{10}H_7CH_3$ 	$C_6H_4F_2$ 
Molar mass / (g/mol)	142.2	114.1
Boiling point at 1 bar / K	517.8	362
Vapor pressure at 293 K / mbar	0.06	62.61
Density at 293 K / (kg/m <sup>3</sup> )	1039	1110

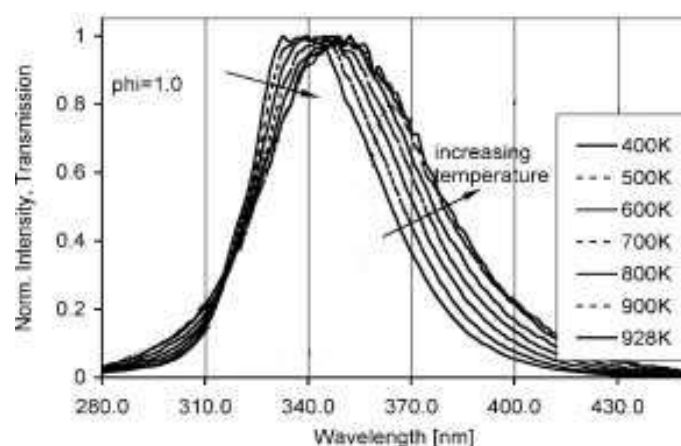


Figure 2-7: Normalized emission spectra of 1-MN in air for different temperatures [30].

### *p*-Difluorobenzene

Absorption cross-sections of *p*-difluorobenzene (*p*-DFB) were examined by Sponer [31] and Steer et al. [32] who investigated fluorescence quantum yields, fluorescence decay times, and emission fluorescence spectra. Steer's work highlighted the need for high-resolution time-resolved measurements of *p*-DFB fluorescence spectra by means of tunable ultraviolet laser excitation. Excitation and fluorescence emission spectra for varying ambient conditions have so far been unavailable. To exploit *p*-DFB as tracer for visualizing phenomena under engine-relevant conditions, a full characterization of the tracer is required. Measurements regarding the spectral characterization of *p*-DFB will be reported in Chapter 3.

### **Ketones**

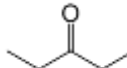
Unlike aromatics, the number of ketone tracers applicable to LIF is limited. Acetone and 3-pentanone are two common ketone tracers. The methodology of this work is based on the use of aromatics tracers in order to avoid energy transfer between tracers (cf., section 3.2.3), therefore, this section will be limited to discussing acetone and 3-pentanone since those two are often preferred because of their fluorescence emission in the visible spectral region, their insensitivity to quenching by molecular oxygen, and their non-toxicity [6].

#### *Acetone and 3-pentanone*

Acetone and 3-pentanone show similar photophysical characteristics, hence, they will be reviewed in this section simultaneously. In 1930, Matheson et al. [33] was the first to investigate the fluorescence of acetone and 3-pentanone. Regardless of similarities in

the photophysical behavior, these two tracers have different boiling point and vapor pressure hence influencing their practical applications. Acetone has a boiling point of 56°C which makes it adequate for tracing low gaseous flows [34]. 3-Pentanone, on the other hand, has a boiling point (101°C) close to typical gasoline surrogates (*iso*-octane: 110°C) which makes it appropriate for tracer LIF applied to SI engines [35]. Quantitative tracer-LIF measurements using acetone and 3-pentanone are possible because the absorption and fluorescence characteristics of these tracers have been thoroughly investigated [22, 36, 37].

Table 2-2 Thermodynamic properties of acetone and 3-pentanone

	Acetone	3-Pentanone
Chemical formula and structure	C <sub>3</sub> H <sub>6</sub> O 	C <sub>5</sub> H <sub>10</sub> O 
Molar mass (g/mol)	58.08	86.13
Boiling point at 1 bar (K)	329	373
Vapor pressure at 293 K (mbar)	245	46.66
Density at 293 K (kg/m <sup>3</sup> )	790	820

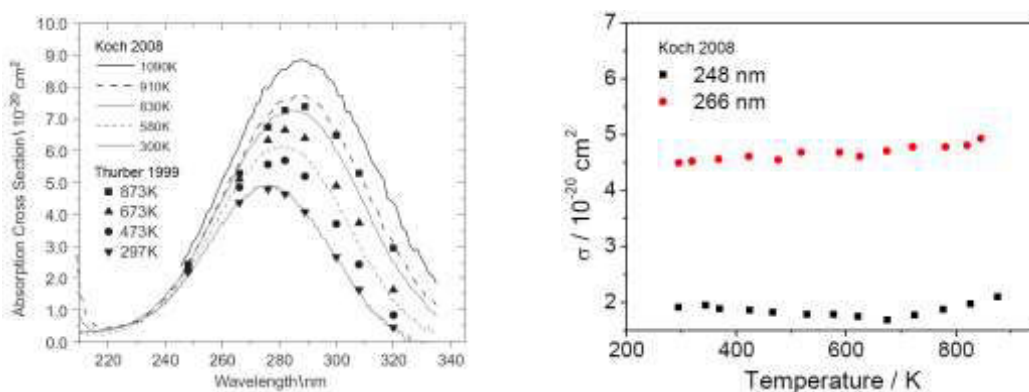


Figure 2-8: Acetone absorption spectra as a function of temperature (left, Koch et al. [38] and Thurber et al. [22]) and temperature-dependence of the absorption cross-section at 248 and 266 nm excitation (right, Koch et al. [38]).

Koch et al. [36] investigated the absorption cross-section of acetone for a wide range of temperatures. The absorption spectrum at 300 K (cf. Figure 2-8, left) has a peak centered at 275 nm and stretches from 230 to 330 nm which makes excitation possible with KrF\* excimer lasers at 248 nm and a frequency-quadrupled Nd:YAG lasers at 266 nm. The absorption spectrum red-shifts and broadens with increasing temperature. Figure 2-9

shows that the absorption cross-section is almost temperature-independent for 248 and 266 nm excitation. The temperature dependence of the absorption spectrum of 3-pentanone is comparable to that of acetone but with higher absolute values.

The emission spectra of acetone and 3-pentanone range from 340 to 540 nm. The profile of the fluorescence spectra of both tracers is almost identical [39]. Variations in temperature, pressure, and O<sub>2</sub> concentration do not have an influence on the spectral shape of the fluorescence spectra of both tracers. Therefore, ketones cannot be used for two-detection-color tracer LIF techniques which are based on the spectral red-shift and broadening. They have, however, been used for temperature measurements with quasi-simultaneous measurements with two excitation wavelengths. Ketones have fluorescence quantum yields that are two orders of magnitude below those of aromatics. The impact of temperature, pressure, and oxygen concentration for different excitation wavelengths was also investigated and results were reported in [40–42].

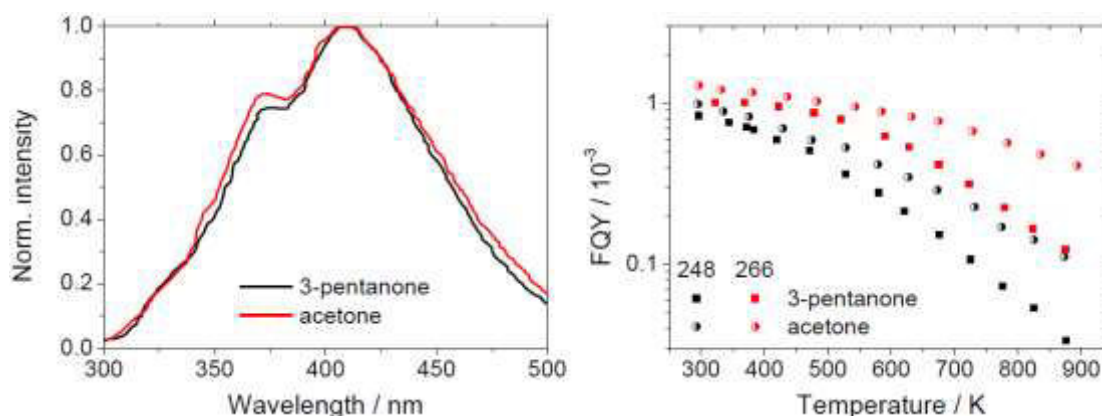


Figure 2-9: Normalized fluorescence spectra of acetone and 3-pentanone at 400 K after 266 nm laser excitation (left, [39]) and their variations in fluorescence quantum yield at 248 and 266 nm excitation wavelength (right, [22]).

### 2.2.3 Photophysics of fluorescence tracers

Fluorescence tracers are usually excited by nanosecond lasers in the UV region. Subsequent spontaneous emission (fluorescence) occurs usually on a timescale of about 1–200 ns. The fluorescence quantum yield and the emission spectra are strongly affected by thermodynamic conditions and potentially by the bath gas composition. To quantitatively interpret the emitted signal intensity, a detailed knowledge of the photophysical processes is required. In this chapter, the photophysics of organic tracers which were used in this work will be illustrated to support the interpretation of the results discussed in Chapter 3.

## Absorption

### *Classification of electronic transitions*

Absorption of UV photons by tracer molecules leads to population of excited electronic states. The magnitude of the absorption is described by the absorption cross-section  $\sigma(\lambda)$  which is wavelength-dependent. The absorbed photon energy promotes an electron from a bonding ( $\sigma$  or  $\pi$ ) or non-bonding ( $n$ ) orbital into one of the empty anti-bonding orbitals ( $\sigma^*$  or  $\pi^*$ ). Combinations of electronic transitions that might occur are described in Figure 2-10. In organic molecules, the bonding  $\sigma^*$ ,  $\pi^*$ , and  $n$  orbitals are considered highest occupied molecular orbitals (HOMO). On the other hand, anti-bonding  $\sigma^*$  and  $\pi^*$  are the lowest unoccupied molecular orbitals (LUMO).

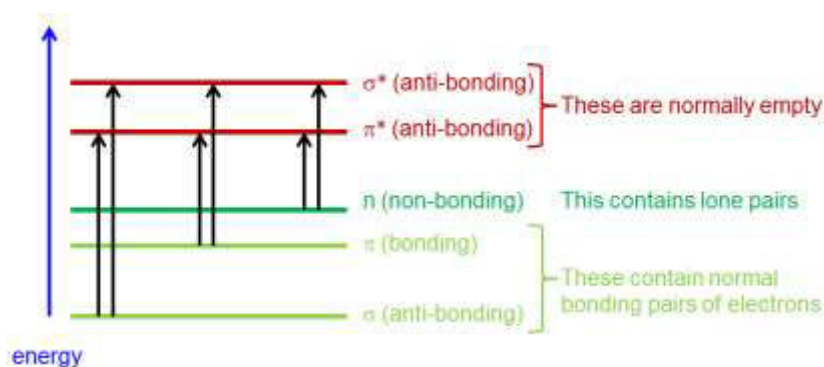


Figure 2-10: Schematics of different combinations of electronic transitions due to molecular excitation. The transitions are designated by arrows. The length of the arrow represents the energy used for transition.

### *Classification of electronic states*

The electronic state of a molecule is directly related to its total spin and the degree of excitation. The total spin for organic molecules in the ground state is  $S = 0$ . All electrons found in the same orbital are paired with an anti-parallel spin. When a single electron is excited, the two unpaired electrons can be either parallel ( $S = 1$ ) or anti-parallel ( $S = 0$ ). Based on the number of realization with the same total energy, also known as the multiplicity state, the  $S = 0$  and  $1$  states are called singlet (S) and triplet (T), respectively.

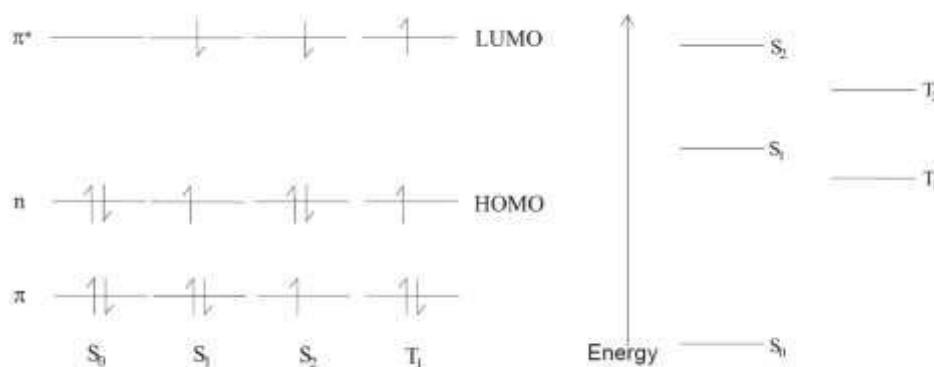


Figure 2-11: Population of the molecular orbitals in the ground state and the first excited state of a carbonyl group (left). The right panel compares the relative energy of various states [6].

Singlet and triplet states are numbered according to increasing energy with subscript numbers signifying the level of excitation. 0 is the ground state while 1 and 2 are excited states with increasing energy. Figure 2-11 shows the population and the energy of the ground state and the first excited states for a carbonyl group present in ketones.

#### *Deactivation of excited molecules*

When molecules are excited, highly excited states become populated. The excess energy from these states can be dissipated on different paths through physical and chemical (dissociation, photo-induced reaction) processes.

Physical processes are divided into three groups:

- Radiative process: All or part of the excess energy is emitted by spontaneous emission which is known as fluorescence
- Non-radiative process: The excess energy is thermalized by vibrational and rotational energy transfer
- Collisional quenching: Electronic excitation of colliding molecules (i.e., electronic energy transfer)

Figure 2-12 depicts the photophysical processes related to deactivation of excited molecules. Radiative and non-radiative processes are indicated by straight and curved lines respectively. An excited molecule can lose its energy either by emitting light (i.e., fluorescence and phosphorescence) or by exciting vibrations and rotations in colliding molecules (i.e., external vibrational relaxation, VR).

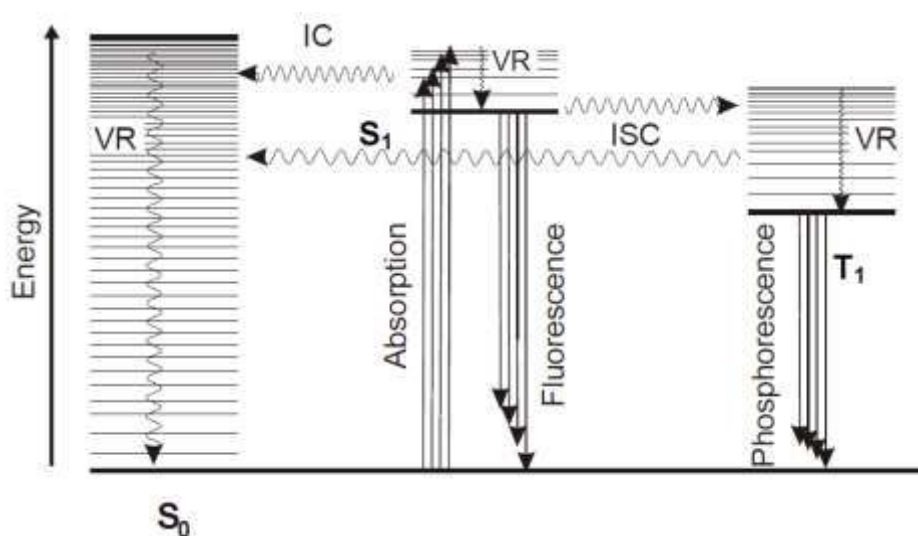


Figure 2-12: Jablonski diagram showing the photophysical processes during deactivation of excited organic molecules [6].

Intra-molecular electronic transitions take place without varying the total energy (horizontal arrows in Figure 2-12). When spin multiplicity is maintained, the process is called internal conversion (IC) and when spin multiplicity changes the process is referred to as intersystem crossing (ISC).

#### *Radiative process*

The rate of spontaneous emission depends on transition moments in the same way as the absorption cross-section and therefore obeys the same selection rules. When the energy difference between the coupled states is high, the probability of spontaneous emission increases.

- Fluorescence

The  $S_1 \rightarrow S_0$  transition due to spontaneous emission of light is fast. It is observed during a range of 1–100 ns. For instance in ketones, the  $S_1 \rightarrow S_0$  transition is symmetry- and orbital forbidden. The radiative lifetime is therefore of the order of  $\mu\text{s}$ . Intersystem crossing leads to a fast depopulation of the excited state thus limiting the effective fluorescence lifetime to  $\sim 1$  ns.

- Phosphorescence

Triplet states are significantly longer lived due to the spin-forbidden radiative relaxation to the singlet ground state. The intersystem crossing populating the  $S_0$  state is inefficient

due to the large energy difference. The spontaneous transition  $T_1 \rightarrow S_0$  is called phosphorescence and has a typical lifetime of ms to s.

#### *Non-radiative process*

- Transition probability

When the energy difference between quantum states is high, the transition probability of non-radiative relaxation processes, such as intersystem crossing and internal conversion, tends to be low. This large energy difference decreases the overlap of the vibrational energy wave functions. For this reason, ISC in simple ketones ( $\Delta E \sim 20$  kJ/mol (0.22 eV)) is faster than in toluene ( $\Delta E \sim 120$  kJ/mol (1.3 eV)). The background of the energy gap between triplet and singlet states will be discussed in the section below due to its importance in comprehending the quenching process.

- Singlet-triplet energy difference

In singlet and triplet systems having identical quantum numbers, the triplet is systematically lower in energy. This is directly related to Hund's rule which states that in open-shell systems the configuration with maximum spin multiplicity is favored. This effect can be explained by referring to Coulomb's law. For the case of maximum spin, the spin wave function is fully symmetric, and therefore, based on Pauli's law, the spatial wave function must be anti-symmetric. This implies for a symmetric case the mean distance between the electrons increases while the Coulomb forces decrease. This leads to an overall lower energy of the triplet compared to the singlet state.

The resulting energy difference relies on the electronic structure of the respective molecule. For single-ring aromatic molecules,  $\pi$  and  $\pi^*$  molecular orbitals have larger spatial overlap than  $n$  and  $\pi^*$  in ketones. This means that the Coulomb repulsion, for instance, is more significant in toluene than in acetone. Oxygen fluorescence quenching is directly influenced by this effect and it can be witnessed in these two classes of molecules.

- Intersystem crossing (ISC)

Intersystem crossing represents the non-radiative transition between states of different spin multiplicity. The total energy is normally conserved which means that the molecule gains vibrational excitation after an  $S_1 \rightarrow T_1$  transition. ISC is permitted for  $S(n, \pi^*) \rightarrow T(\pi, \pi^*)$  and  $S(\pi, \pi^*) \rightarrow T(n, \pi^*)$  and forbidden for  $S(n, \pi^*) \rightarrow T(n, \pi^*)$  and  $S(\pi, \pi^*) \rightarrow T(\pi, \pi^*)$  transitions. The transition probabilities of forbidden transitions are not exactly zero

due to interaction of the electronic wave function with vibrations. However, they are notably reduced compared to allowed transitions.

For ketones and benzene derivatives such as toluene, ISC is symmetry-forbidden. Nevertheless, it is three and one orders of magnitude faster than the respective rates of spontaneous  $S_1 \rightarrow S_0$  emission. ISC can be significantly increased in the presence of molecular oxygen. This is discussed in the collisional quenching section below.

- Internal conversion (IC)

The non-radiative transition process between states of the same spin multiplicity is known as internal conversion. This process is symmetry-allowed. IC is considered to have a minor significance for typical species used as fluorescence tracers due to the large energy difference between  $S_0$  and  $S_1$ . This means that fluorescence is emitted from  $S_1$  state only. Note that the energy difference between the excited singlet states is small enough to enable fast  $S_2 \rightarrow S_1$  transitions.

- Vibrational relaxation (VR)

Vibrational relaxation takes place via collisions with bath-gas molecules. In the liquid phase, VR is very fast. In the gas phase, VR does not lead to full thermalization during the fluorescence lifetime thus rendering the signal pressure-dependent. Other processes such as ISC and spontaneous emission take place on the same timescale as VR.

## **Kinetics of photophysical processes**

### *Radiative and effective lifetimes*

The temporal variation of the number of excited molecules  $M^*$  can be described by a first-order differential equation (2-1) considering that fluorescence emission of a photon  $h\nu$  is the only pathway of relaxation of  $M^*$ .

$$-\frac{d}{dt}[M^*] = k_{fl}[M^*] \quad (2-1)$$

Using equation (2-1), the concentration of excited molecules  $[M^*]$  can be expressed in terms of the exponential decay of the rate of fluorescence process  $k_{fl}t$  and the initial concentration  $[M^*]_0$ .

$$[M^*] = [M^*]_0 e^{-k_{fl}t} \quad (2-2)$$

Within the radiative lifetime,  $\tau_{\text{rad}}$ , the number of the excited molecules decay to 1/e of the initial value.

$$\tau_{\text{rad}} = \frac{1}{k_{\text{fl}}} \quad (2-3)$$

When dealing with practical systems,  $[M^*]$  decreases more rapidly due to simultaneous occurrence of non-radiative processes ISC and IC. The decrease in  $[M^*]$  can be expressed in the following equation below:

$$\frac{d}{dt}[M^*] = -(k_{\text{fl}} + k_{\text{ISC}} + k_{\text{IC}})[M^*] \quad (2-4)$$

The total rate of depopulation of the excited state,  $k_{\text{tot}}$ , includes all individual depopulating processes  $i$ ,

$$k_{\text{tot}} = \sum k_i \quad (2-5)$$

leading to the experimentally accessible effective fluorescence lifetime:

$$\tau_{\text{eff}} = \frac{1}{k_{\text{tot}}} \quad (2-6)$$

### *Fluorescence quantum yield*

Due to non-radiative processes, not all excited molecules emit fluorescence. The fraction of excited molecules that actually emit fluorescence is called fluorescence quantum yield,  $\phi_{\text{fl}}$ , which would be unity in the absence of non-radiative relaxation. The fluorescence quantum yield as expressed in equation (2-7) is the ratio of the fluorescence rate,  $\tilde{k}_{\text{fl}}[M^*]$ , over the absorption rate  $\tilde{k}_{\text{abs}}[M^*][h\nu]$ , where  $[h\nu]$  is the photon density. A steady-state population of  $M^*$  can be established by using a nanosecond laser pulse duration.

$$\phi_{\text{fl}} = \frac{\tilde{k}_{\text{fl}}[M^*]}{\tilde{k}_{\text{abs}}[M^*][h\nu]} \quad (2-7)$$

The temporal variation of the excited state population (equation (2-8)) can thus be obtained by using the rate coefficient of non-radiative excited state depopulation  $\tilde{k}_{nr} = \tilde{k}_{tot} - \tilde{k}_{fl}$ .

$$\frac{d}{dt} [M^*] = \tilde{k}_{abs}[M^*][h\nu] - (\tilde{k}_{fl}[M^*] + \tilde{k}_{nr}[M^*]) \quad (2-8)$$

Note that the temporal variation can be used to determine  $[M^*]$ , which is difficult to obtain experimentally, as:

$$[M^*] = \frac{\tilde{k}_{abs}[M^*][h\nu]}{\tilde{k}_{fl} + \tilde{k}_{nr}} \quad (2-9)$$

The fluorescence quantum yield is thus interpreted as the ratio of the rate of coefficients of fluorescence and the total depopulation or the inverse ratio of the respective lifetimes:

$$\phi_{fl} = \frac{\tilde{k}_{fl}}{\tilde{k}_{abs}} = \frac{\tau_{eff}}{\tau_{rad}} \quad (2-10)$$

The radiative lifetime can be obtained by measuring the fluorescence quantum yield and the effective lifetime. Note that the rate coefficients are denoted by  $\tilde{k}$ . For spontaneous processes, the rate coefficients are converted to rates by multiplying with the concentration. In the following sections,  $[M^*]$  cancels in the equations for most processes. Therefore, all  $[M^*]$  were discarded and the tilde notation was eliminated. The tilde notation is only utilized again when collisional processes are considered for which the rate depends not only on  $[M^*]$  but also on the number density of the collider (cf. section 0).

The detected fluorescence signal intensity (i.e., absolute signal)  $S_{fl}$  is proportional to the number of fluorescence photons  $n_{fl}$ , which is the product of the absorbed photons, the fluorescence quantum yield  $\phi_{fl}$ , the efficiency of the detection system  $\eta$  and the observed solid angle  $\Omega/4\pi$ . The term  $E/h\nu$  is the photon flux in  $\text{cm}^{-2}$ .  $n_{fl}$  is the number density of the fluorescence tracer in the observed volume  $V$  that have the absorption cross-section  $\sigma_{abs}$  in  $\text{cm}^2$ .

$$S_{fl} = \left( \frac{E}{h\nu} \right) V n_{fl} \sigma_{abs} \phi_{fl} \eta \frac{\Omega}{4\pi} \quad (2-11)$$

## Collisional quenching

All the non-radiative processes that cause depopulation of the excited states that were presented so far were intra-molecular processes. A number of strong inter-molecular deactivating processes can take place depending on the properties of colliding molecules. In the sections below, the kinetics and mechanics of these processes will be addressed.

### *Stern-Volmer coefficient*

When collisional quenching takes place, an additional term is added to the denominator of equation (2-10) to account for its effect on fluorescence quantum yield. The probability of the fluorescence quenching is proportional to the collisional rate with the respective species times a species-specific quenching cross-section. This is expressed by the product of the number of density of the colliding species  $n_q$  and rate coefficient  $\tilde{k}_q$ . Therefore the fluorescence quantum yield becomes as follows:

$$\Phi_{fl} = \frac{k_{fl}}{k_{tot} + \tilde{k}_q n_q} = \frac{\tau_{eff}}{\tau_{rad}} \quad (2-12)$$

The tilde notation is applied in order to differentiate between the rates of energy transfer processes (e.g.,  $k_{tot}$ ) and the rate coefficients (e.g.,  $\tilde{k}_q$ ). The rate coefficient  $\tilde{k}_q$  becomes a rate after multiplying it by the respective number density of the quenching species  $n_q$ .

The variation of the signal intensity with respect to the concentration of the quenching molecules can be described as follows:

$$\frac{S_{fl}^0}{S_{fl}} = \frac{k_{fl}}{k_{tot}} \frac{k_{tot} + \tilde{k}_q n_q}{k_{fl}} = 1 + \frac{\tilde{k}_q}{k_{fl}} n_q \quad (2-13)$$

where  $S_{fl}^0$  is the fluorescence intensity in the absence of quenching. Measurements performed while varying the quencher concentrations under identical ambient conditions can be exploited to assess the ratio  $\tilde{k}_q/k_{tot}$ . This ratio is known as the Stern-Volmer coefficient  $k_{SV}$  which is an indicator of the importance of fluorescence quenching. The plot for graphical analysis of equation (2-14) is called the Stern-Volmer plot.

$$k_{SV} = \frac{\tilde{k}_q}{k_{tot}} = \tilde{k}_q \tau_{eff} \quad (2-14)$$

Assuming that quenching is due to short-range collisions, the quenching constant can be interpreted as a product of the collisional frequency  $Z_{\text{coll}}$  as derived from the kinetic gas theory and a probability  $\langle p \rangle$  of an effective collision.

$$\tilde{k}_q n_q = Z_{\text{coll}} \langle p \rangle \quad (2-15)$$

### *Electronic energy transfer*

Electronic energy transfer is the primary process that causes collisional quenching. The quenching molecule in its ground state  $Q$  is electronically excited during collision based on the following relation:



$M^*$  is referred to as the donor while  $Q$  is referred to as the acceptor. The electronic energy transfer is comprised of two fundamentally different processes which will be detailed in the section below.

- Fluorescence resonance energy transfer (FRET)

Förster was the first to describe the fluorescence energy process in [43]. FRET is led by distortions in the electronic structure of the donor and the acceptor due to dipole-dipole interactions. The dipole oscillation of  $M^*$  then induces an oscillation in  $Q$  without direct physical contact between the two. This interaction depends on the distance between the molecules where it permits energy transfer over a distance up to 10 nm. Within a given time interval  $dt$  the probability of energy transfer  $dP_n$  is,

$$dP_n = \tau_{\text{eff}}^{-1} \left( \frac{r_0}{r} \right)^6 dt \quad (2-17)$$

with  $\tau_{\text{eff}}$  being the fluorescence lifetime. The critical radius  $r_0$  determines the strength of the interaction which depends on the overlap between the emission spectrum of the donor and the absorption spectrum of the acceptor.

Note that electrons are not exchanged between the molecules. Hence, the spin selection rules must be satisfied. There are two possible processes that can occur and they are illustrated below.

- Short-range energy transfer

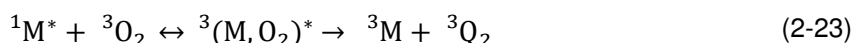
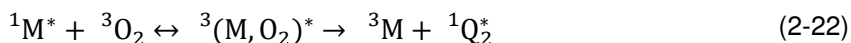


This mechanism was described by Dexter [44]. In this process electrons are exchanged between molecules, therefore direct contact resulting in spatial overlap between different molecular orbitals is a necessity. The maximum distance is of the order of 0.5–1 nm. The spectral overlap of the two molecules has an impact on the probability of this process. Here, selection rules do not apply. For this process, two reactions (c.f., (2-20) and (2-21)) are allowed to occur.



- Fluorescence quenching by molecular oxygen

The ground state of molecular oxygen is a triplet state rendering fluorescence quenching of organic molecules very effective because the transition into triplet states is facilitated. The energy transfer reactions can be therefore written as [45]:



The colliding molecules form a short lived electronically excited transition state (exciplex). This results in coupling between different spin multiplicity states which in turn enables the otherwise spin-forbidden intersystem crossing. When ionization increases, the quenching rate  $\tilde{k}_q$  is decreased indicating that at least partial charge occurs in the transition state [46]. This only takes place if the energy difference between M's singlet and triplet state is larger than the energy required for excitation of O<sub>2</sub> into its singlet state.

In conclusion, aromatic molecules are highly quenched by O<sub>2</sub> while small aliphatic ketones are only slightly influenced by O<sub>2</sub> [47]. The mechanism of oxygen quenching is described in [48].

### Sensitized fluorescence

When the absorption and emission spectra overlap, energy transfer during collisions (or at small distances even without collisions) between organic molecules can take place. This property has been exploited for mixing studies where two flows were seeded with two different tracers known as donor and acceptor. The donor is excited at a certain wavelength and then transmits its excitation to the acceptor in the region where the two flows convene. The acceptor thus emits fluorescence that can be utilized as an indicator for the mixing process. This technique was used by Yip et al. [49] to visualize gas-phase fluid mixing with acetone as donor and biacetyl as acceptor.

Caution is required when ketones and aromatic tracers are used in combination because of efficient energy transfer between these two tracer classes. Krämer et al. [14] used a mixture of 3-pentanone and toluene to investigate the spatial distribution of fuel components with different volatilities of a multi-component fuel. 3-Pentanone was found to quench the fluorescence of toluene with an efficiency equivalent to that of O<sub>2</sub>. Consequently, the electronic energy transfers from collisions with toluene led to the increase of 3-pentanone fluorescence.

### **2.3 Scientific question and measurement strategy in this work**

In modern internal combustion (IC) engines, evaporation and mixing effects of multi-component fuels are highly relevant. Direct injection enhances effects of preferential evaporation of compounds with different volatility that potentially cause mixture inhomogeneity, wall wetting and delayed evaporation, oil dilution, pool fires, etc. Fuels that contain biomass-derived components with unconventional evaporation properties further enhance preferential evaporation. Consequently, it is of great interest to develop measurement techniques that can assess the effects of preferential evaporation on the resulting fuel/air mixture, in particular for validation of simulations and optimization of injection strategies. Laser-induced fluorescence (LIF) imaging is an appropriate technique in this context that is frequently used to observe mixture formation in non-fluorescing base fuels with well-characterized fluorescence tracers [6].

To quantitatively measure the relative variation of concentrations of fuel components of multi-component fuels with combined tracers, three challenges must be addressed: (1) Tracers must be selected that well match the evaporation properties of the fuel components of interest. (2) The spectral characteristics of the respective tracers must be known for the relevant range of temperature, pressure, and mixture composition. Specifically, the LIF emission of the selected tracers must be in separate spectral regions to allow for

simultaneous measurements with minimum cross-talk and the tracers should have negligible photophysical interaction to allow for a straight-forward interpretation of signal intensities. (3) A measurement strategy capable of quantifying the effects of preferential evaporation with minimal measurement uncertainties in complex engine environments must be determined.

Most of the techniques reported in the literature fail to satisfy these combined requirements. Fuel distribution measurements usually address single-component fuels doped with either a ketone or an aromatic tracer [13, 50, 51] and tracers are often chosen to provide maximum signal. Single-component surrogate fuels, however, do not well represent the evaporation of commercial fuels that contain a variety of components with different volatilities that impact spray penetration and vaporization [52, 53].

The three scientific challenges identified in the previous section are still being addressed within a systematic sequence of collaborative projects. The first project, known as BIOPTIC I, between IFPE and ONERA was carried out between 2008 and 2010 to address these issues. Within this work, measurement methodologies capable of providing quantitative information on the effect of biomass derived fuel components on fuel/air-mixture distribution in simplified configurations (low ambient pressure, adiabatic conditions, and homogeneous ambient composition) were developed. This methodology required thermodynamic approaches that can appropriately predict multi-component fuel and tracer evaporation properties. For this purpose, a thermodynamic model that fulfills these requirements was established. Several fluorescence tracers with a wide variety of evaporation properties were identified and then characterized. Lastly, measurement strategies were developed to test the functionality and credibility of results obtained by the thermodynamic model. The results showed that the scientific challenges related to multi-component fuel effects are within a reasonable reach. However, more work was still necessary to develop a reliable measurement technique capable of characterizing preferential evaporation effects of multi-component fuels in engine-relevant conditions (i.e., high pressure high pressure environment). To respond to those demands, a second collaborative project, BIOPTIC II, between IFPE, CORIA, and IVG was carried out between 2012 and 2015. The methodology that was initially developed for jet- and Diesel-fuel in BIOPTIC I was extended to gasoline fuels in BIOPTIC II. A new multi-component surrogate fuel representative of gasoline was designed by the department of applied thermodynamics and molecular modeling at IFPE. Therefore, new corresponding tracers were selected and characterized. A number of tracers were investigated for relevant-engine conditions. Only two tracers, *p*-difluorobenzene and 1-methylnaphthalene were

characterized within this PhD thesis. The spectroscopic characterization is particularly robust because CORIA and IVG use complementary methods for photophysical characterization of tracers. Regardless of the differences between the experimental setups and methods applied, experimental findings from both institutes can be compared. Lastly, an application of the methodology to typical injection conditions was carried out which is the core of this PhD thesis. The LIF imaging technique developed here aims at localizing effects of preferential evaporation and at qualitatively determining the deviation from the case of equal distribution of the fuel components for gasoline-type fuels. A two-tracer strategy was applied to study the mixture formation for two injectors (ECN Spray G injector and a piezo-electric outward-opening injector) under conditions representative for realistic engines, yet in an  $O_2$ -free environment. Two-color 1-methylnaphthalene LIF thermometry measurements were performed simultaneously to investigate the homogeneity of the temperature field across the vaporized spray. The fuel mass concentration fields were also derived from jet images using the normalization method illustrated in [54].

### **3 Photophysical measurements of *p*-difluorobenzene and 1-methylnaphthalene**

The ideal tracer mixture to detect effects of preferential evaporation should be composed of a low- and a high-volatility tracer. Each tracer will then ideally co-evaporate with its corresponding fuel component. Thermodynamic equilibrium calculations carried out within the Bioptic II framework showed that a mixture of *p*-difluorobenzene (*p*-DFB) and 1-methylnaphthalene (1-MN) is adequate for identifying preferential evaporation since the former evaporates with the high-to-medium volatility component (i.e., *n*-pentane and *iso*-octane) and the latter with the low-volatility component (i.e., *n*-undecane). This tracer mixture also enables LIF thermometry due to the red-shift of 1-MN spectrum with temperature increase.

This chapter illustrates photophysical measurements performed on *p*-DFB and 1-MN. The spectral and temporal fluorescence properties of both tracers were investigated for laser excitation at 266 nm to obtain experimental data of fluorescence spectra and lifetimes over a wide temperature and pressure range representative of IC-engine conditions. Fluorescence lifetime measurements were performed at the Institute of Gas and Thermodynamics (IVG) at University of Duisburg-Essen using a high-pressure high-temperature flow vessel. These experiments were conducted together with Thorsten Benzler who is a PhD candidate at the University of Duisburg-Essen. The fluorescence spectra analysis was performed at CORIA laboratories by Björn Rossow who is a post-doctoral researcher at CORIA. Fluorescence spectra could have been derived from experiments performed at IVG, however, the CORIA results showed a higher spectral resolution and therefore were selected for spectral analysis. Fluorescence spectra and lifetimes of *p*-DFB and 1-MN were acquired in a temperature of 296–980 K and 325–925 K respectively, in a pressure range of 1–10 bar in N<sub>2</sub>.

#### **3.1 Investigation of tracer fluorescence**

##### **3.1.1 Fluorescence lifetime measurements of *p*-DFB and 1-MN**

There are different kinds of experimental apparatus that serve as tools for studying the photophysical properties of tracers under well-defined temperature, pressure, and bath-gas conditions. Static vessels with optical access are adequate for photophysical studies up to moderately high temperature [55]. The downside of these vessels is the long residence times which can lead to degradation of species due to pyrolysis or photolysis. This can be avoided by continuously flowing a gas mixture through the vessel. Most of the

flow vessels are made out of stainless-steel and are externally heated. Materials stability and the complexity of sealing windows under these conditions restricts measurements to maximum temperatures to below 900 K at high pressures [36, 56]. On the other hand, ceramic flow cells are corrosion resistant and capable of withstanding much higher temperatures, however, due to their fragility and the high possibility of chemical decomposition, measurements are often limited to atmospheric pressure. A cell developed by Trost et al. [27] was designed to provide rapid mixing thus avoiding chemical decomposition, however, the concern here is mixture homogeneity. To overcome these limitations, shock tubes are suitable for experiments that target high temperature and pressure as operating conditions simultaneously. The short exposure time to the desired temperature and pressure conditions limits the measurement time and thus prevents problems with decomposition at temperatures up to  $\sim 1775$  K [57]. One of the downsides of this approach is the low duty cycle of the experiments providing only a limited amount of measurements per day.

The flow vessel used in this work for LIF lifetime measurements is based on gases flowing through an alumina ceramic tube which can reach temperatures up to 1400 K. The alumina ceramics vessel is installed inside a thermally insulated stainless-steel cylinder allowing high-pressure measurements up to 10 bar.

### **High-temperature high-pressure flow vessel design**

The flow vessel shown in Figure 3-1 was used in this work to measure fluorescence spectra and lifetimes of vaporized tracers under a wide range of temperature, pressure, and bath-gas composition. The flow cell consists of two concentric ceramic tubes with four circular openings at  $90^\circ$  for optical access to the probe volume in the center of the inner tube. The inner and the outer flow chamber with a diameter of 55 and 89 mm respectively, are placed inside a stainless-steel vessel of 400 mm diameter. Electric heaters are positioned around the outer flow chamber and are thermally insulated against the vessel walls. The gas mixture enters the stainless-steel vessel from its bottom by a concentric tube-in-tube feed through.

The path of the gas flow is shown in Figure 3-1. The gas mixture reaches the lower chamber and is preheated before it flows upwards through the outer flow chamber consisting of eight ceramic tubes. As the heated gas flow reaches the upper chamber, the flow direction is reversed downwards into the inner chamber via seven holes. The stainless-steel vessel is equipped with four quartz windows of 30 mm clear aperture. These windows are aligned with the opening of the outer and the inner chamber. The windows

are equipped with purge flows to avoid having an absorbing species getting trapped in the volume between the windows and the outer chamber.

The temperature of the outer flow chamber is controlled via an R-type thermocouple. The gas inside the inner chamber is measured with another R-type thermocouple located shortly above the probe region. The flow cell is designed to operate at a maximum temperature of 1400 K. Elevated pressures are obtained with two back-pressure regulators (Hoke, 1–6 bar, and 2–10 bar, respectively) located between the exit of the cell and the exhaust line. The needle valve position of the back-pressure regulator is controlled manually.

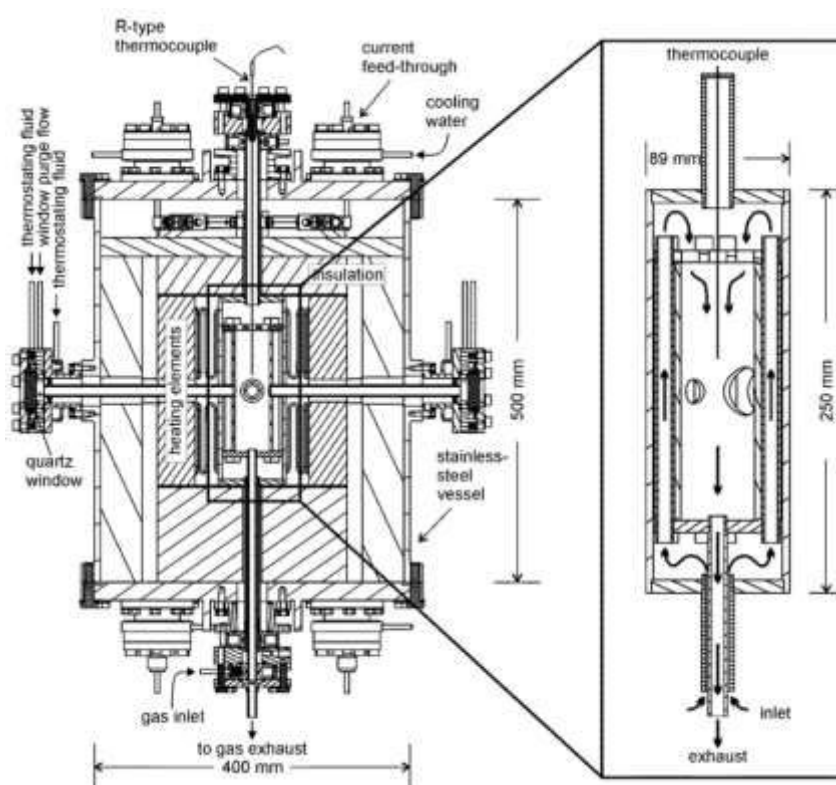


Figure 3-1: Schematic of the high-pressure high-temperature flow vessel (left) at the University of Duisburg-Essen and its alumina ceramic flow tube (right) where the inner gas flow is located [41]. The interrogation region is in the center of the ceramic tube.

### Tracer/gas supply and control system

Figure 3-2 depicts the gas supply for the high-pressure high-temperature vessel. The tracers that are in the liquid state at ambient conditions, are stored in a glass canister. The canister is sealed by a stainless-steel cap and connected to a HPLC pump (high-pressure liquid chromatography pump 2250, Bischoff-Chrom) which meters the tracer liquid flow at a maximum pressure of 25 bar. The liquid tracer then enters an electrically-

heated evaporation and mixing chamber (CEM: controlled evaporator mixer, Bronkhorst) where it completely evaporates and mixes with the carrier gas. The carrier gas is controlled by a mass-flow controller (Bronkhorst) with the range of 1–4 slm (standard liter per minute). The mixture is then directed towards a gas mixing chamber where it is mixed with a second gas flow with 2–20 slm controlled by mass flow controllers. After the gas-mixing chamber, the gaseous mixture enters the cell. The bath-gas composition is controlled by the carrier gas flow set in the CEM and the gas flow fed into the gas-mixing chamber which allows a study of the tracer in a bath gas of N<sub>2</sub>, air, and a mixture of N<sub>2</sub>/air with various O<sub>2</sub> partial pressures in the range of 0–0.21 bar.

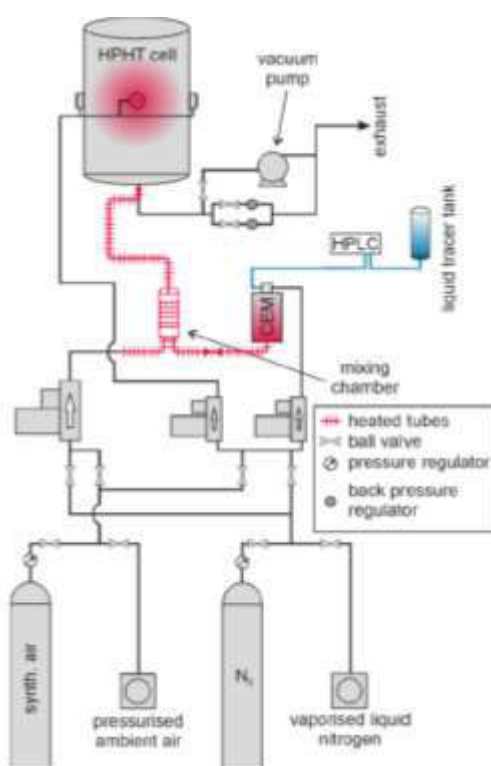


Figure 3-2: Schematics of the tracer-gas supply and control system [41].

### Optical arrangement

For the measurements of effective fluorescence lifetimes the fourth harmonic (266 nm) of a picosecond Nd:YAG laser (PL2143B, Ekspla) was used. The laser is capable of delivering 7 mJ at 266 nm with a pulse length of 26 ps at a repetition rate of 10 Hz. The laser beam is reduced to 3 mm before entering the vessel by a convex-concave ( $f = 100$  mm and  $f = -40$  mm) lens arrangement. The fluorescence signal is then collected perpendicularly to the laser beam via two consecutive convex-quartz lenses ( $f = 375$  mm and  $f = 300$  mm) and thus focused on the entrance slit of the spectrograph ( $f = 300$  mm,

Acton SP2300, Princeton Instruments with a 150 grooves/mm grating) by a UV-enhanced aluminum mirror. The spectrally-resolved fluorescence signal is projected onto a streak camera which is equipped with a streak module (C5680-24C, Hamamatsu) and a CCD camera (Orca R2, 640×512 pixel). Camera and laser were synchronized with a trigger pulse generator (DG645, Stanford Research Systems). The system produces 2D images with temporal and spectral (plotted on the x- and y-axis respectively) intensity information.

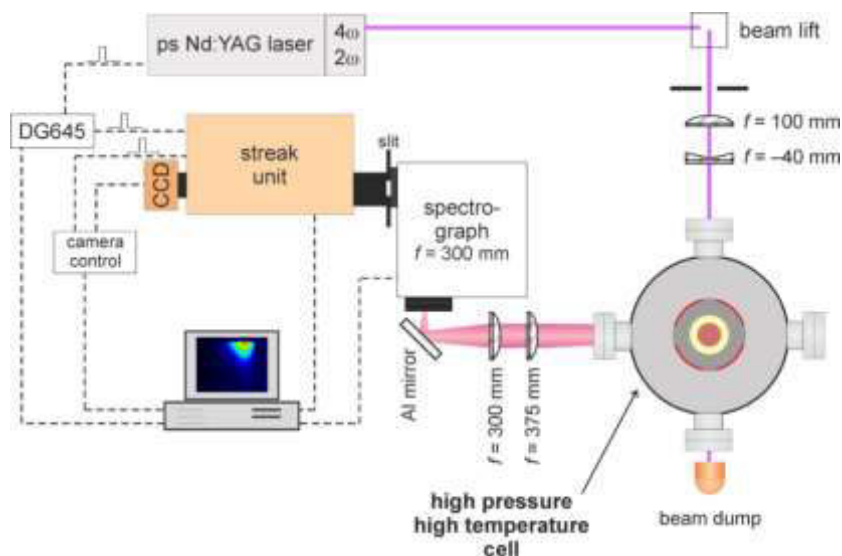


Figure 3-3: Optical arrangement for measuring spectrally- and temporally-resolved tracer fluorescence. M1: aluminum mirror, L1-L4: quartz lenses, CCD: CCD: camera, DG465: pulse delay generator [58].

### 3.1.2 Evaluation of effective fluorescence lifetime of tracers

Temporal and spectral information can be derived from the 2D images obtained by the streak-camera system. However, this section will be solely dedicated to the evaluation of effective fluorescence lifetime of *p*-DFB and 1-MN. The evaluation of the spectra will be discussed in section 3.1.4.

For each condition, 1000 instantaneous images were recorded and averaged to enhance the single-to-noise ratio. Prior to averaging, each instantaneous image was corrected for laser jitter by a built-in jitter correction function provided by the streak camera software. Afterwards, a background image was subtracted from each instantaneous image. The background image was acquired by averaging 1000 instantaneous images obtained while the laser is running and with only N<sub>2</sub> flowing in the cell.

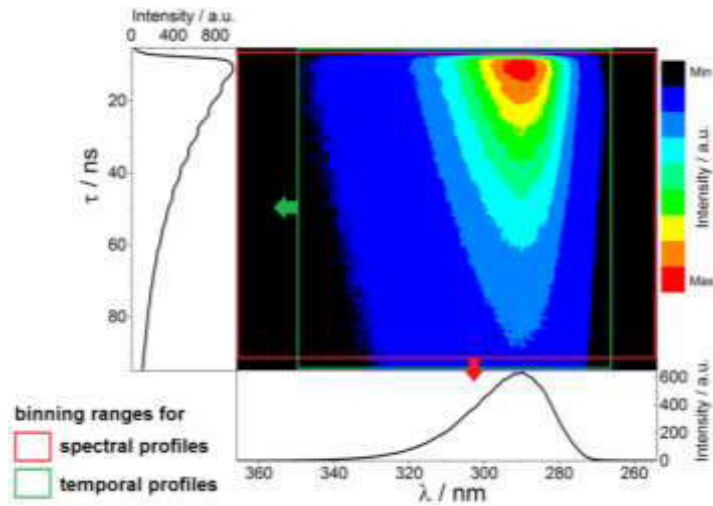


Figure 3-4: Sample image (averaged over 1000 instantaneous images) of temporally- and spectrally-resolved fluorescence for 1.5 mbar *p*-DFB after excitation at 266 nm at 700K in N<sub>2</sub> at a total pressure of 1 bar. The signal integration ranges along the time axis for the evaluated spectral profiles are marked as red, and along the spectral axis for the decay profiles as green rectangles, respectively.

Vertical binning of rows results in fluorescence spectra for specific time intervals, while horizontal binning of columns results in effective fluorescence lifetimes curves. In this section, the focus will be on the evaluation method performed to determine the effective fluorescence lifetime.

Signal decay times,  $\tau$ , were calculated by a simplified version of the convolve-and-compare technique introduced by Settersten et al. [59] and depicted below:

$$I(t) = I_f(i_o, \tau_o, t_o, t) f(t) + y_o \quad (3-1)$$

The LIF-signal  $I(t)$  is the result of temporally convoluting the single-exponential decay function  $I_f$  with an amplitude  $i_o$ , a decay time  $\tau_o$ , and a time offset  $t_o$  with the temporal instrument response function  $f(t)$  and by considering the baseline offset  $y_o$ . All adjustable parameters are indexed by “o”. Therefore when employing a double-exponential function  $I_f$ , two amplitudes ( $i_{1,o}, i_{2,o}$ ) in addition to two decay times ( $\tau_{1,o}, \tau_{2,o}$ ) were considered. The modeled decay is then fitted to the experimental decay by minimizing the sum of the squares of the residual differences between the two. The parameter  $t_o$  was determined from the maximum of the decay curve.

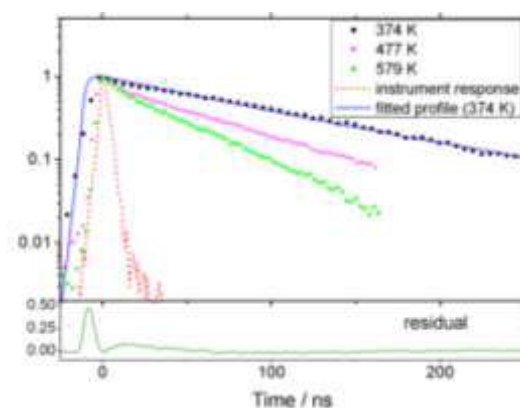


Figure 3-5: Time-resolved LIF intensity for 1-MN in 1 bar N<sub>2</sub> with excitation at 266 nm at various temperatures. For 374 K, the fitted function and the residuals are shown as blue and green curve, respectively. The instrument response curves (red dashed lines) were recorded without tracer for the streak speeds appropriate for the 374 K measurements.

Figure 3-5 shows 1-MN LIF decay profiles for three gas temperatures. Decay times vary significantly with changing ambient conditions. Therefore, for each temperature the time-span setting of the streak camera was adjusted in order to optimize the temporal resolution of the detection system. For the present hardware settings, the minimum temporal resolution of the detection system was 50 ps.

### 3.1.3 Fluorescence spectra measurements of *p*-DFB and 1-MN

Fluorescence spectra of *p*-DFB and 1-MN were derived from experiments performed by Björn Rossow, a post-doctoral researcher at CORIA laboratories. These experiments were performed within the BIOPTIC II framework and therefore in the following section the flow cell and the data evaluation procedure will be addressed.

#### Flow cell

The cell used for fluorescence spectral measurements at CORIA laboratories allows the observation of tracer vapor fluorescence for temperatures and pressures in the 300–900 K and 1–30 bar range after laser excitation in the UV. Figure 3-6 shows the cell which has outer dimensions of 190×145×120 mm<sup>3</sup> with 15 mm overall minimal wall thickness. The inner volume is ~230 cm<sup>3</sup>. Optical access is provided by three UV-transparent silica windows. Two windows are mounted opposite to each other allowing the laser to pass through the probe volume while the fluorescence gets registered by a spectrograph mounted perpendicular to the laser path.

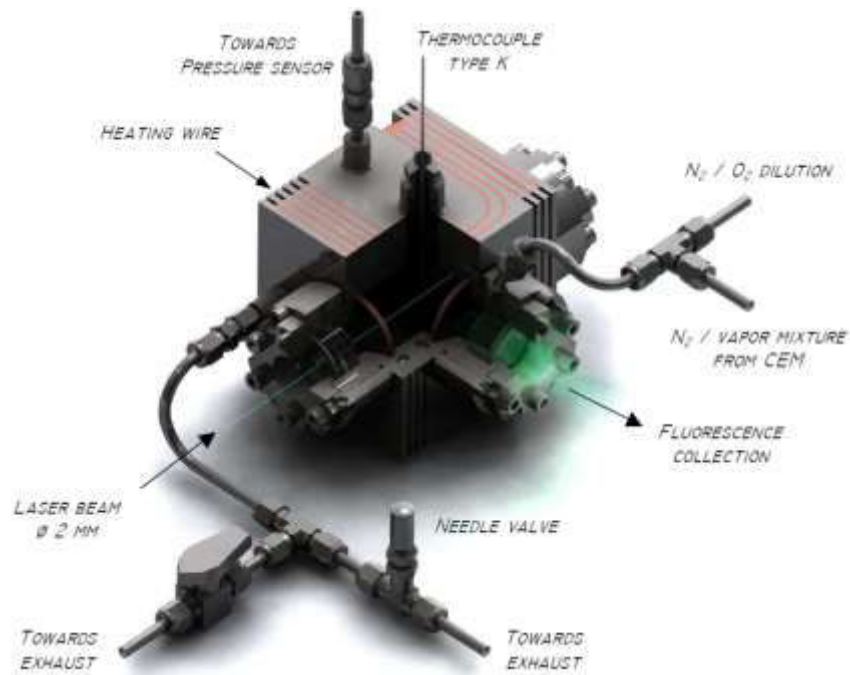


Figure 3-6: Flow cell for high-temperature high-pressure fluorescence spectra measurements [39]. The tracer is evaporated in  $N_2$  gas by the CEM system. Oxygen can be added to the tracer/ $N_2$  mixture before it enters into the cell [39].

### Tracer/gas supply and control system

Tracer vapor concentration entering the cell is controlled by a controlled evaporator mixer (CEM, Bronkhorst). Continuous and constant evaporation of the liquid tracer to the buffer gas is accomplished in a steadily heated capillary of 473 K. The quantity of liquid tracer introduced into the CEM is controlled by a liquid flow meter (LFM) and the intake needle valve of the CEM while the gas flows are controlled by mass flow controllers (MFC, Bronkhorst). The flow system is controlled externally by a LabView routine with the help of a data acquisition board (National Instruments). Oxygen concentration in the test cell (ranging between 0–16.7%) is controlled by dilution with a  $N_2/O_2$  gas mixture (industrial air) at the exit of the CEM. Dilution is done as short as possible before the inlet of test cell in order to minimize the length of flow contact between tracer and oxygen and to limit effects of tracer oxidation knowing that the tracer concentrations used for these experiments are <0.15 vol%.

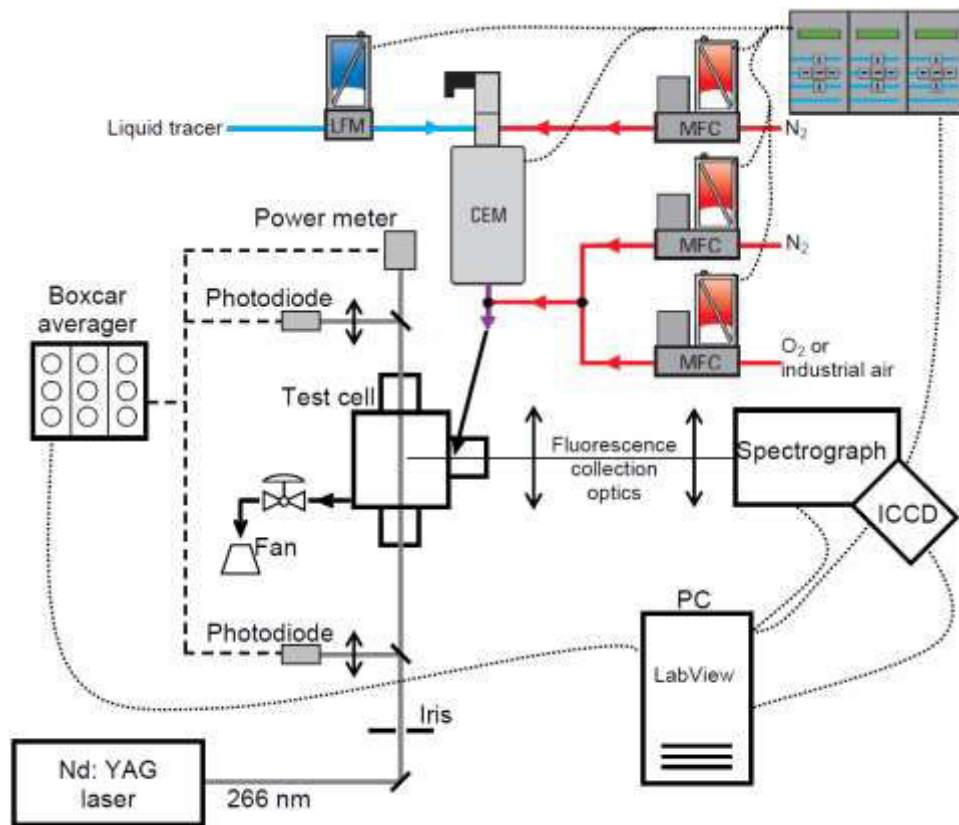


Figure 3-7: Experimental set-up for fluorescence spectra measurements at CORIA. Photodiodes are used to measure the laser beam intensity prior to and after the cell passage to correct for effects of laser attenuation [39].

### Temperature and pressure control

The test cell is heated with a heating wire (2 m long, 2 kW Thermocoax SEI type with Inconel alloy sheath) embedded into grooves in the cell body. The temperature of the gas inside the cell is controlled by a K-type thermocouple placed few millimeters above the laser probe volume. Pressures between 1–30 bar can be attained inside the cell and measured with a pressure transducer (Tb244, JPB). Read-out values of both pressure and temperature are used in a LabView routine to control the intake flow. Pressure ranges can be chosen by manually adjusting the needle valve at the test cell exhaust.

### Optical arrangement

Figure 3-8 depicts the optical arrangement used for fluorescence signal collection. Fluorescence light emission resulting from tracer excitation with an Nd:YAG laser tuned at 266 nm with a laser fluence of  $\sim 0.15 \text{ mJ/cm}^2$  is collected at a right angle to the laser beam by using a two UV achromatic doublets ( $f_1 = 160 \text{ mm}$  and  $f_2 = 100 \text{ mm}$ ). The light

is then collected by a spectrograph (Jobin Yvon, SPEX 270M) coupled with a CCD camera (Princeton Instruments, HSICCD-576G/BT, 576×384 pixels). Note that the framing rate of the system was fixed to 10 Hz thus matching the repetition rate of the laser. The spectrograph and the camera are controlled by a computer. Fluorescence spectra are measured for wavelengths ranging between 240–540 nm. The slit width was fixed to 1000  $\mu\text{m}$  providing a good signal-to-noise ratio and an adequate spectral resolution to detect the presence of fine spectral structure.

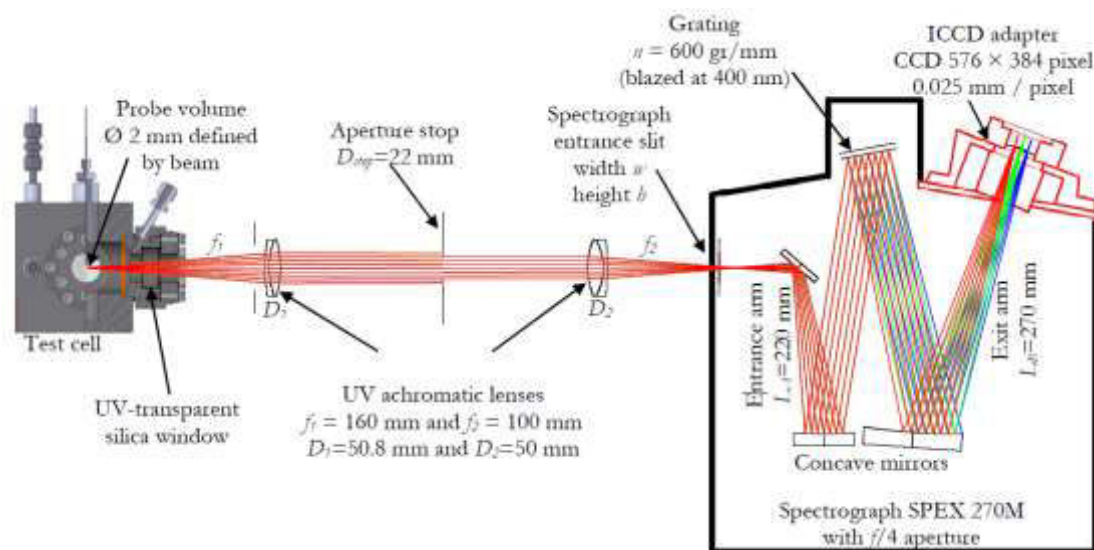


Figure 3-8: Optical arrangement for fluorescence detection. Fluorescence emitted by the excited molecules is collected by two achromatic lenses. The slit entrance of the spectrograph is parallel to the laser beam. The spectrograph has an aperture of  $f/4$  [39].

### 3.1.4 Evaluation of tracer fluorescence spectra

Prior to data evaluation, the spectral response of the entire optical set-up (i.e., the apparatus function) was determined by using a deuterium and a tungsten lamp. The deuterium lamp covers the UV spectral region ranging between 220–400 nm while the tungsten lamp covers the visible region ranging between 400–540 nm.

Based on the fluorescence signal intensity, spectra are accumulated for 100 to 400 laser shots. The resulting individual image recorded on the ICCD detector covers a spectral range of 80 nm. The spectrally-resolved fluorescence emission is then extracted from these images. The resulting spectral profiles were then corrected for the spectral response of the instrument.

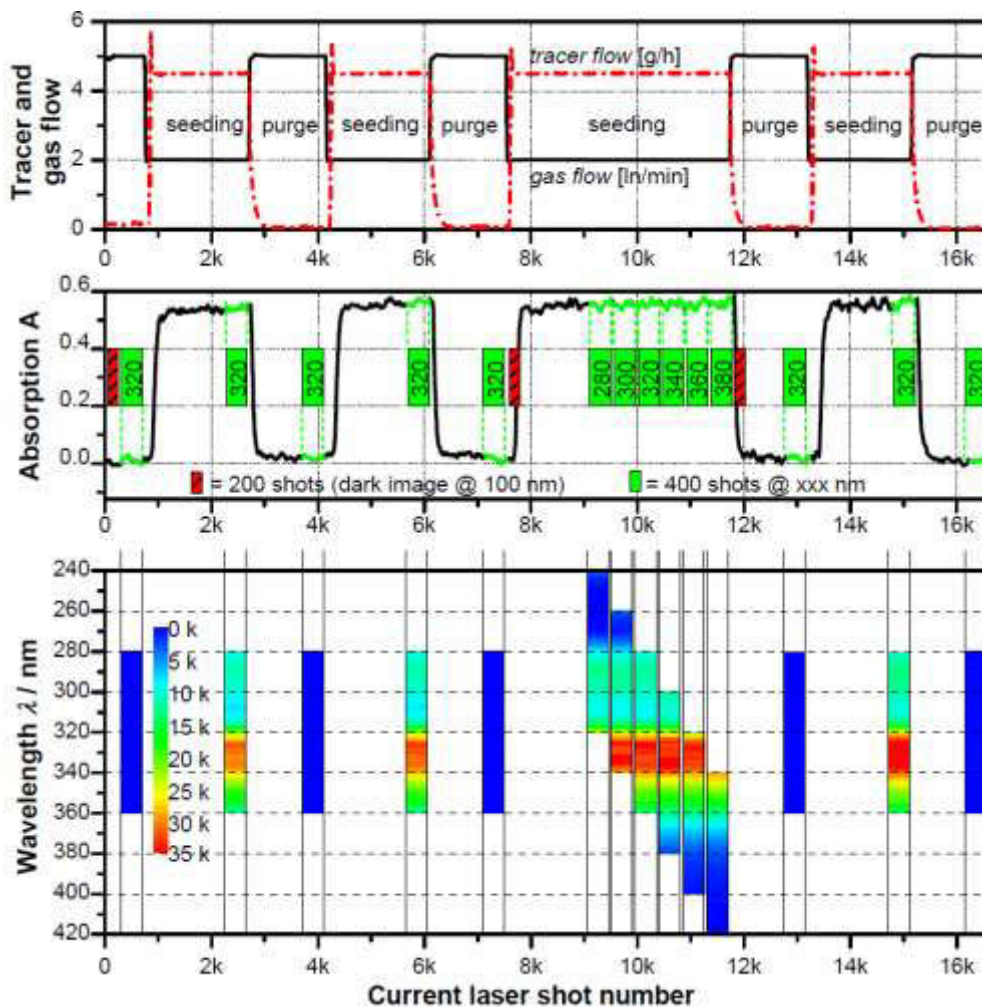


Figure 3-9: Example of a measurement cycle for the study of LIF spectra at a given condition which is kept constant throughout the cycle [39].

To guarantee a reproducible test cycle the measurement procedure is controlled via Lab-View. Figure 3-9 presents a typical measurement cycle. The probe volume in the test cell is alternately filled with the tracer gas mixture and purged with  $N_2$  to measure absorption and to check for the removal of tracers during purging. The detection system covers a spectral range of 80 nm which is insufficient for investigating the emission spectra for most tracer species especially when tracer pyrolysis takes place and therefore the fluorescence emission becomes spread over a wider spectral range than what is covered by one camera image. For this reason, fluorescence measurements each covering a spectral range of 80 nm were carried out with a 60 nm overlap to obtain sufficient information for combining the spectra covering a larger wavelength range [39]. In this combining algorithm, the overlapping spectral region of two spectra is filled with a weighted average of both spectra meaning that pixels closer to the CCD center receive heavier

weight factors. This algorithm allows the combination of multiple spectra and yields a continuous line without abrupt changes in intensity. Repeated dark image correction is realized by changing the spectrograph grating tilt to the 100 nm position. This grating position reproduces nearly the “closed camera” condition mainly due to the CCD entrance window not capturing light in the far UV. Comparison to a “real dark image” with closed camera revealed similar results and it was assured, that stray light is insignificant when taking dark images at 100 nm tilt angle.

## 3.2 Spectroscopic characterization of tracers

### 3.2.1 *p*-Difluorobenzene

*p*-DFB fluorescence lifetimes were investigated as a function of laser fluence to determine the limits of the linear regime which was found to be  $\sim 0.2$  mJ/cm<sup>2</sup> at 296 K and 1 bar. This fluence was used for all experiments performed with *p*-DFB. The *p*-DFB partial pressure was 1.2 mbar at 296 K which corresponds to a number density of  $2.93 \times 10^{19}$  m<sup>-3</sup>. At higher temperatures the partial pressure was increased providing a constant number density of *p*-DFB molecules in the probe volume.

#### Temperature and pressure dependence in N<sub>2</sub>

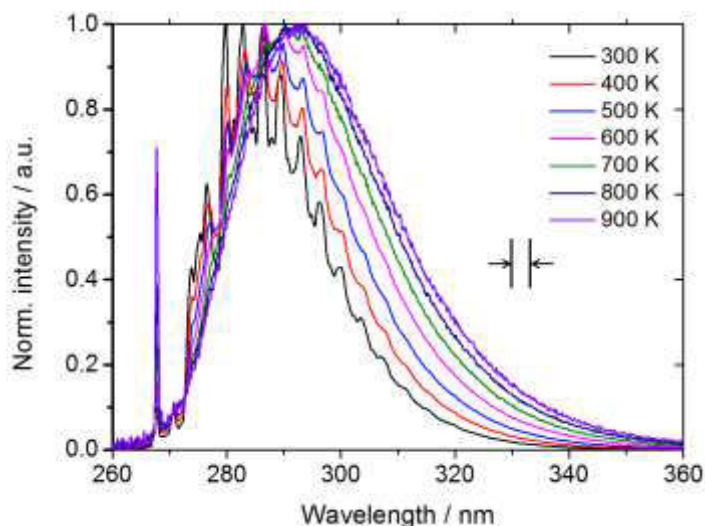


Figure 3-10: Peak-normalized *p*-DFB fluorescence spectra at various temperatures in 1 bar N<sub>2</sub> at a *p*-DFB number density of  $2.93 \times 10^{19}$  m<sup>-3</sup>. The arrows indicate the spectral resolution of the detection system by FWHM of a recorded mercury line at 254 nm.

Figure 3-10 displays the spectrum of *p*-DFB at 1 bar N<sub>2</sub> for temperatures between 300 and 900 K. Each spectrum was normalized to its respective peak intensity. An adjacent average 3 nm window size filter was applied for smoothing the spectra. At 300 K, the

emission ranges between 270 and 360 nm with the peak centered at around 280 nm. As temperature increases, the peak red-shifts by  $\sim 2$  nm per 100 K. The long wavelength tail of the spectra thus becomes stronger in comparison to the peak.

Figure 3-11 shows fluorescence lifetimes measured in  $N_2$  between 1–10 bar for 298–1025 K. For all the investigated pressure conditions, the fluorescence lifetime decreases with increasing temperature. For 1 bar, the fluorescence lifetime decreases from  $6.58 \pm 0.32$  ns at 298 K to  $0.74 \pm 0.05$  ns at 1025 K. The decrease in fluorescence lifetime is even more pronounced for 8 bar as it decreases from  $6.57 \pm 0.33$  ns at 296 K to  $0.39 \pm 0.04$  ns at 1025 K. This means that the total pressure has an influence on the fluorescence lifetime and thus on the fluorescence quantum yield.

To closely examine the impact of pressure on the fluorescence lifetime, measurements were performed at constant temperatures while changing the pressure between 1 and 10 bar. For 298 and 475 K, the effective fluorescence lifetime is almost constant. With increasing temperature (675–1025 K), the effective fluorescence quantum yield strongly decreases between 1–4 bar then they appear to level off for pressures above 4 bar.

At pressures higher than 8 bar, the lifetimes showed a constant behavior due to the limited temporal resolution (i.e., 50 ps) of the detection system and the convolute-and-compare algorithm. Therefore, measurements at pressures  $>8$  bar were not plotted since they are lower than the temporal resolution of the system.

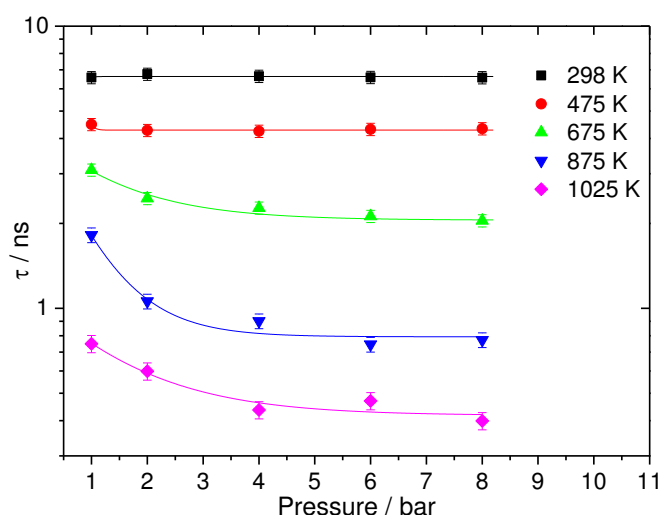


Figure 3-11: Effective fluorescence lifetime of *p*-DFB in  $N_2$  as a function of total pressure at various temperatures. The lines are fitted to show the trends.

## Influence of molecular oxygen

Molecular oxygen is generally a strong quencher of the  $S_1$  state of aromatic molecules [60] and hence also for  $p$ -DFB. Figure 3-12 shows the significant influence of  $O_2$  on the effective fluorescence lifetime. At room temperature the fluorescence lifetime reduces with increasing  $O_2$  partial pressure, with this trend decreasing at higher temperatures. The measurements cover a temperature range between 296 and 970 K and  $O_2$  partial pressures between pure  $N_2$  and air at 1 bar total pressure. The fluorescence lifetime in air at room temperature is 0.79 ns and decreases to 0.64 ns at 970 K. The decreasing quenching efficiency of  $O_2$  with increasing temperature has been observed for other aromatic tracers, like toluene [39, 60] and naphthalene [41] after excitation at 266 nm when determining relative fluorescence quantum yields from time- and wavelength-integrated tracer fluorescence spectra.

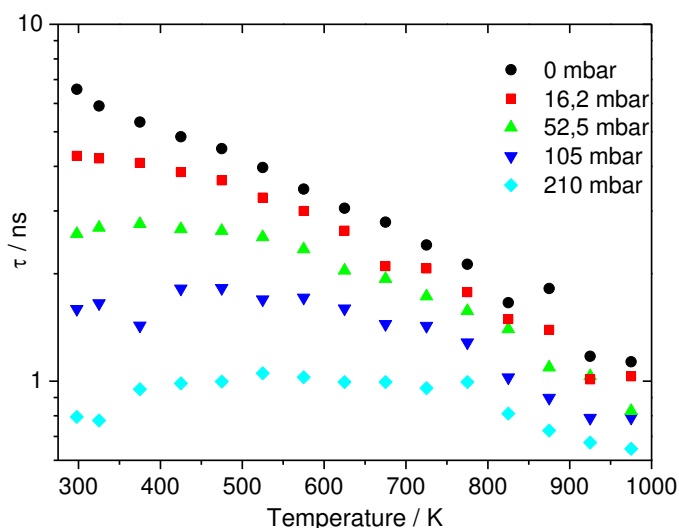


Figure 3-12: Effective fluorescence lifetime of  $p$ -DFB as a function of temperature for several  $O_2$  partial pressures in  $N_2$  at 1 bar total pressure.

The temporally-integrated fluorescence intensities of  $p$ -DFB show Stern-Volmer behavior, according to Eq.(2-12), which describes the signal variation as a function of quencher concentration. This should also apply to the measured effective fluorescence lifetimes. To validate this, Stern-Volmer coefficients were determined from data taken at atmospheric pressure for varying  $O_2$  partial pressures and several temperatures (cf., Figure 3-12). The temperature-dependent Stern-Volmer coefficients for quenching of  $p$ -DFB by  $O_2$  are depicted in the right panel of Figure 3-13.

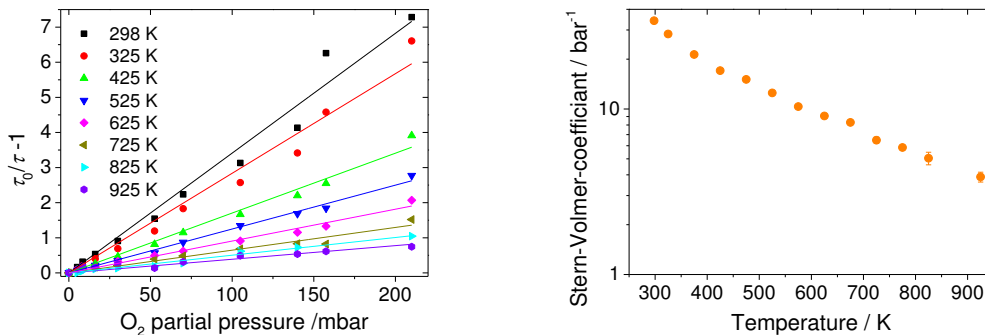


Figure 3-13: Stern-Volmer plots of *p*-DFB fluorescence quenched by  $O_2$  for selected temperatures (left). Stern-Volmer coefficients (right) for *p*-DFB at various temperatures for 1 bar total pressure.

### 3.2.2 1-Methylnaphthalene

The 1-methylnaphthalene (1-MN) fluorescence intensity was investigated as a function of laser fluence to determine the limits of the linear regime, which was found to be  $0.15 \text{ mJ/cm}^2$  at 373 K. At 373 K the naphthalene partial pressure was fixed at 0.9 mbar which corresponds to a number density of  $2.16 \times 10^{19} \text{ m}^{-3}$ . At higher temperatures the partial pressure was increased to maintain a nearly constant tracer number density in the probe volume. In additional measurements it was tested that at this number density self-quenching can be neglected.

#### Temperature and pressure dependence in $N_2$

Figure 3-14 shows peak-normalized fluorescence spectra of 1-MN diluted in  $N_2$  at a total pressure of 1 bar for 300–750 K. At 300 K, the fluorescence emission extends from roughly 300 to 400 nm with a maximum at around 325 nm. In comparison to *p*-DFB, 1-MN fluorescence shows a stronger red-shift with increasing temperature ( $\sim 5 \text{ nm per } 100 \text{ K}$ ). The long-wavelength tail of the spectra becomes stronger relative to the peak emission. The emission structure and the behavior of the 1-MN is very similar to naphthalene [39].

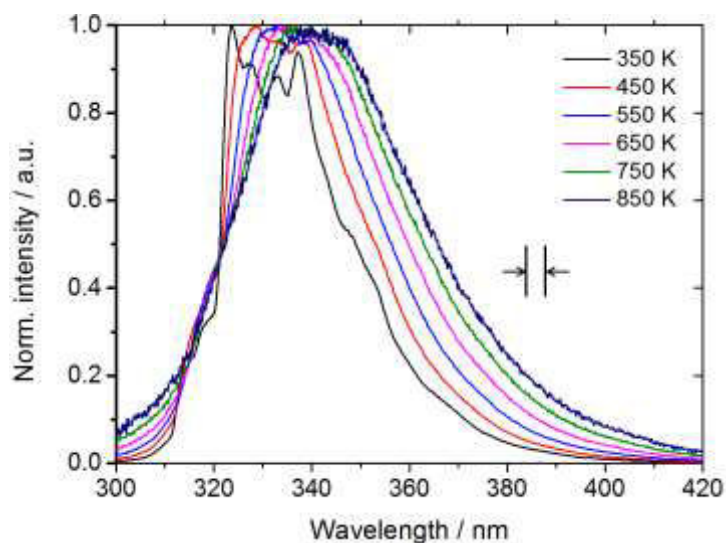


Figure 3-14: Peak-normalized 1-MN fluorescence spectra at various temperatures in 1 bar  $N_2$  bath at a 1-MN number density of  $2.16 \times 10^{19} \text{ m}^{-3}$ . The arrows indicate the spectral resolution of the detection system as the FWHM of a recorded mercury line at 254 nm.

Figure 3-15 shows temperature-dependent 1-MN effective fluorescence lifetimes meas-

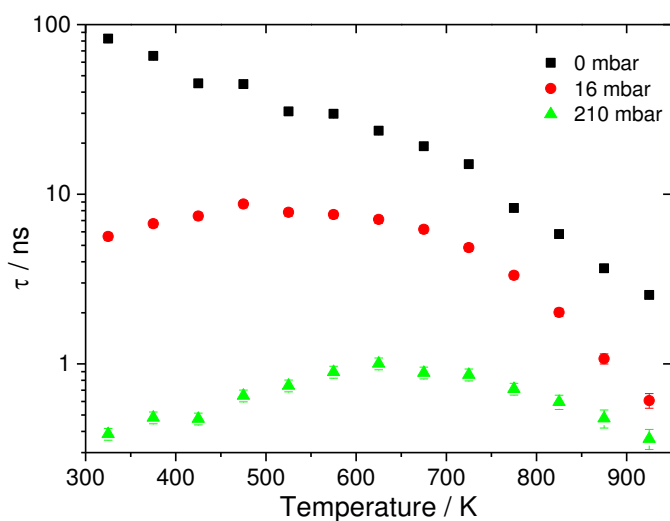


Figure 3-15: Effective fluorescence lifetime of 1-MN as a function of temperature for several  $O_2$  partial pressures in 1 bar total pressure.

ured in pure  $N_2$  (black squares) at 1 bar total pressure for 325–925 K. In contrast to *p*-DFB, 1-MN has a long fluorescence lifetime at low temperatures (325 K). This can be due to the activation of so-called “third decay channel” when an amount of excess energy is reached in the  $S_1$  state. As shown by Otis et al. [61], this third decay path is activated

due to enhanced internal conversion. This supplementary deactivation path leads to the appearance of a second lifetime component. This second lifetime is activated when excitation is accomplished with wavelengths less than 250 nm. Similarly to *p*-DFB, the 1-MN fluorescence lifetime decreases with increasing temperature. The decrease of 1-MN fluorescence lifetime, however, is stronger than for *p*-DFB.

### Influence of molecular oxygen

Collisional quenching of 1-MN by O<sub>2</sub> was investigated for a temperature range of 325–925 K for various O<sub>2</sub> partial pressures. Unlike *p*-DFB, 1-MN is highly quenched by O<sub>2</sub> as the fluorescence lifetime decreases from 82.6±1.6 ns in pure N<sub>2</sub> to 5.6±0.2 ns in 16 mbar O<sub>2</sub> at 325 K. For 16 mbar, the fluorescence lifetime dependence shows a plateau for temperatures between 325 and 680 K and then decreases further until it reaches 0.3±0.05 ns at 925 K. As the O<sub>2</sub> partial pressure increases to 210 mbar, the fluorescence lifetime becomes temperature independent ranging between 1–0.3 ns.

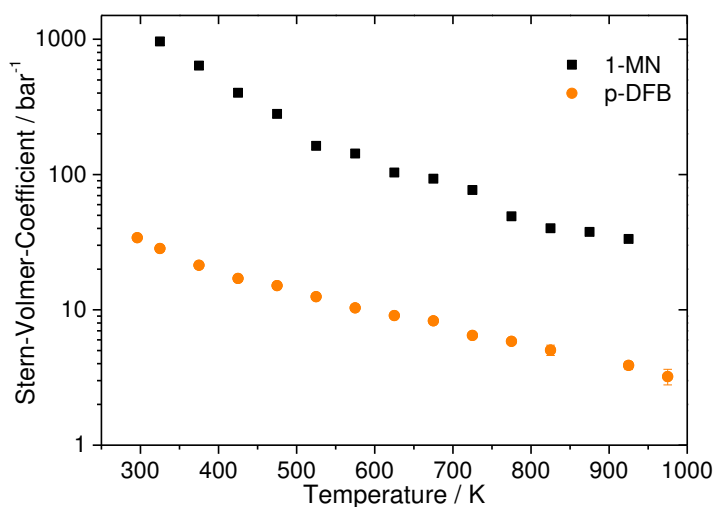


Figure 3-16: Stern-Volmer coefficient of 1-MN and *p*-DFB fluorescence at various temperatures at 1 bar.

The Stern-Volmer coefficient of 1-MN was calculated at various temperatures for a total pressure of 1 bar and compared to the coefficients of *p*-DFB. The Stern-Volmer coefficients for 1-MN are larger than those of *p*-DFB, indicating high quenching efficiency in collisions with O<sub>2</sub>. Moreover, this also supports results presented above that in air 1-MN fluorescence lifetimes are nearly unaffected by temperature.

### 3.2.3 Tracer mixture

The application in this thesis requires the simultaneous use of two tracers. Therefore, potential photophysical interaction between the two tracers must be investigated by examining the fluorescence lifetimes of the tracers in the mixture in comparison to those of the pure components. A mixture of *p*-DFB and 1-MN, with a 1:5 volumetric ratio was investigated. This ratio was selected to generate similar fluorescence intensities for both tracers in the evaporated fuel at 600 K and 9 bar (cf., section 4.2.3). The fluorescence lifetime of the tracers in the mixture were investigated for conditions that correspond to spray experiments illustrated in chapter 4.

Figure 3-17 shows a comparison of the fluorescence lifetimes of *p*-DFB and 1-MN in the tracer mixture and as pure components as a function of temperature in N<sub>2</sub> at 9 bar total pressure. The effective fluorescence lifetimes of the individual tracers were given for partial pressures of 1.2 mbar at 296 K for *p*-DFB and of 0.9 mbar at 325 K for 1-MN.

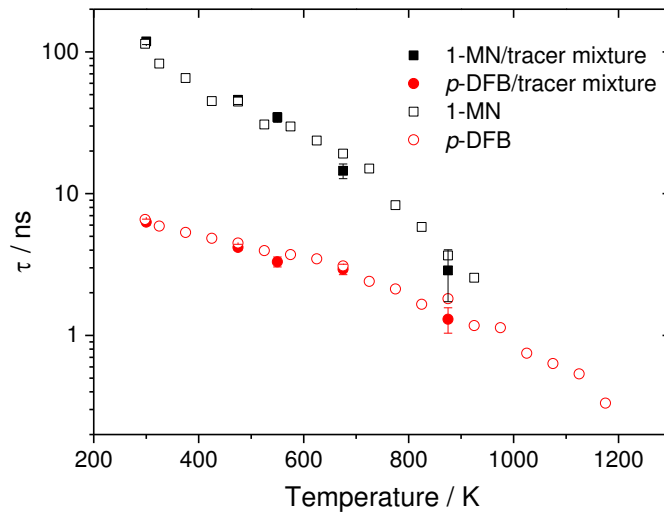


Figure 3-17: Effective fluorescence lifetimes of 1.2 mbar *p*-DFB (hollow red circles) and 0.9 mbar 1-MN (hollow black squares) investigated separately for 1 bar total pressure of N<sub>2</sub>. The solid red and black circles represent the effective fluorescence lifetimes of *p*-DFB and 1-MN respectively, derived from the tracer mixture. The mixture contains 0.3 mbar of *p*-DFB and 1.5 mbar of 1-MN.

The number density of each tracer was low enough to prevent self-quenching and thus to assume that the effective fluorescence lifetime is independent of the number density. The effective fluorescence lifetime, which is proportional to the fluorescence quantum yield, of *p*-DFB and 1-MN are comparable for measurements with individual tracers and

with a mixture of *p*-DFB/1-MN within the precision of the measurements except for 870 K where the signal-to-noise ratio is low. Regardless of the deviation at 870 K, the fluorescence lifetimes measured for the tracer mixture show good agreement with the fluorescence lifetimes of single tracers in the investigated temperature range from 296 to 650 K. This implies that there is no indication of significant photophysical interaction between the two tracers which makes them good candidates for two-tracer LIF imaging.

## **4 Quantitative two-tracer LIF for simultaneous imaging of preferential evaporation effects, temperature, and fuel concentration**

### **4.1 Measurement strategy**

The measurement strategy developed in this work is based on the use of a transparent surrogate fuel composed of three different volatility components. The fuel is then doped with two fluorescence tracers. Each tracer co-evaporates with a certain volatility end and has a distinct emission spectrum allowing for simultaneous detection of both tracers. In the absence of preferential evaporation, both tracers would appear at a fixed concentration ratio throughout the fuel cloud and the LIF-signal ratio of both tracers would be constant within the entire field of view. Deviations from a homogeneous value, thus, directly indicate regions where preferential evaporation affects the fuel composition. In addition, the information derived from the ratio images are considered quantitative since the measured ratio itself is quantitative and since the evaporation behavior of the tracer relative to the fuel component is known. The latter has been obtained by thermodynamic simulations that are not the focus of this work, but are however exploited when choosing potential tracers for the two-tracer LIF technique.

Temperature measurements are based on the red-shift of the spectrum of one of the selected tracers [62]. It is important to assess the temperature distribution across the entire jet since temperature inhomogeneities could affect the fluorescence signal via the temperature dependence of fluorescence quantum yield and therefore could affect the ratios of the two-tracer method leading to a misinterpretation in terms of preferential evaporation.

Fuel concentration fields are derived from LIF images with a method based on normalizing by the known total injected fuel mass of an image through the corresponding 3D reconstructed information [54].

This chapter is divided into three main parts. Firstly, the details of the measurement strategy, from choice of surrogate fuel and tracers to experimental apparatus and conditions are discussed. Secondly, the experimental and image post-processing methods that were applied to obtain meaningful information from LIF images are addressed. Finally, the results of measurements in vaporized fuel sprays are presented.

### **4.1.1 Choice of injector technology**

The main objective of this work is to investigate the mixing process of multi-component fuels thus providing a pertinent database for model validation. The comparison of experimental results and CFD simulations requires full characterization of the initial and the boundary conditions of the injector. The experiments were performed with an ECN multi-hole Spray G injector and a piezo-electric outward opening injector. The ECN Spray G is characterized in terms of rate of injection, internal flow, and droplet size by the ECN community [63]. The piezo-electric injector on the other hand still requires an in-depth characterization. In the section below, both injectors will be described.

#### **ECN Spray G injector**

The Engine Combustion Network (ECN) aims at improving the fundamental understanding of Diesel and gasoline spray formation and combustion in engines and works towards developing predictive models for engine optimization. The network brings together experimental and computational research for comparisons of measured and simulated results at standardized conditions [64]. “Spray G” is a gasoline spray with operating conditions corresponding to a non-reacting early injection case for spray-guided gasoline injection. The injector specifications are for modern advanced injection systems with high pressure capability. Spray G is generated by a solenoid eight-hole injector which results in a full-cone spray structure. Spray G was selected for two main reasons: (1) Most of the injectors used in SIDI engines nowadays resemble Spray G [65–67]. (2) This injector has been fully characterized, in terms of nozzle geometry, initial and boundary spray conditions before [63] which makes experimental results an appropriate database for model validation.

#### **Piezo-electric outward opening injector**

Piezo-electric fuel injectors are emerging as a crucial technology for enabling gasoline engines to meet tightening emissions and fuel economy standards. The injector used in this work is a Mercedes piezo-electric outward-opening hollow-cone injector. Numerous research has been performed on this injector because it was found to enhance the effect of preferential evaporation [8, 11, 13–15, 20, 50]. Unlike the ECN injector, the piezo-electric injector still lacks characterization which can hinder the use of experimental results as means of validation to numerical models.

#### 4.1.2 Choice of surrogate fuel and tracers

A single- and a multi-component fuel were used in this work. The use of a single-component fuel is due to the fact that the reference fuel for the ECN Spray G conditions is *iso*-octane. Preliminary experiments were therefore carried out at these conditions to investigate temperature, jet structure, and fuel distribution across the field of view for Spray G conditions and variants. *iso*-octane was doped with *p*-difluorobenzene (*p*-DFB) assuming that it behaves similarly to *iso*-octane in terms of evaporation, convection, and diffusion. *p*-DFB also allows for temperature measurements due to the red-shift of the spectrum with temperature increase (cf., section 3.1.3). For more information about experimental conditions, refer to section 4.1.3

Once the reference is set with the single-component fuel, the experiments using a multi-component fuel can then be carried out to investigate the effect of preferential evaporation of components of different volatility classes. Preferential evaporation was investigated with both, ECN Spray G and the piezo-electric injector. The formulation of the surrogate multi-component fuel mixture and the selection of fluorescent tracers based on their evaporation characteristics relative to the fuel components was not the focus of this work. These tasks were performed within the Bioptic 2 project and the results of the thermodynamic study were only used in this work. For this reason, the main principles and the results of this thermodynamic study are presented here. More details are available in [68]. The thermodynamic model takes into account the molecular structure of the components and the interactions between these molecules. First, saturated hydrocarbons have been selected according to the boiling temperature of pure compounds that represent the typical range for gasoline. Then the proportions between these compounds have been tuned to reproduce the distillation curve of commercial fuels. A three-component gasoline surrogate was designed containing *n*-pentane (purity grade  $\geq 99\%$ ), *iso*-octane (99.8%), and *n*-undecane ( $\geq 99\%$ ) that represent the light, medium, and heavy volatility groups, respectively. The mixture (36, 46, and 18% by volume) was designed to match the distillation curve of commercial gasoline measured according to ASTM D86. The three blue curves of Figure 4-1 corresponding to the left axis show the distillation curves of the measured commercial gasoline, that of the simulated surrogate mixture, and that of the measured surrogate mixture.

As for tracers, only aromatic candidates were considered to avoid the photophysical interaction known for the combination of ketones and aromatics [14]. *p*-DFB and 1-meth-

1-methyl naphthalene (1-MN) were selected to represent the light-to-medium and heavy fractions, respectively. The co-evaporation of the tracer pair with their respective components was verified using the thermodynamic calculations. Figure 4-1 shows the results of this calculation and displays the calculated evaporated fraction of the three different surrogate components and of the two fluorescent tracers (right axis of the graph) as a function of temperature. 1-MN almost perfectly follows the evaporation of *n*-undecane whereas *p*-DFB well represents the combined lighter fractions. The selected tracers allow for simultaneous imaging because their emission spectra are in two distinct spectral regions [32, 69].

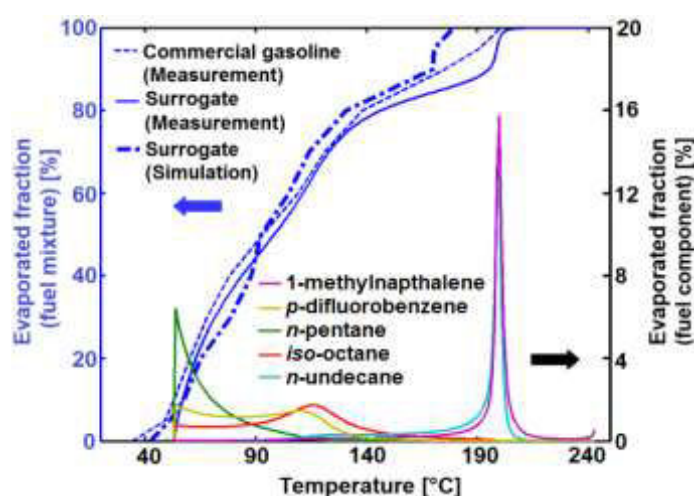


Figure 4-1: Comparison of the evaporation curves of commercial gasoline and the three-component surrogate obtained from numerical simulation and measurements (left axis). The lower curves (right axis) show the evaporated fractions of each fuel and tracer component as a function of temperature obtained from the thermodynamic calculations. Experiments and calculations are carried out at 1 bar.

When this dissertation was written, the thermodynamic simulation had only been performed in atmospheric conditions therefore limiting the possibility to quantitatively relate the fluorescent tracer measurements to fuel component composition. The work that takes into account the effect of pressure was under way. This work is therefore focusing on the quantitative measurement of tracer concentration ratios to localize regions where preferential evaporation is significant. A full quantitative analysis of the effect of preferential evaporation on the fuel mixture composition will be possible once the thermodynamic simulations are made available at pressures relevant to the experimental conditions used in this work.

### 4.1.3 Operating conditions

This work investigates the mixture formation of two different types of injectors which are the ECN Spray G injector and the piezo-electric injector. Various operating conditions were used for each injector depending on the objective of the experiments. For clarification of the structure of the following sections, these operating conditions are presented here.

Figure 4-2 schematically shows the operating conditions and their corresponding filter configurations that are used in this work. This figure can be used as a guideline throughout this chapter. In this section the focus will be on the operating conditions rather than the filter configurations which will be addressed later on in section 4.1.4.

Figure 4-2 is divided into two parts representing the two experimental campaigns carried out by using two different injectors. The left and the right side of the figure illustrate the conditions used in ECN Spray G and piezo-electric experiments, respectively. Two separate experiments were performed with ECN Spray G where each experiment required the use of a different surrogate fuel.

- In the first experimental campaign with ECN Spray G, a single-component fuel (*iso*-octane) doped with *p*-DFB was used. These investigations serve as a reference for the analysis of the mixture formation and the temperature distribution across the jet. For these measurements, two different configurations were employed. *Configuration I* (i.e., the identical filters configuration BP292/BP292) aims at providing information regarding the accuracy and precision of the whole measurement system. *Configuration T* (i.e., *p*-DFB LIF thermometry configuration BP320/BP292) enables temperature measurements across the entire field of view and consequently of fuel mass fraction fields by single-color LIF.
- In the second experimental campaign the objective was to test for the presence and observability of preferential evaporation. Therefore, a multi-component fuel was used as a surrogate fuel. Three filter configurations were used for multi-component fuel experiments. The identical filter configuration here involves two sets of filters ([BP292/BP292] and BP292/[BP292]) since the experimental setup of the multi-component fuel experiments has three detection channels and therefore the accuracy and the precision for each channel pair requires assessment. Note that the braces surrounding [BP292/BP292] and any other optical filter (e.g., [BP292]) are used to indicate that the image pair or the individual image were recorded by using the image doubler. *Configuration E* ([BP292/BP340]) aims at

identifying the effects of preferential evaporation. *Configuration T* (1-MN LIF thermometry configuration BP377/[BP340]) allows the investigation on the temperature distribution across the jet.

Both single- and multi-component fuel sprays were examined at ECN Spray G target conditions which correspond to an ambient density of  $3.5 \text{ kg/m}^3$  and an ambient temperature of 573 K. Two variants were also looked into which are 6 and  $9 \text{ kg/m}^3$  at 700 and 800 K, respectively. These variants simulate mid and late injection strategies during the compression stroke of a typical IC engine [70]. The injection pressure and duration were set to 200 bar and  $680 \text{ }\mu\text{s}$ , respectively, based on ECN standards.

Measurements carried out with piezo-electric injector involved solely the use of the multi-component fuel in order to study the effects of preferential evaporation. The filter configuration utilized for these experiments is similar to those used for multi-component fuel experiments of ECN Spray G. Measurements were performed at three operating conditions:

- **ECN Spray G thermodynamic conditions:** Allows to examine the influence of injector technology on mixture formation, temperature distribution, and preferential evaporation.
- **Temperature variations at constant gas density:** The objective behind such measurements is to look into the influence of temperature on preferential evaporation. Therefore temperature was varied between 550–700 K while keeping the density constant at  $5.2 \text{ kg/m}^3$ .
- **Gas density variations at constant temperature:** These experiments aim at examining the influence of the gas density (i.e. pressure) on preferential evaporation. Hence the density was varied between  $6.3\text{--}12.5 \text{ kg/m}^3$  at a constant temperature of 550 K.

The injection pressure and injection duration were set to 100 bar and  $600 \text{ }\mu\text{s}$ , respectively.

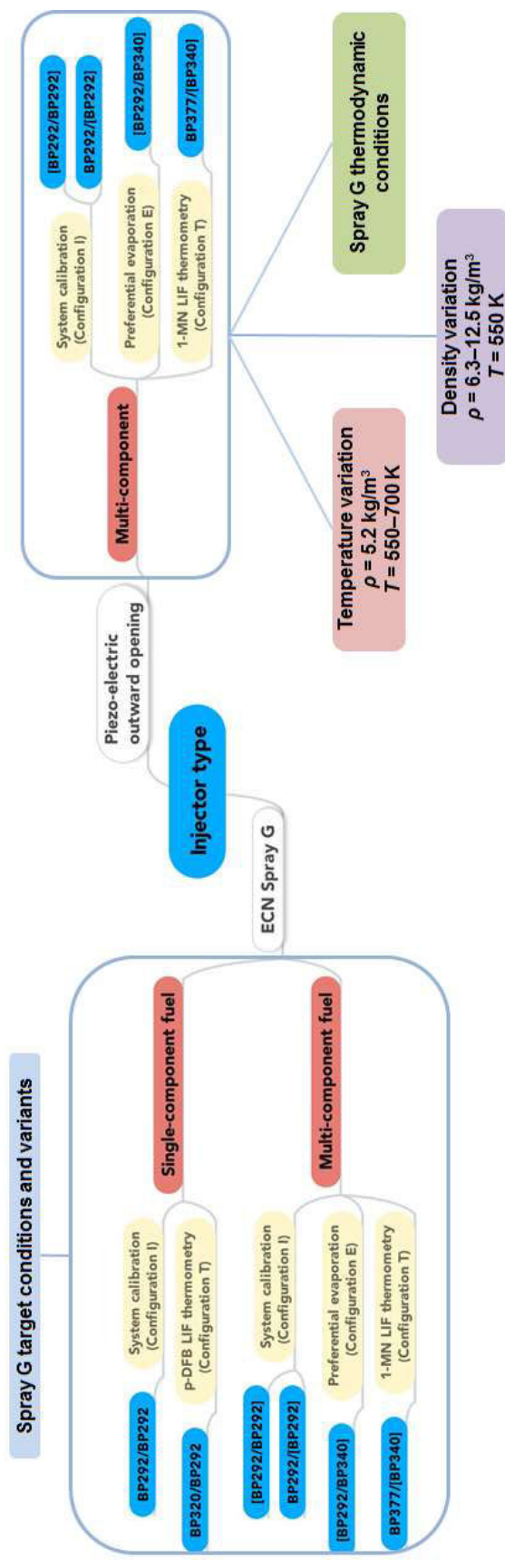


Figure 4-2: Scheme of experimental conditions and filter configurations used in this work. The type of fuel used is presented in orange boxes. The filters used for two-color measurements are given in blue boxes and the configuration and the configuration and its aim is given in yellow boxes. The blue boxes represent the filter combinations

#### 4.1.4 Experimental and optical arrangement

All measurements have been performed in an optically accessible high-pressure high-temperature pre-combustion vessel. The vessel allows the study of sprays and mixture formation under conditions similar to that of IC engines during injection. The injector is mounted on the top of the vessel. Two cylindrical sapphire windows on opposite sides of the vessel provide a field of view of  $85 \times 85 \text{ mm}^2$  while two  $65 \times 10 \text{ mm}^2$  quartz windows provide laser access perpendicularly to the viewing direction. High temperature and pressure prior to the start of injection are provided by pre-combustion of a  $\text{C}_2\text{H}_2/\text{H}_2/\text{O}_2/\text{N}_2$  mixture. After combustion, gases gradually cool down and the fuel is injected after a specific delay when the desired temperature and pressure are reached. For all experiments presented in this work, the mixture proportion was fixed so that no  $\text{O}_2$  was left after pre-combustion. Such an  $\text{O}_2$ -free environment is appropriate for evaporation studies and prevents fluorescence quenching. For further details, see [71].

As presented in the previous section a single- and a multi-component fuel were used for visualizing the mixture formation of the jet. For single-component fuel experiments, two detection channels (using two cameras) were used thus producing two images simultaneously. The multi-component fuel experiments required three detection channels which were provided by mounting an image doubler in front of one of the two cameras. In the section below, the optical arrangement corresponding to these two configurations will be addressed in details.

##### 4.1.4.1 Single-component configuration

*iso*-octane was selected as surrogate fuel for single-component experiments since its evaporation mimics that of gasoline. The objective of these experiments was to derive the fuel vapor distribution and the temperature fields of the vaporized spray simultaneously in the ECN spray G conditions.

For LIF measurements, *iso*-octane was doped with 0.03 vol% *p*-DFB which was excited by the fourth harmonic of a Nd:YAG laser (266 nm). The laser was used to form a light-sheet ( $59 \times 0.5 \text{ mm}^2$ ) that passes through the center of the fuel jet, crossing plumes 2–6 with the top of the sheet 5.2 mm away from the injector tip. Figure 4-3 shows the light-sheet position relative to the jet plume orientation. The plumes originating from eight individual holes of Spray G are numbered from 1 to 8 based on the ECN reference numeration.

The laser energy was controlled via an attenuator coupled with an energy sensor. Therefore the Q-switch timing was fixed to deliver the highest laser energy possible while the

orientation of the attenuator mirrors was changed to provide the appropriate amount of laser energy within the linear range of LIF-signal generation. Images of the laser-light sheet were recorded when the vessel is homogeneously seeded with the tracer. For this, ten consecutive injections at 7 bar and 453 K in nitrogen were realized and imaging was performed after 5 to 10 s with the mixing fan on to ensure homogeneous mixing of the tracer. A homogeneous region of interest in the laser light-sheet is selected and its absolute average LIF-signal is calculated and plotted for various laser fluences in Figure 4-4 and for each optical filter. The figures show that the fluorescence of *p*-DFB linearly depends on the laser fluence throughout the range investigated. Note that at 40 mJ/cm<sup>2</sup> the laser pulse energy does not align with the rest of the measurements. This deviation was systematically observed in all the laser fluence measurements (see for the 1-MN characterization). This can be due to a systematic problem in the measurement of the laser fluence. Hence the points at 40 mJ/cm<sup>2</sup> were not taken into account when fitting curves into data points.

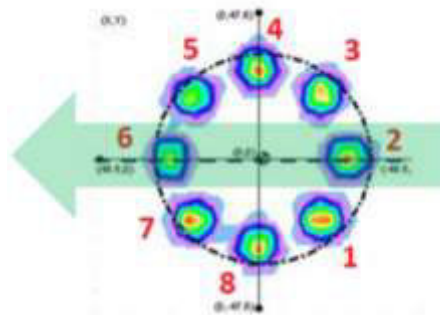


Figure 4-3: Spray orientation used for LIF imaging. The plumes originating from 8 individual holes of Spray G are numbered from 1 to 8 based on the ECN reference numeration. The green arrow indicates the direction of the laser-light sheet and the visualized spray pair 2-6.

The laser fluence curves displayed in Figure 4-4 shows that the highest fluence investigated could have been used while ensuring linear behavior of the fluorescence. However, the laser fluence was fixed at 20 mJ/cm<sup>2</sup> in order to remain consistent with the 1-MN conditions. It will be shown in that 1-MN exhibits a non-linear behavior for laser fluence higher than ~28 mJ/cm<sup>2</sup>.

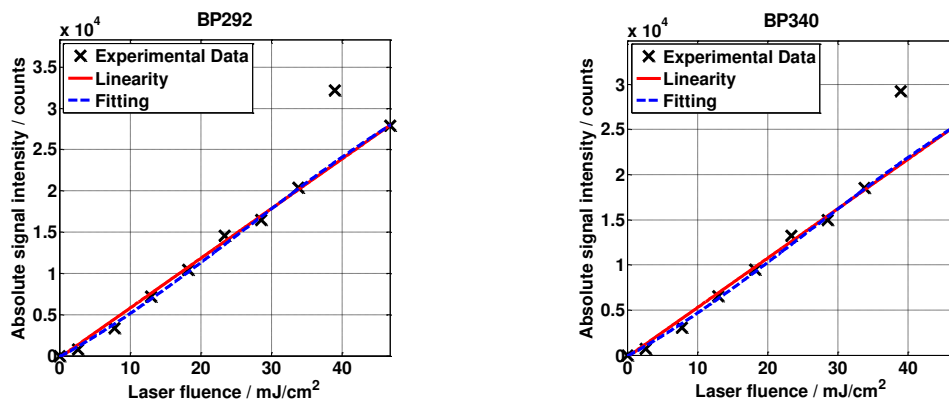


Figure 4-4: Fluence dependence of *p*-DFB signal intensity for laser excitation at 266 nm in N<sub>2</sub> at 7 bar and 453 K for filters BP292 (left) and BP320 (right). Absolute signal intensity values were derived by calculating the average of a homogenous region of interest in the laser-light sheet. The blue and the red lines are polynomial and linear fit to the data points respectively.

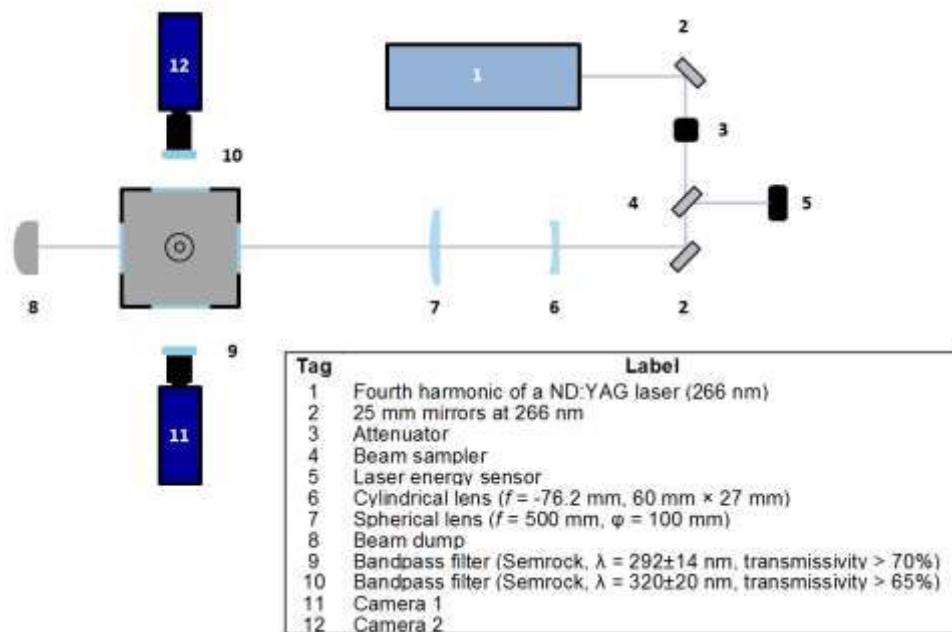


Figure 4-5: Schematic of the experimental and optical arrangement for single-component fuel experiments.

Before the laser beam enters the experiment and after it passes through the attenuator, a fraction is reflected onto an energy sensor to measure shot-to-shot laser pulse energy. The laser beam is expanded and then collimated using a cylindrical and a spherical lens, respectively, thus forming a laser light-sheet at the center of the spray. The LIF-signals

were acquired with a fast achromatic UV lens ( $f = 45$  mm,  $f/1.8$ , EADS Sodern) and imaged onto two ICCD cameras (Princeton PI-MAX 4,  $512 \times 512$  pixels) mounted opposite to each other with the vessel situated in the middle. The LIF-signal from  $p$ -DFB was detected through BP292 and BP320. The experimental arrangement and optical filter properties are illustrated in Figure 4-5.

The LIF technique used in the present work is based on tracer excitation in the vapor phase. Therefore, the presence of liquid droplets should be avoided in the measurement volume. For this purpose, preliminary Mie-scattering measurements were performed with a frequency-doubled Nd:YAG laser (532 nm) with similar light-sheet dimensions as used for tracer LIF to determine the delay after the start of injection (aSOI) where the spray in the imaged area is completely evaporated. In all experimental conditions, no droplets were observed at 2.7 ms aSOI which was therefore selected as the first timing for the LIF measurements. This timing was determined based on Mie-scattering experiments. Figure 4-6 shows the average Mie-scattering signal intensity as a function of time aSOI. The plotted signal is the absolute average signal derived from spray images performed at  $5.2 \text{ kg/m}^3$  and 550 K. This figure shows that the signal gradually decreases as time advances due to the evaporation of liquid fuel. The first timing at which the signal is relatively low in comparison to early aSOI timings is 2.7 ms. The spray orientation relative to the light-sheet for Mie-scattering experiments is identical to the spray orientation used for LIF imaging shown in Figure 4-3.

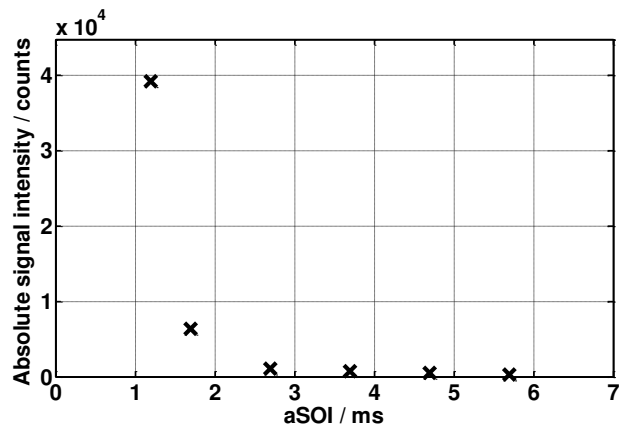


Figure 4-6: Evolution of Mie-scattering signal as a function of different aSOI timings. The absolute signal intensities were obtained by calculating the average signal across the entire field of view. No droplets were observed at 2.7 ms aSOI which was therefore selected as the first timing for LIF measurements.

Two filter configurations were used for single-component experiments: (1) *Configuration*  $T_{BP320/BP292}$  was used for temperature measurements based on two-color  $p$ -DFB with one filter centered at the peak of  $p$ -DFB LIF spectrum BP292 while the second detects the long-wavelength tail BP320 allowing to determine the BP320/BP292 ratio. This configuration requires the exact superposition (mapping) of both images to generate a meaningful image of the intensity ratio BP320/BP292. (2) *Configuration*  $I_{BP292/BP292}$  was used for optimizing the image mapping, assessing the accuracy and precision, and calibrating relative sensitivities (cf. sections 4.2.4 and 4.3.1). Two identical bandpass filters (BP292) were placed on both cameras and the ratio of the nominally identical images BP292/BP292 allows to assess experimental limitations.

Regarding fuel concentration fields of Spray G, they were obtained from images acquired from a single camera. The fuel concentration fields were then derived by applying the normalization method (cf. section 4.2.1) to images acquired with BP292 filter.

#### 4.1.4.2 Multi-component configuration

The main difference between the single- and the multi-component configuration is that in the latter, one of the ICCD cameras was coupled to an image doubler (LaVision) therefore allowing three images to be recorded simultaneously. The experimental arrangement is displayed in Figure 4-7.

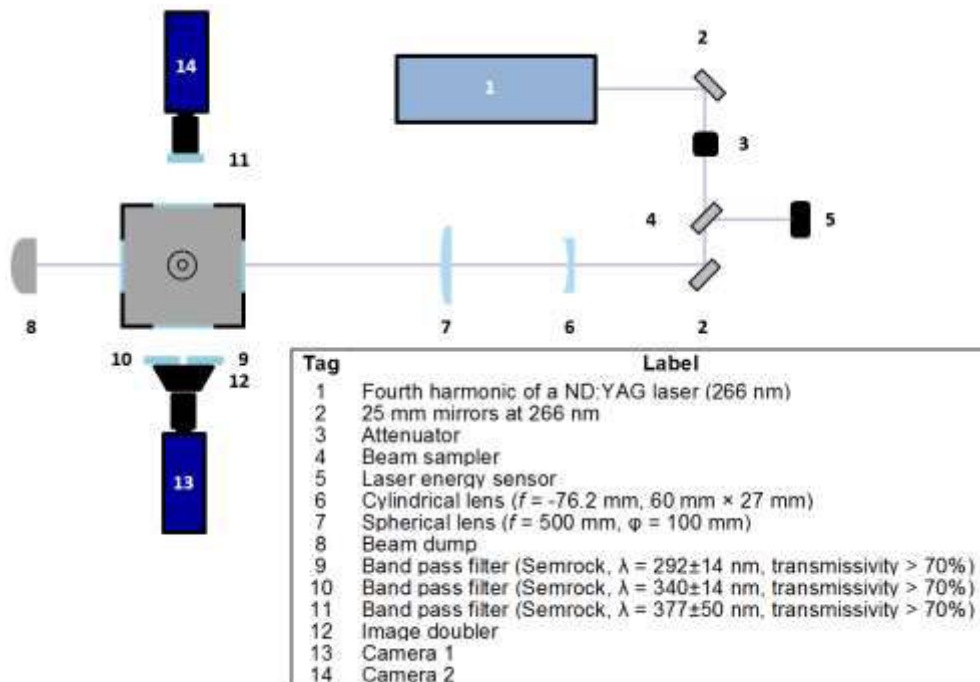


Figure 4-7: Schematic of the experimental and optical arrangement for multi-component fuel experiments.

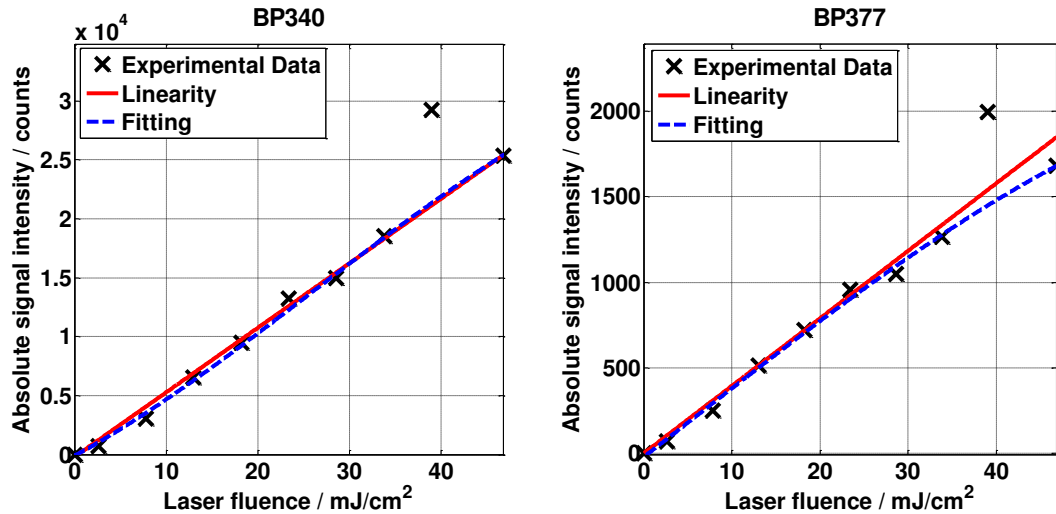


Figure 4-8: Fluence dependence of the 1-MN signal intensity for laser excitation at 266 nm in  $N_2$  at 7 bar and 453 K for filters BP340 (left) and BP377 (right). Absolute signal intensity values were derived by calculating the average of a homogenous region of interest in the laser-light sheet. The blue and the red lines are polynomial and linear fit to the data points respectively.

The procedure detailed in the single-component fuel section regarding laser fluence was also used to determine the required laser fluence for multi-component experiments. represents the fluence plot of BP340 filter which shows that the LIF-signal is linear for all tested laser fluence. For BP377 filter, the signal starts to deviate from linearity at 28  $mJ/cm^2$ . Therefore, the laser fluence was set to 20  $mJ/cm^2$  to obtain a good signal-to-noise ratio while ensuring that LIF-signal is in the linear range. Four different filter configurations were used for these experiments: *Configuration*  $E_{[BP292/BP340]}$  was employed to assess preferential evaporation by simultaneously collecting the signal of both tracers on each channel of the image doubler. The filters used for the detection of *p*-DFB and 1-MN LIF were BP292 nm and BP340, respectively.

The main difference between the single- and the multi-component configuration is that in the latter, one of the ICCD cameras was coupled to an image doubler (LaVision) therefore allowing three images to be recorded simultaneously. The experimental arrangement and the properties of the optical filters are given in Figure 4-7. The procedure described in the single-component fuel section regarding laser fluence was also used to determine the required laser fluence for multi-component experiments. The signal behavior as a function of laser fluence was investigated at 7 bar and 453 K. represents the fluence plot of BP340 filter which shows that the LIF-signal is linear for all tested laser fluence. For BP377 filter, the signal starts to deviate from linearity at 28  $mJ/cm^2$ . Therefore, the laser fluence was set to 20  $mJ/cm^2$  to obtain a good signal-to-noise ratio while ensuring that the LIF-signal is in the linear range. Four different filter configurations were

used for these experiments: *Configuration*  $E_{[BP292/BP340]}$  was employed to assess preferential evaporation by simultaneously collecting the signal of both tracers on each channel of the image doubler. The bandpass filters used for the detection of *p*-DFB and 1-MN LIF were BP292 and BP340, respectively.

This configuration requires the exact superposition (mapping) of both images to generate a meaningful image of the intensity ratio [BP292/BP340]. *Configuration*  $I_{[BP292/BP292]}$  was used for optimizing the image mapping, assessing the accuracy and precision, and calibrating the relative sensitivities of the image pair acquired with the image doubler. Therefore, identical filters (BP292) were placed on each detection channel of the image doubler where ratios of the nominally identical images [BP292/BP292] allows to assess experimental limitations of each pair of the detection channels. *Configuration*  $T_{BP377/[BP340]}$  was used for temperature measurements based on 1-MN two-color LIF with one filter centered at the peak of the 1-MN LIF spectrum (BP340) while the second detects the long-wavelength tail (BP377) allowing to determine BP377/[BP340] ratio. Similarly, *Configuration*  $I_{BP292/[BP292]}$  was used to optimize image mapping and calculate the measurement precision and accuracy generated by image pair BP292/[BP292].

## 4.2 Experimental methods and image post-processing

### 4.2.1 Normalization method to obtain spatially-resolved fuel concentration maps

Fuel concentration maps are derived from LIF images with a method based on normalizing by the total injected fuel mass of a 2D LIF image through the corresponding 3D reconstructed information. For more details refer to Ref. [54]. The normalization method is based on the following hypotheses:

- (1) The LIF intensity is proportional to the fuel concentration and the incident laser energy
- (2) The spray is symmetric with respect to the nozzle axis (axisymmetric) enabling the reconstruction of 3D distribution from 2D information
- (3) The entire width of the spray is captured by LIF imaging so that the total injected fuel mass can be determined using assumption (2)

The accuracy of this method and the validity of these hypotheses will be discussed in section 4.3.2.

In the formulation of the first hypothesis, the effect of temperature on the effective fluorescence yield, which includes effects of the absorption cross-section and the quantum

yield, is neglected. In this initial phase the temperature effect on the fluorescence quantum yield was neglected before being corrected for in a second step as discussed in the following section. This two-step process was adopted to simplify the analysis. As a consequence the LIF-signal is expressed as follows:

$$S_{\text{fl}}(x, y) = \eta' E_{\text{laser}}(y) c_f(x, y) \quad (4-1)$$

where  $S_{\text{fl}}$  is the absolute signal intensity,  $x$  is the radial distance from the nozzle axis to the measurement location and  $y$  is the axial distance from the nozzle.  $\eta'$  is the proportionality factor that contains detection efficiency and calibration constants,  $E_{\text{laser}}$  is the normalized fluence distribution in the light-sheet at ordinate  $y$ , and  $c_f$  is the fuel concentration at coordinate  $(x, y)$  in  $\text{kg}/\text{m}^3$ . Determining the entire fuel from the two-dimensional measurement within a cross section imaged via the light-sheet technique is based on the assumption of axial symmetry. Using Eq. (4-1) the 3D reconstruction of the 2D information based on hypothesis (2) yields:

$$I_v = \iiint_{-\pi}^{\pi} \frac{S_{\text{fl}}(x, y)}{E_{\text{laser}}(y)} x d\theta dy dx = 2\pi \iint \frac{S_{\text{fl}}(x, y)}{E_{\text{laser}}(y)} x dy dx \quad (4-2)$$

where  $I_v$  is defined as the hypothetic spatially-integrated LIF-signal in case the entire volume was illuminated by laser light. This quantity is proportional to the amount of fuel in the section of the jet that corresponds to the height and the location of the laser light sheet.

Hypothesis (3) in combination with Eq.(4-1) and (4-2) results in:

$$\eta' = \frac{I_v}{m_{\text{fuel}}} \quad (4-3)$$

where  $m_{\text{fuel}}$  is the total injected fuel mass in kg. Combining Eq. (4-4) and (4-1) yields the relation between fuel concentration and absolute LIF intensity:

$$c_f(x, y) = \frac{S_{\text{fl}}(x, y)}{\eta' E_{\text{laser}}(y)} \quad (4-4)$$

Note that in Eq. (4-4), the absolute LIF-signal  $S_{\text{fl}}$  is assumed to be independent of temperature and therefore fluorescence quantum yield  $\Phi_{\text{fl}}$  is considered spatially invariant. In reality, the fluorescence intensity is lower at high temperatures than at low temperatures due to the temperature dependence of the fluorescence quantum yield. Therefore,

for an improved determination of the fuel concentration in the jet, the temperature dependence of  $\Phi_{fl}$  was corrected later (cf. section 4.2.2) by replacing the initial assumption of constant fluorescence quantum yields by temperature-dependent values thus leading to the corrected fuel concentration maps.

### Image post-processing

A post-processing routine was developed to calculate the fuel-concentration fields based on the methodology explained above. Firstly, the laser pulse energy variation in the light-sheet was obtained from images when the vessel was homogeneously filled with the tracer at low concentration. For this, ten consecutive injections of the surrogate fuel and tracer mixture at 7 bar and 453 K in nitrogen were realized and imaging was performed after 5 to 10 s with the mixing fan on to ensure homogeneous mixing. The resulting image was then averaged along the  $x$ -axis to obtain a one-dimensional profile that represents the energy variation in the laser profile  $E_{laser}(y)$  that is then used for correcting the individual images. The tracer concentration was low enough to ensure that laser attenuation was insignificant. The instantaneous images do not show any asymmetry in the absolute LIF-signal intensity across the laser path. Each individual image was then corrected for the pixel-to-pixel sensitivity of the detector using a flat-field image obtained from a homogeneous laser-light sheet. Shot-to-shot variations in the laser energy were corrected using information determined with the laser energy sensor. For measurement series in the fuel jet, average LIF image are then calculated, typically for 20 individual measurements. Prior to calculating ratios, a threshold was set that eliminated signal from areas in the image with intensities less than 10% of the maximum to avoid non-physical values due to calculation of ratios from images with locally poor signal-to-noise ratios.

#### 4.2.2 Calculation of temperature fields based on an adiabatic mixing model

The adiabatic mixing model of Espey et al. [72] that was applied to derive the local temperature of an evaporated fuel jet is based on the assumption that the mixing between the fuel and the ambient air does not involve heat transfer without mass transfer (i.e., adiabatic mixing). Therefore, the model assumes thermodynamic equilibrium to determine the adiabatic mixing temperatures  $T_{mix}$  from the following relation:

$$\int_{T_{mix}}^{T_{amb}} c_{p,a} dT = (FAR)_m \cdot \left[ \int_{T_{Fl,ini}}^{T_{int}} c_{p,Fl} dT + h_{v,T_{ini}} + \int_{T_{int}}^{T_{mix}} c_{p,Fv} dT \right] \quad (4-5)$$

The term  $\int_{T_{\text{mix}}}^{T_{\text{amb}}} c_{p,a} dT$  signifies the decrease of thermal energy of the ambient gases during energy transfer with the fuel. The ambient gases temperature drops from the initial temperature  $T_{\text{amb}}$  (i.e., measured with a thermocouple) to the adiabatic mixing temperature  $T_{\text{mix}}$ .  $c_{p,\text{Fl}}$  is the ambient gas molar specific heat of the liquid fuel (where Fl stands for liquid fuel).  $c_{p,\text{Fv}}$  are is molar specific heat of the gas fuel (where Fv stands for liquid fuel). The term  $(FAR)_m$ , also known as  $FAR$ , is the fuel-air ratio by mass. By applying the ideal gas law,  $FAR$  can be then derived from the fuel mass concentration by the following relation:

$$(FAR)_m = \frac{c_f}{c_a} = \frac{c_f}{\frac{pM_a}{RT_{\text{mix}}} - c_f \frac{M_a}{M_f}} \quad (4-6)$$

The term  $\left[ \int_{T_{\text{Fl,ini}}}^{T_{\text{int}}} c_{p,\text{Fl}} dT + h_{v,T_{\text{ini}}} + \int_{T_{\text{int}}}^{T_{\text{mix}}} c_{p,\text{Fv}} dT \right]$  signifies the increase in thermal energy during energy exchange with the ambient gases when the fuel temperature rises from the initial fuel temperature at injection  $T_{\text{Fl,ini}}$  to the adiabatic mixing temperature  $T_{\text{mix}}$  passing through the intermediate temperature  $T_{\text{int}}$  where the change of state from liquid to gas takes place (i.e., the boiling point at the respective pressure).  $h_{v,T_{\text{ini}}}$  expresses the effective enthalpy of evaporation assuming that the fuel evaporates from the start of injection temperature  $T_{\text{ini}}$  and after evaporation reaches the gas-phase temperature.

The adiabatic mixing temperature provides an evaluation of the local temperature in the fuel jet where all the fuel is vaporized. This model requires ambient temperature, fuel-air ratio by mass,  $FAR$ , and a preliminary estimation of the adiabatic mixing temperature as input parameters. The ambient temperature used in the adiabatic mixing model is based on temperature measurements previously performed in the vessel using a thermocouples. As for the  $FAR$ , it was spatially resolved by using the fuel concentration maps that will be presented in section 4.3.2. The adiabatic mixing temperature field is then determined iteratively. This field represents the zeroth-order temperature field. This field was then used to replace the initial assumption of constant fluorescence quantum yield by temperature dependent values leading to a first-order correction in local fuel mass. This again led to an improved temperature field. This procedure was performed iteratively until no further changes occurred resulting in a spatially resolved temperate field from single-line LIF with adiabatic mixing assumption which will be denoted hereafter as  $T_{\text{mix}}$ . Note that the various sources of uncertainty in this procedure will be discussed in section 4.3.2.

### 4.2.3 Simultaneously imaging of preferential evaporation and temperature using two-tracer LIF

The technique presented in this work is capable of imaging preferential evaporation in a multi-component fuel based on the simultaneous detection of *p*-DFB and 1-MN fluorescence tracers for which thermodynamic calculations showed that they have complementary evaporation characteristics similar to high- and low-volatility components of the multi-component fuel. Relative variations in the spatial distribution of fuel components as a consequence of preferential evaporation were determined from the ratio of LIF-signals measured within two distinct spectral bands (i.e., at 292 and at 340 nm). However, tracer LIF strongly depends on temperature [6]. Therefore, any temperature inhomogeneities could affect the ratios of the two-tracer method leading to a misinterpretation in terms of preferential evaporation. Therefore, LIF thermometry was conducted simultaneously with preferential evaporation experiments to investigate the variations in temperature across the field of view.

As mentioned in section 4.1.4.2, imaging was performed using two ICCD cameras. An image doubler was mounted in front of one of the cameras therefore generating two images from a single camera. This allows for the simultaneous imaging of preferential evaporation and LIF thermometry. Optical filters centered at the peak of each tracer spectra (292 nm for *p*-DFB and 340 nm for 1-MN) were placed in front of the image doubler. The ratio derived from these two channels (i.e., BP292/BP340) was used to assess preferential evaporation. An optical filter that detects the signal originating from the long-wavelength tail of 1-MN (i.e., BP377) was mounted in front of the second camera. The temperature distribution across the jet was obtained firstly by computing the absolute LIF-signal ratio image of BP377/BP340 and secondly by applying the calibration curve which was calculated by convoluting each optical filter with 1-MN spectra (cf., Eq. (4-10)). The accuracy and precision of the method, which will be illustrated in section 4.2.4, were characterized by determining the LIF-signal ratio within the three identical spectral bands.

Note that for experiments that were carried out with *iso*-octane as surrogate fuel, only fuel concentration and temperature fields were investigated. Indeed in the case of a single-component fuel, preferential evaporation does not exist. Therefore, the image doubler was demounted leading to a two detection path experimental setup. Since *p*-DFB was selected as a tracer for single-component fuel experiments, a filter centered at the peak of its spectra (BP292) and at its long-wavelength tail (BP320) were mounted in front of each camera (refer to Figure 4-5 for filter properties). The absolute LIF-signal ratio

BP320/BP292 is then calculated and later transformed into a temperature field by applying the calibration curve derived from  $p$ -DFB spectra (cf. section 4.2.2).

#### **4.2.4 Error assessment and system calibration**

For quantitative measurements of preferential evaporation and temperature with two-tracer LIF-signal ratio, it is important to determine the measurement accuracy and precision. This information was determined following a methodology initially described in Ref. [58]. It is based on the hypothesis that the measurement accuracy and precision are mainly affected by (1) interfering LIF-signal from the surrogate fuel, (2) fluorescence cross-talk between both signal channels (this only applies to two-tracer LIF), (3) incorrect mapping of the images, (4) variation in pixel-to-pixel sensitivity between the collection paths, and (5) shot noise. Note that other error sources may exist (i.e., spatial non-uniformity of the transmission of optical filters due to variations in viewing angle, spatial inhomogeneity of laser energy, etc.) but their effects are considered to be minor with respect to the error sources stated earlier.

Concerning LIF interference (1) and cross-talk (2), specific experiments are performed either without tracer or with one tracer only to determine the corresponding error sources. Concerning the other error sources (3 to 5), the global principle of the methodology is to carry out preliminary LIF imaging in conditions similar to that of the measurements, but with a different filter configuration. Instead of using filters centered on two different wavelength ranges, identical filters are used on the two collection path. In such configuration, the two collection channels should theoretically provide identical images. However, since error sources (3) to (5) will affect imaging, differences between the two images can appear. Because the theoretical result is known (identical images), the deviation from this theoretical outcome is a direct measurement of the effect of the error sources. The results obtained from identical filters configuration is then transposed to the different filters configuration.

Two types of measurements were carried out for this analysis: (1) LIF images of the fuel jet recorded under similar conditions to those of two-tracer LIF imaging and (2) flat-field images acquired with the laser-light sheet. The jet images are used to optimize image mapping. The flat-field images are used to correct for variations in pixel-to-pixel sensitivity. The final result is used to assess the contribution of random error due to shot noise and imperfect corrections for the previous effects. Note that the flat-field images of the laser-light sheet also serve as *ex situ* calibration of the relative sensitivity of the two collection systems. Using this calibration prevents the need of *in situ* calibration for the

tracer-LIF thermometry since sensitivity differences between the various collection channels are taken into consideration. The results regarding random error will be reported in section 4.3.1.

### Optimized image registration

Any optical diagnostics method that relies on computing the signal ratio from an image pair requires a precise superposition of two images. For this reason, a reliable image mapping technique is necessary. In this work, image mapping was firstly done by using a reference grid image acquired by both cameras. The reference grid images were compared to each other resulting in a transformation matrix. This transformation matrix was then applied to spatially adjust one image (also known as input image) with respect to the other (base image). The transformation matrix is described as follows:

$$\mathbf{T} = \begin{bmatrix} sc & -ss & 0 \\ ss & sc & 0 \\ t_x & t_y & 1 \end{bmatrix} \quad (4-7)$$

$$sc = N \times \cos(\alpha)$$

$$ss = N \times \sin(\alpha)$$

The transformation matrix  $\mathbf{T}$  contains two translation factors, horizontal and vertical translation, denoted by  $t_x$  and  $t_y$ , respectively. The variables  $N$  and  $\alpha$  represent the scaling and rotation factor, respectively.

To verify that the applied image mapping technique functions properly, a signal intensity correlation is plotted. The correlation plot also known as scatter plot is a graph that plots the pixel intensities of the input image (i.e., transformed image) on the vertical axis and the pixel intensities of the base image on the horizontal axis. Figure 4-9 shows exemplary correlation plots derived from jet images recorded with identical optical filters (BP292). By discretizing the scatter plot in the  $x$ -axis, the mean (dashed line) and the standard deviation (solid lines) are determined as shown in Figure 4-9. Note that  $\sigma_R$  displayed in Figure 4-9a is a representation of the relative dispersion around the mean value. However, to determine the global  $\sigma_R$ , the standard deviation of the ratio image of the jet needs to be calculated by taking into account the entire field of view.

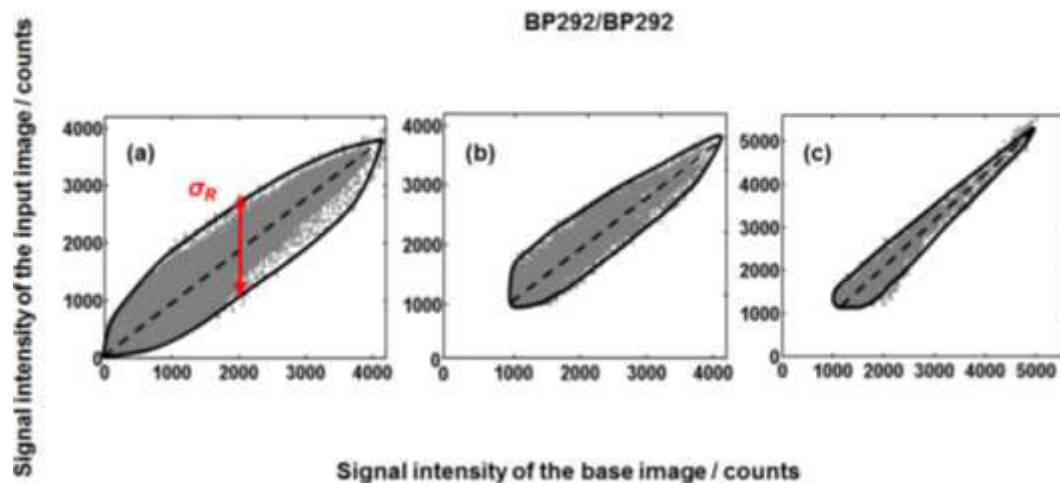


Figure 4-9: Exemplary signal intensity correlation plots for an image pair obtained by *Configuration I<sub>BP292/BP292</sub>* (a) after image mapping using a reference grid image, (b) after optimizing of the spatial adjustment according to [73], and (c) after additional flat-field correction.

Ideally, when two images are perfectly mapped, the correlation plot should result in a straight line with no dispersions around the mean. In reality, however, even after applying the transformation matrix, the correlation plot still suffers from a high dispersion ( $\sigma_R$ ) as shown in Figure 4-9a. image does not sufficiently yield in adequate results. Therefore, an optimized image mapping technique suggested in Ref. [58] was applied in this work. To improve image registration, the four transformation variables ( $t_x$ ,  $t_y$ ,  $N$  and  $\alpha$ ) were varied independently until the smallest  $\sigma_R$  was reached. This was done iteratively until no further changes occurred for each variable. Figure 4-9b shows that applying the optimized image registration leads to a decrease in  $\sigma_R$ . Figure 4-9c shows the correlation plot after it underwent flat-field correction. Flat-field correction is essential since it further minimizes the dispersions around the mean and consequently corrects for the differences in sensitivity between the detection paths.

### Correcting for pixel-to-pixel sensitivity

To correct for the pixel-to-pixel sensitivity of both cameras, flat-field LIF images of the laser light-sheet were obtained by using identical filters configuration. This correction also serves for system calibration due to the differences in sensitivity between the detection paths (i.e., the difference in sensitivity in both channels of the image doubler and also in the two camera detectors). Therefore, flat-field images were acquired when the vessel was homogenously seeded with the tracer. For this, ten consecutive injections at 7 bar and 453 K in  $N_2$  were done and imaging was performed after 5 to 10 s with the

mixing fan on to ensure homogenous mixing of the tracer. Then, 30 instantaneous images were recorded and their ensemble average was calculated. The average image was then normalized by a mean that is calculated from the most homogenous region of interest found in the laser-light sheet. The correction was applied by multiplying each image with its own flat-field image therefore resulting in an additional decrease in dispersion (cf., Figure 4-9c).

### **System calibration (*ex situ* calibration)**

The flat-field correction described in the previous section not only serves as a correction for pixel-to-pixel sensitivity, but also corrects for the difference in sensitivity between the detector of each camera. Because these flat-field images were obtained using identical filters configuration, the acquired image also accounts for the difference in sensitivity between the two detection channels. Similarly, each detection channel of the image doubler has a different level of sensitivity and therefore was calibrated separately through flat-field images of the laser-light sheet acquired by the image doubler. The black dashed line plotted in Figure 4-9 describes the difference in sensitivity of one detection channel with respect to the other. Each detection path has its own sensitivity function. In this work three different functions (i.e., *Configuration*  $I_{BP92/BP292}$ , *Configuration*  $I_{[BP292/BP292]}$  and *Configuration*  $I_{BP292/[BP292]}$ ) were calculated and then applied to correct LIF-ratio images that were used to assess preferential evaporation and temperature distribution. This *ex situ* calibration allows for direct transformation of LIF-ratio images to temperature images knowing that the temperature calibration curves were corrected by the transmission characteristics of the collection optics.

### **Fluorescence cross-talk for surrogate fuel and two-tracer LIF**

Non-fluorescing components were selected for the multi-component surrogate fuel. However, fluorescence may occur due to impurities of the components (specified with  $\geq 99\%$  purity). Therefore, prior to tracer-LIF experiments with single- and multi-component fuel, the background fluorescence intensity that is caused by the surrogate without tracers was measured under otherwise identical conditions. The interferences were found to be negligible in all channels (292, 320, 340, and 377 nm).

Prior to introducing the two tracers into the fuel simultaneously, each tracer was added separately to assess the signal cross-talk and to determine the best tracer concentration. Figure 4-10 shows individual LIF images obtained at 600 K by introducing 0.015 vol% *p*-DFB and 0.075 vol% 1-MN separately. With these proportions, similar signal levels were obtained, which is important because of the limited dynamic range of the cameras used.

The signal cross-talk of  $p$ -DFB and 1-MN to the respective other channel was 8 and 6%, respectively. This signal contribution due to cross-talk was corrected for before deriving final results of preferential evaporation. Laser attenuation was found negligible in all cases. The instantaneous images do not show any asymmetry in the absolute LIF-signal intensity across the laser path.

For conditions presented in this work, the chosen bandpass filters provided a good compromise for single-shot measurements. The cross-talk could have been further decreased by using narrower bandpass filters at an expense of signal intensity. Based on an analysis of the fluorescence emission spectra of either tracer, the cross-talk of 1-MN in the  $p$ -DFB channel can be reduced by 50 and 90% when reducing the bandwidth of the 292-nm filter by 3 and 6 nm at an expense of  $\sim 10$  and  $\sim 40\%$  of the  $p$ -DFB LIF-signal, respectively. The cross-talk of  $p$ -DFB in the 1-MN channel can be reduced by 50 and 90% when reducing the bandwidth of the 292-nm filter by 3 and 6 nm at an expense of  $\sim 17$  and  $\sim 35\%$  of the 1-MN LIF-signal, respectively.

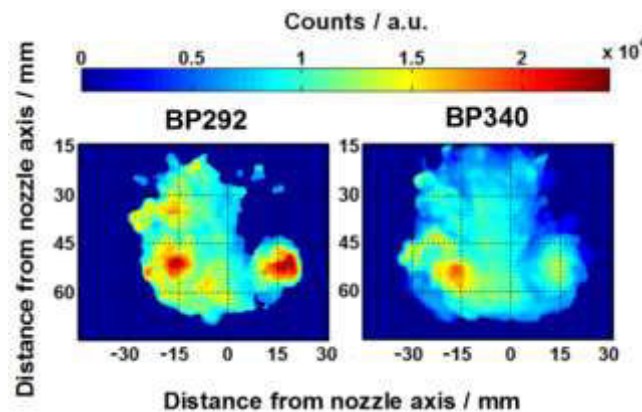


Figure 4-10: Exemplary LIF images at 600 K of the signal intensity related to 0.015 vol%  $p$ -DFB and 0.075 vol% 1-MN. Tracers were introduced separately into the multi-component fuel to determine the best concentration for each tracer.

## 4.3 Results and discussion

### 4.3.1 Error Assessment

One of the main challenges of this work is to achieve quantitative measurements in harsh engine-relevant conditions (i.e., high-temperature high-pressure). This implies that the measurement accuracy and precision have to be determined. The measurement accuracy indicates how close the measurement of a certain quantity is to its true value. The precision describes the statistical variation of measurements.

In the present work, a methodology is developed to determine the accuracy and precision of preferential evaporation and jet temperature measurements. The principle of the methodology adopted is the following:

The accuracy is determined by comparing the measured value to that determined from a second measurement technique, when available. For the assessment of the accuracy of temperature measurements, LIF thermometry results are compared to thermocouple calibration measurements of the vessel according to a methodology described below. As for the accuracy of preferential evaporation measurements, there is no second measurement technique available and therefore, the measurements are compared to another set of experiments performed at similar conditions for which the results are known. For this purpose, experiments were performed with identical filters at conditions similar to preferential evaporation experiments. In case of ideal image superposition, the ratio over the entire jet should be centred at unity. The accuracy of preferential evaporation measurements is determined by calculating the standard deviation across an averaged two-tracer LIF-ratio image acquired with identical filters.

The precision is also determined from measurements with identical filters. The error sources that are detected with this configuration will also affect the measurement configurations that use different filters to visualize preferential evaporation and temperature distribution. Therefore, the precision of temperature and preferential evaporation measurements is determined from the standard deviation of a two-color LIF-ratio standard deviation image derived from a set of instantaneous jet images.

In this section, the methodology for determining the accuracy and precision of temperature measurements is addressed. For temperature assessment, thermocouple measurements of the ambient gases are available and therefore compared with the LIF thermometry results. However the schematic Figure 4-11 illustrates the difficulty behind determining the temperature measurement accuracy. The schematic shows a temperature profile in the jet and the surrounding ambient gases. The temperature in the jet is lower than the ambient gases due to evaporation and mixing of the colder fuel with the hot ambient gases. Generally, the accuracy is assessed by comparing temperature measurements with a second measurement technique. However in the present case, the thermocouple measurements provide information in a different location than that of the jet. Therefore the direct comparison of thermocouple measurements with LIF thermometry results is not fully accurate since thermocouple measurements do not represent the temperature

inside the jet. In the present work, the temperature accuracy will be determined in two steps.

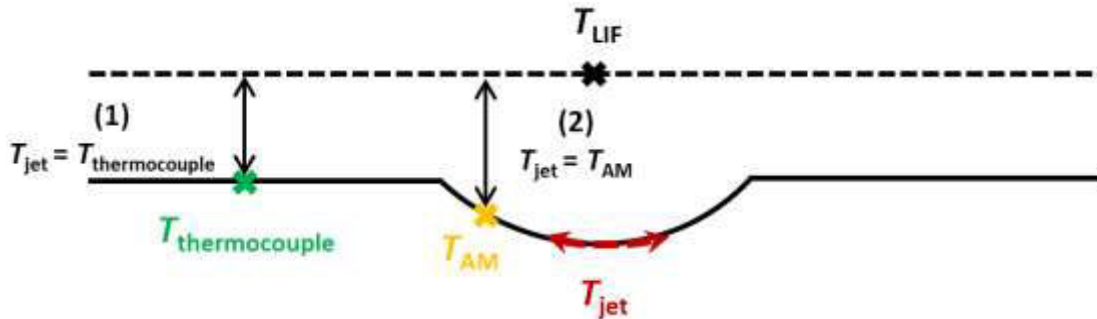


Figure 4-11: Schematic illustrating temperature profile inside the vessel and the two methods adopted to quantify the accuracy of temperature measurements.  $T_{\text{thermocouple}}$  is the ambient vessel temperature measured by thermocouples.  $T_{\text{jet}}$  is the jet temperature which is unknown.  $T_{\text{LIF}}$  is the average temperature measured by LIF thermometry.  $T_{\text{AM}}$  is the average temperature calculated from the adiabatic mixing temperature fields.

Firstly, the temperature accuracy is determined by assuming that the temperature in the jet is equal to the temperature ambient gases. This is a simplifying hypothesis that provides a first estimation of temperature accuracy in the absence of information regarding the temperature distribution in the jet. In section 4.3.2, information related to the jet temperature derived from temperature fields based on the adiabatic evaporation and mixing assumption will be presented. The assessment of the measurement accuracy is then improved by comparing the mean jet temperature obtained from LIF thermometry to that obtained from the adiabatic mixing temperature fields.

Similarly to the precision of preferential evaporation measurements, the temperature precision is determined by calculating the standard deviation of the LIF-ratio image obtained in identical filters configuration. This standard deviation is then converted to temperature using the relation between temperature and LIF-ratio obtained from the spectral calibration data.

#### 4.3.1.1 Determining the accuracy

In this work, two experimental campaigns were performed based on the type of fuel utilized (i.e., single- or multi-component fuel). Consequently, the experimental and optical arrangement was altered. For single-component fuel experiments, two cameras coupled with optical filters were used thus resulting in two detection channels. From these experiments, the temperature and the fuel concentration fields were determined. As for multi-component fuel experiments, two cameras were used where one of the cameras was

coupled with an image doubler. The image doubler results in two images each having a resolution of 256×256 pixels. This allows for the simultaneous acquisition of three images (i.e., three detection channels). Both detection channels of the image doubler were used to visualize preferential evaporation while one channel of the image doubler was paired with the other camera in order to determine the temperature distribution across the jet. The accuracy was therefore determined for each optical arrangement according to the methodology described above.

*Temperature accuracy in the single-component fuel configuration*

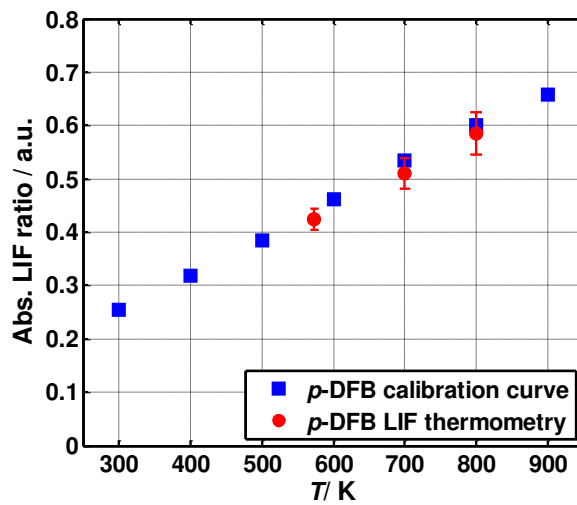


Figure 4-12: Measured LIF-signal ratio from *Configuration*  $T_{BP320/BP292}$  (red circles) as a function of ambient temperature measured by thermocouples in comparison to spectroscopy cell data (blue squares) obtained by convoluting BP292 and BP320 with *p*-DFB spectrum at various temperatures. Absolute LIF-signal ratios were calculated from average jet images performed with ECN Spray G. Error bars represent the measurement uncertainty [74].

For single-component fuel experiments, the objective was to perform two-color LIF thermometry (*Configuration*  $T_{BP320/BP292}$ ) and to calculate the fuel concentration across the vaporized spray. The temperature distribution was investigated by two-color *p*-DFB thermometry. Average images were calculated from 15 measurements taken at Spray G conditions and variants. Therefore the absolute two-color LIF-ratio was derived from average images and compared to spectroscopy cell data. Figure 4-12 shows the measured average signal ratio from *Configuration*  $T_{BP320/BP292}$  (red circles) as a function of various ambient temperatures measured by thermocouples. The calculated average LIF-ratios show good agreement with cell data except at 800 K where the measurement uncertainty is the highest due to low signal-to-noise ratio.

To determine the measurement accuracy, LIF thermometry measurements should be compared to the jet temperature. However, as already mentioned, the real value of the jet temperature is unknown. A preliminary estimation of the accuracy of temperature measurements is performed here based on a simplifying hypothesis that the jet temperature is equal to that of the ambient temperature obtained by thermocouples. This initial assumption permits a first quantification of the temperature measurement accuracy by directly comparing LIF thermometry results to thermocouple temperature measurements.

To transform LIF-ratio images into meaningful temperature fields, a calibration curve is calculated by convoluting the detection filters BP292 and BP320 with  $p$ -DFB spectrum at various temperatures. The result is a “convoluted area” which represents the absolute LIF-signal collected by each filter. When these ratios are plotted against their corresponding ambient temperatures, the result is the calibration data shown in Figure 4-13. Note that the temperatures indicated in Figure 4-13 are based on thermocouple measurements carried out in the spectroscopy cell. The equation described in Eq. (4-8) corresponds to the logarithmic fit (red curve in Figure 4-16) relating temperature  $T$  (in Kelvin) to the LIF-signal ratio  $R$ .

$$T/K = 610 \ln(R) + 1110 \quad (4-8)$$

Figure 4-14 shows the average temperature fields derived from instantaneous 15 LIF-

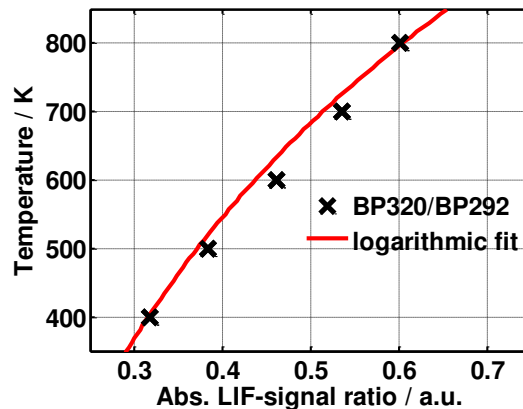


Figure 4-13: Dependence of the  $p$ -DFB signal ratio on temperature for two-color LIF thermometry for 266 nm excitation and filter pair BP320/BP292 obtained from LIF spectra in  $N_2$  by taking into account the spectral response of the entire detection system. The temperature values noted on the  $y$ -axis were obtained from thermocouple measurements performed in the optical cell close to the probe volume of the optical measurements.

ratio images of ECN Spray G at its conditions and variants by applying Eq. (4-8). From these images the mean over the entire jet was calculated and compared to thermocouple measurements. At  $3.5 \text{ kg/m}^3$  and 573 K, the mean temperature across the jet was found

to be centered at  $\sim 579$  K. This means that two-color LIF thermometry is slightly overestimating the jet temperature since we can expect the latter to be lower than the ambient. By calculating the mean temperature across the entire jet for other operating conditions and comparing it to ambient temperature (i.e., measured by a thermocouples), the LIF thermometry measurements once again overestimate the temperature of the jet by 1, 4, and 6% for 3.5, 6, and 9 kg/m<sup>3</sup> (573, 700, and 800 K), respectively. This implies that the accuracy of temperature measurements decreases with increasing ambient temperature.

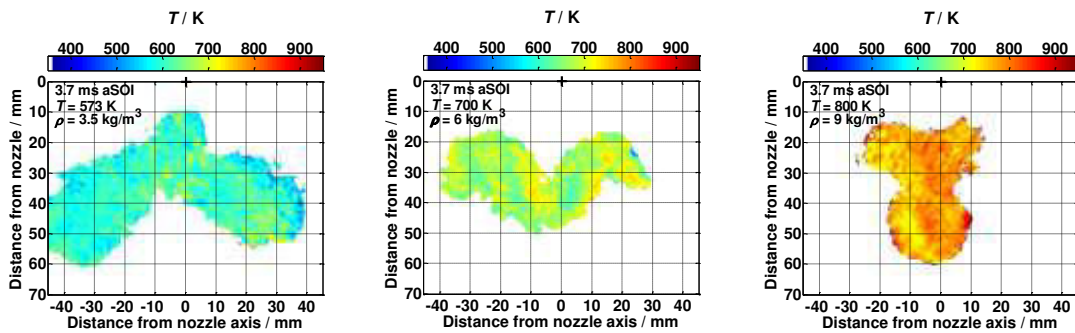


Figure 4-14: Temperature fields obtained by two-color  $p$ -DFB LIF with the Spray G injector at Spray G conditions and variants at 3.7 ms aSOI for *iso*-octane. The cross in the images represents the nozzle position. The experimental ambient conditions are noted on the top left side of the images.

To assess temperature fluctuations across the jet, the measurement precision needs to be determined. A more detailed discussion regarding temperature gradients in the jet will be discussed in section 4.3.2.

#### *Temperature and preferential evaporation measurements accuracy in the multi-component fuel configuration*

The accuracy was investigated for both pairs of detection channels used for visualizing preferential evaporation and temperature. By placing identical filters on each side of the image doubler, *Configuration I*<sub>[BP292/BP292]</sub> can then be used to determine the accuracy of preferential evaporation measurements by calculating the mean of the LIF-ratio average image [BP292/BP292]. Figure 4-15 shows LIF-ratio average image obtained by *Configuration I*<sub>[BP292/BP292]</sub>. The ratio across the jet is centered at unity expect for the spray boundary where ratios higher than unity are detected. The mean of the average LIF-ratio image of the jet was calculated and found to be 1.06. Therefore the relative error between the ideal case (unity) and the real mean of the superposed average image is  $\sim 6\%$ .

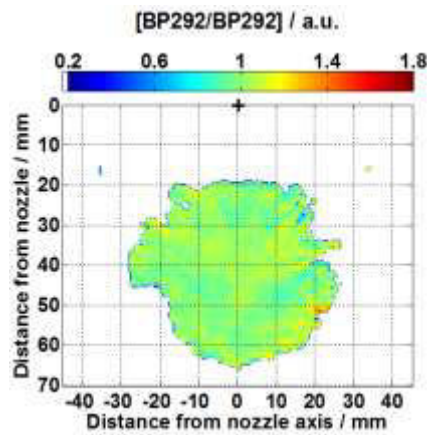


Figure 4-15: Two-tracer LIF-ratio average image taken in *Configuration*  $I_{[BP292/BP292]}$ . The average image was obtained from 15 instantaneous images. The cross in the images represents the nozzle position.

The methodology used to determine the temperature accuracy for single-component experiments was also applied to *Configuration*  $T_{BP377/[BP340]}$  to assess the temperature accuracy of the setup used for multi-component fuel experiments. Since 1-MN was selected for LIF-thermometry measurements, the LIF-ratio values obtained from jet images were compared to 1-MN calibration curve acquired from the spectroscopy cell data. This was done for Spray G and piezo-electric injector measurements. Once again, this analysis is performed as a preliminary step using the simplifying hypothesis ( $T_{jet} = T_{thermocouple}$ ).

The left panel of Figure 4-16 shows the two-color LIF-ratio calculated from average ECN Spray G images (red circles) and the calibration data obtained from the spectroscopy cell (blue squares) as function of core ambient temperature measured by thermocouples. LIF thermometry data portrays a good agreement with cell data. Similar to single-component measurement, the measurement error is relatively high at 800 K compared to 573 and 700 K due to low signal-to-noise ratio at high temperature and high pressure conditions (i.e., 800 K and 21 bar). The same conclusion applies to the right panel of Figure 4-16 which shows the two-color LIF-ratio calculated from average piezo jet images (red circles) and the calibration data obtained from the spectroscopy cell (blue squares) as a function of core ambient temperature measured by thermocouples. Note that these data points were performed at constant density conditions (see section 4.1.3).

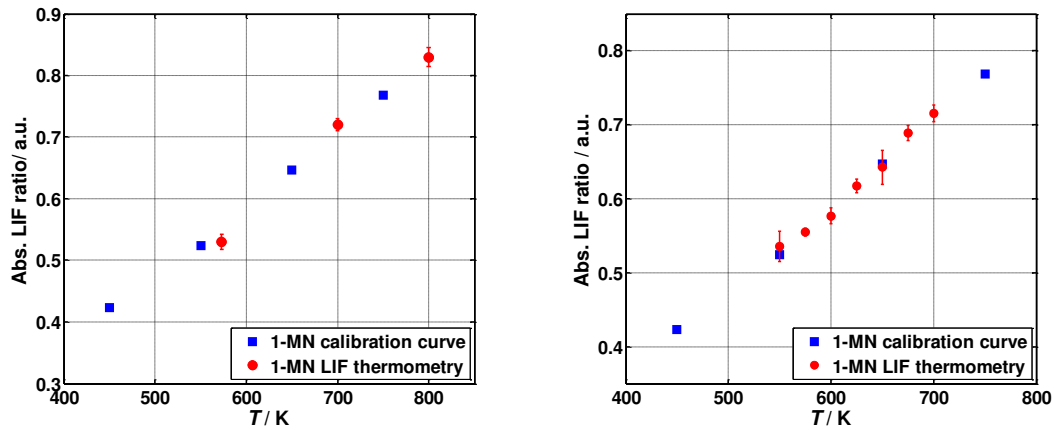


Figure 4-16: Measured average signal ratio from *Configuration*  $T_{BP377/[BP340]}$  (red circles) as a function of ambient temperature measured by thermocouples in comparison to spectroscopy cell data (blue squares) obtained by convoluting the BP340 and BP377 with 1-MN spectrum at various temperatures. LIF-signal ratio was calculated from spray images performed with Spray G (left) and the piezo-electric injector (right). Error bars represent the measurement uncertainty [74].

The accuracy was determined by calculating the difference between LIF thermometry and the thermocouple measurements for Spray G and piezo-injector experiments. The two-color LIF-ratio images were transformed into LIF temperature fields using the calibration curve of 1-MN which was derived from spectroscopy cell measurements. The procedure described for deriving  $p$ -DFB calibration curve was applied for 1-MN. The 1-MN temperature calibration curve described by in Eq.(4-9) corresponds to the logarithmic fit (red curve in Figure 4-17) relating temperature  $T$  to the LIF-signal ratio  $R$ .

$$T/K = 530 \ln(R) + 900 \quad (4-9)$$

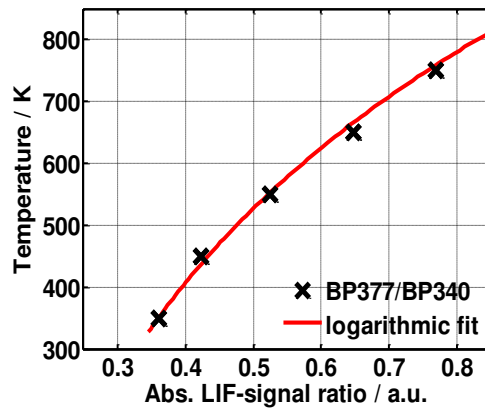


Figure 4-17: Dependence of the 1-MN signal ratio on temperature for two-color LIF thermometry for 266 nm excitation and filter pair BP377/[BP340] obtained from LIF spectra in  $N_2$  by taking into account the spectral response of the entire detection system. The temperature values noted on the y-axis were obtained from thermocouple measurements.

To quantify for the accuracy of temperature measurements performed in the multi-component fuel configuration, average temperature fields obtained from *Configuration*  $T_{BP377/[BP340]}$  were investigated. Figure 4-18 shows average two-color LIF temperature fields of ECN Spray G at its conditions and variants. The mean temperature calculated by considering the entire jet was found to be 590, 735, and 864 K. Once again, when comparing LIF thermometry findings to thermocouple measurements, the two-color LIF thermometry measurements over predicted the jet temperature by 3, 5, and 8% for 3.5, 6 and 9  $kg/m^3$  (at 573, 700, and 800 K) respectively. The multi-component fuel configuration has a lower accuracy than the single-component fuel configuration. The reason for this reduced accuracy is probably due to the fact that images originating from the image doubler suffer from a significant vignetting effect. Pixel-to-pixel sensitivity and flat-field correction could not fully correct for the non-uniform distribution of light projected on the image doubler. These effects render image mapping more challenging thus reducing accuracy.

The two-color LIF-ratio images of the piezo-injector were also converted into temperature fields using the 1-MN calibration curve. Figure 4-19 shows average two-color LIF temperature fields of jets originating from the piezo-electric injector at 5.2  $kg/m^3$  and for temperatures ranging between 550–700 K. The relative errors determined from piezo-injector measurements are similar to those of Spray G except at 550 K (5.2  $kg/m^3$ ) where the relative error is a mere ~1% (i.e., 556 K mean temperature obtained via two-color LIF compared to 550 K ambient temperature) against 3% for Spray G at 573 K (3.5  $kg/m^3$ ).

This is probably due to the fact that at high ambient densities the jet becomes more concentrated at the central portion of the CCD where the vignetting effect is less pronounced than what was observed with ECN Spray G at  $3.5 \text{ kg/m}^3$  and  $573 \text{ K}$  as the jet was spread over a wider portion of the sensor.

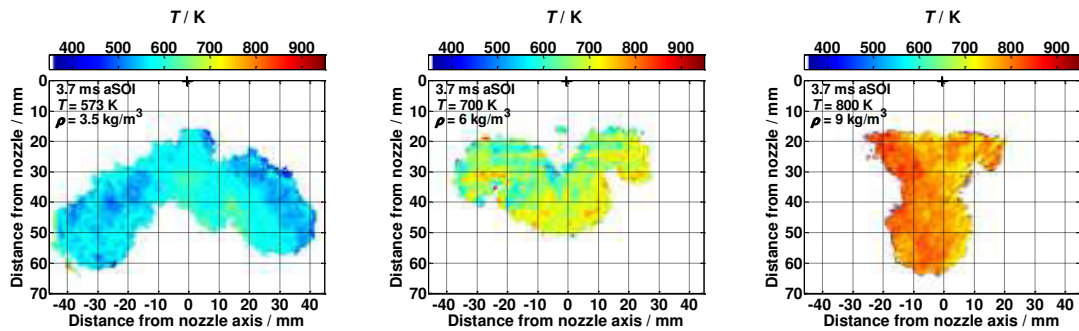


Figure 4-18: Average temperature fields obtained by two-color 1-MN LIF with the Spray G injector and at Spray G conditions and variants.

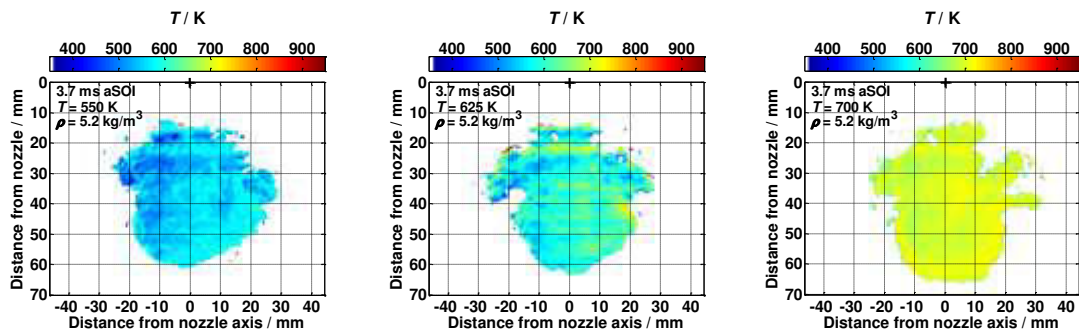


Figure 4-19: Average temperature fields obtained by two-color 1-MN LIF with the piezo-electric injector at a constant density of  $5.2 \text{ kg/m}^3$  for various ambient temperatures.

#### 4.3.1.2 Determining precision

The precision is mainly affected by the following error sources: (1) mismatch in image mapping, (2) pixel-to-pixel sensitivity variations of the two cameras and (3) shot noise. To quantify precision, a method based on comparing images obtained by identical filters under similar conditions to those of two-tracer (i.e., preferential evaporation) and two-color (i.e., temperature) LIF was adopted.

Ideally, when two images obtained with identical filters are superimposed, their resulting ratio should be unity and thus the pixel-wise correlation between both nominally identical images should result in a straight line with a slope equal to unity. In reality the LIF-ratio

suffers from some dispersion (i.e.,  $\sigma_R$ ) due to the contribution of different error sources. The deviation from the ideal correlation can therefore be used to determine the influence of error sources, assuming that their contribution is unchanged when changing filters. The precision of the preferential evaporation experiments is calculated from the two-color LIF-ratio standard deviation image acquired by *Configuration I*<sub>[BP292/BP292]</sub>. The same procedure is applied to *Configuration I*<sub>[BP292/BP292]</sub> to determine the precision of the temperature measurements. The dispersions are firstly calculated in terms of LIF-ratio and then converted to temperature ( $\sigma_T$ ) using the adequate tracer calibration curve derived from spectroscopy cell measurements. Since two different experimental setups were used for single- and multi-component fuels, the temperature measurement precision of each setup was assessed separately.

#### *Single-component fuel configuration*

The temperature precision generated by the optical detection path of *Configuration I*<sub>[BP292/BP292]</sub> was determined by a two-step procedure. Firstly, the image mapping was optimized by recording LIF jet images using identical filters under conditions similar to the two-color *p*-DFB measurements. Then, a flat-field correction was carried out to correct for variations in pixel-to-pixel sensitivity using a set of flat-field images.

Figure 4-20 shows correlation plots of an image pair obtained by *Configuration I*<sub>[BP292/BP292]</sub> that underwent these different steps. The absolute signal intensities of pixels of the base and input images are plotted on the *x*- and *y*-axis respectively. The grey dashed line corresponds to the mean of the spray ratio image (BP292/BP292) image while  $\sigma_R$  represents the relative dispersion around the mean. Note that the reported dispersions are determined from calculating the standard deviation over the entire image. Figure 4-20a shows the correlation plot after standard mapping using a reference grid. The plot suffers from a significant scattering ( $\sigma_R \sim 0.13$ ) around the mean (grey dashed line) due to imperfect image registration and pixel-to-pixel sensitivity. Figure 4-20b shows the correlation after applying the optimized image mapping and pixel-to-pixel sensitivity resulting in a 63% decrease in the dispersion. Figure 4-20c shows the correlation plot after an additional pixel-to-pixel sensitivity correction based on a flat-field image. An additional reduction of the dispersion by 25% is observed. The remaining dispersion is attributed to shot noise and imperfect corrections of the previous effects. This contribution was used to assess the measurement precision which for *Configuration I*<sub>[BP292/BP292]</sub> was found to be  $\pm 0.045 (\pm 1\sigma_R)$ .

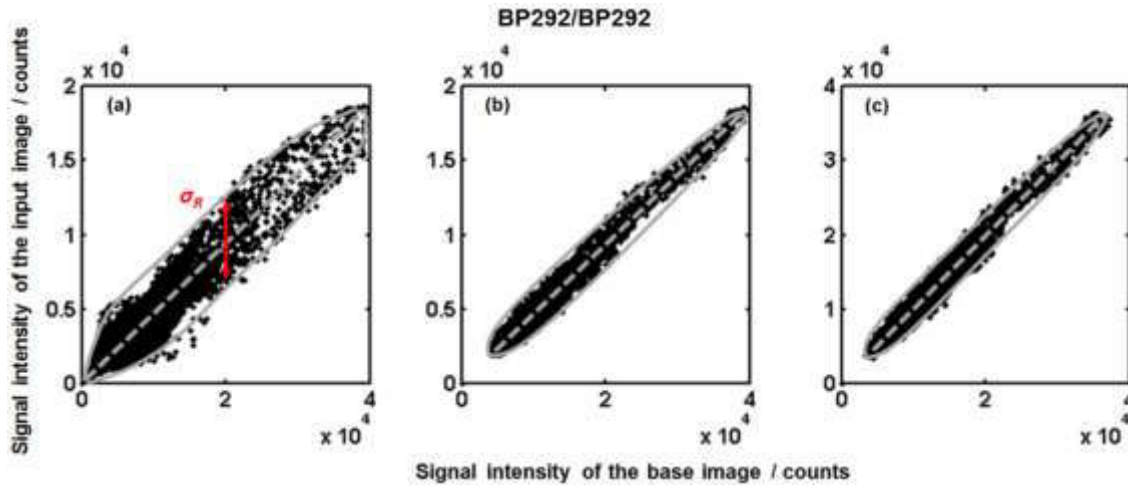


Figure 4-20: Signal intensity correlation for an image pair obtained by *Configuration I<sub>BP292/BP292</sub>* (a) after image mapping using a reference grid image, (b) after optimizing of the spatial adjustment according to [58], and (c) after additional flat-field correction.

The LIF-ratio representing the measurement precision is then transformed to temperature precision by solving for the first derivative of the temperature calibration curve of *p*-DFB expressed in Eq.(4-8). The derivative of Eq. (4-8), results in:

$$\sigma_T = 610 \frac{\sigma_R}{R} \quad (4-10)$$

where  $\sigma_T$  is the temperature measurement precision and  $\sigma_R$  is the standard deviation of the values  $R$  in the ratio image obtained in *Configuration I<sub>BP292/BP292</sub>*. The temperature precision in *Configuration I<sub>BP292/BP292</sub>* was found to be  $\pm 25$  K.

#### *Multi-component fuel configuration*

The measurement precision was calculated for detection channels used to visualize preferential evaporation and temperature distribution in the spray. Therefore, LIF-ratio images of *Configuration I<sub>[BP292/BP292]</sub>* and *Configuration I<sub>BP292/[BP292]</sub>* were examined. The steps described above for single-component fuel experiments for optimizing image registration and correcting for pixel-to-pixel sensitivity were also applied on images obtained from multi-component experiments. The correlation plots shown in Figure 4-21 represent the signal intensity correlation for an image pair obtained by *Configuration I<sub>[BP292/BP292]</sub>* and *Configuration I<sub>BP292/[BP292]</sub>* after optimizing image registration and after applying flat-field correction. The measurement precision of *Configuration I<sub>[BP292/BP292]</sub>* was found to be  $\pm 0.05$  while that of *Configuration I<sub>BP292/[BP292]</sub>* was found to be  $\pm 0.055$  ( $\pm 1\sigma_R$ ).

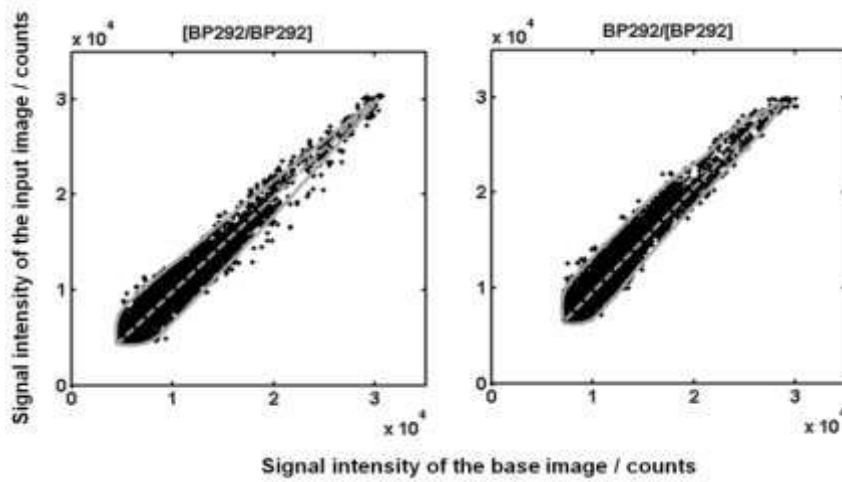


Figure 4-21: Signal intensity correlation for an image pair obtained by *Configuration*  $I_{[BP292/BP292]}$  (left) and *Configuration*  $I_{BP292[BP292]}$  (right) after applying image registration and flat-field correction.

The temperature measurement precision was derived from precision calculations of *Configuration*  $I_{BP292[BP292]}$  since the same pair of detection channels coupled with different pair of optical filters (BP377/[BP340]) was used to calculate the temperature distribution in the vaporized spray. The dispersion of the LIF-ratio can be expressed in terms of dispersion in temperature by solving for the first derivative of the temperature calibration Eq. (4-9) as illustrated Eq. (4-11).

$$\sigma_T = 530 \frac{\sigma_R}{R} \quad (4-11)$$

The calculated temperature precision of *Configuration*  $I_{BP292[BP292]}$  is  $\pm 28$  K. The multi-component fuel *Configuration*  $I_{BP292[BP292]}$  has a lower precision than the single-component fuel *Configuration*  $I_{BP292/BP292}$  probably because images originating from the image doubler suffer from vignetting. Pixel-to-pixel sensitivity and flat-field correction could not fully correct for the non-uniform distribution of light projected on the detector. These effects render image registration more challenging thus resulting in high fluctuations in the LIF-ratio spray image obtained by *Configuration*  $I_{BP292[BP292]}$ .

### 4.3.2 Spatially-resolved fuel concentration maps and their corresponding temperature fields

In the previous sections, the measurement precision was determined for the two-image setup (single-component fuel) and three-image setup (multi-component fuel). A first es-

timation of the temperature measurement accuracy was also provided based on a simplifying hypothesis (jet temperature is equal to the ambient temperature measured by thermocouples). In this section, fuel concentration and temperature maps based on an adiabatic mixing model will be presented and used to determine more precisely the temperature measurement accuracy. The method used to derive fuel concentration maps and its hypotheses are discussed in section 4.2.1. The following section discusses the underlying hypothesis and assesses accuracy.

#### **4.3.2.1 Discussion of the hypotheses and the accuracy of the method**

Hypothesis (1) presented in section 4.2.1 assumes that the LIF intensity is proportional fuel to concentration and to incident laser energy. This hypothesis neglects the impact of temperature on fluorescence quantum yield and thus on the absolute LIF-signal intensity. In order to assess the validity of this hypothesis, the temperature field obtained from an adiabatic mixing model was used to evaluate the effect of temperature variation in the jet on the fluorescence quantum yield. The details of this analysis will be presented in section 4.3.2.2, where it will be shown that temperature gradients in the jet for the investigated operating condition have a negligible effect on fluorescence quantum yields which makes hypothesis (1) valid.

Hypothesis (2) (axisymmetric jet), related to Eq. (4-2), may generate significant uncertainties in the present configuration since the spray is issued from eight discrete holes and significant shot-to-shot fluctuations in the mixing process happen due to turbulent processes. The fuel concentration images, displayed in the next section, show that some degree of asymmetry do exist between the two plumes that are observed in the visualization plan. In order to minimize this effect, the  $I_v$  for each plume was calculated separately and then summed to result in  $I_v$ , representative of the LIF-signal volume of the whole spray. The instantaneous images were corrected for shot-to-shot fluctuation by normalizing by the mean laser energy ratio. Once instantaneous images are normalized, the average image is calculated and the normalization method is applied on this average image to minimize asymmetry effects. To assess the measurement error induced by the asymmetry of the jet, additional measurements were carried out with the light sheet perpendicular to the spray axis located at 38 mm from the injector nozzle with the camera positioned at a 90° angle thus collecting the fluorescence from the bottom window. Figure 4-22 shows the corresponding image of the LIF distribution in the perpendicular plane for Spray G target conditions and variants at 3.7 ms aSOI. These images show that alt-

though the jet is issued from eight discrete holes, the fuel concentration is relatively homogeneously distributed in the azimuthal direction at image timing (3.7 ms aSOI). This means that the long duration between end of injection and imaging provided sufficient mixing time to drastically reduce mixture inhomogeneities.

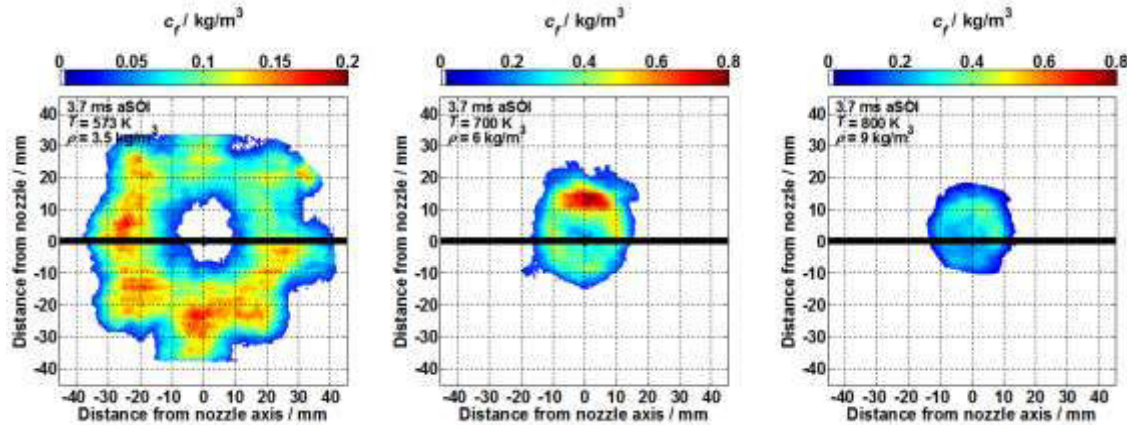


Figure 4-22: Average fuel concentration fields in a perpendicular plan located at 38mm of the nozzle for Spray G target conditions and variants at 3.7 aSOI. Each image is obtained from 15 instantaneous LIF images. The marked rectangular zone indicates the area used for reconstructing 2D information from 1D information.

In addition, the images in Figure 4-22 were analyzed to determine the error generated by the axisymmetric hypothesis 2D global information. For this purpose, 1D information corresponding to the intersection between the two perpendicular light-sheet was obtained with the same reconstruction methodology that was used in Eq.(4-2). The resulting volume intensity was then compared to the 2D information obtained from direct integration of the images in Figure 4-23. For  $3.5 \text{ kg/m}^3$ , a difference of 15% was obtained between the two methods. Since this difference is related to the asymmetry of the jet, the error of hypothesis (2) is estimated at 15%. As for ambient densities 6 and  $9 \text{ kg/m}^3$ , the error is estimated at 17% and 11%, respectively.

Hypothesis (3), related to Eq.(4-3), assumes that the entire width of the spray is captured by the light-sheet. However, the light-sheet was 5.2 mm from the nozzle and therefore did not cover the entire jet region. Moreover, applying a threshold of 10% leads to an additional reduction of the visualization region corresponding to an additional reduction of 2.5 mm from the light-sheet (i.e., spray visualization starts from 7.7 mm downstream of the nozzle). Therefore a part of the jet is not seen in the LIF images. Consequently,  $I_v$  does not account for the total injected fuel mass  $m_{\text{fuel}}$ , which is a source of uncertainty

in Eq.(4-3). To assess the impact of this “uncaptured mass” on the calculation, the schlieren images were used to calculate the ratio between the “uncaptured volume” and the total volume of the jet. For spray G target conditions, the ratio was calculated for 2.7 and 3.7 ms aSOI. The ratio was found to be below 1%. This error source was therefore neglected and the total fuel mass injected  $m_{\text{fuel}}$  (i.e., 10 mg) was used in Eq. (4-3).

Additional sources of uncertainty exist due to the post-processing method. The first one is related to the threshold applied to raw images to reduce noise. The impact of the threshold factor applied in image post-processing is investigated by varying the threshold factor was by  $\pm 5\%$ . The variations in the threshold factor resulted in a change of less than 4% in the calculated  $I_v$ . The third source that contributes to the method uncertainty is the choice of the nozzle coordinates. The nozzle abscissa was varied by  $\pm 3$  pixels. The impact of this abscissa variation resulted in a change of less than 2% in the calculated  $I_v$ .

Taking into account all these uncertainty sources, it is considered that the accuracy of the normalization method is of the order of 22%.

#### **4.3.2.2 Fuel concentration maps and their corresponding temperature fields**

In this section the fuel concentration maps and their corresponding temperature fields obtained by the adiabatic mixing model are presented for single- and multi-component fuel experiments. Moreover, two-color temperature fields are calculated from LIF-ratio images by applying the temperature curves obtained via the spectroscopy cell. The objective is to refine the determination of the temperature measurement accuracy by comparing the LIF thermometry results to temperature information from the adiabatic mixing model. The latter uses thermocouple measurements of the vessel core temperature as input and takes into account the effect of evaporation and mixing.

### **Spray G injector**

#### *Single-component fuel experiments*

Fuel concentration fields of ECN Spray G were derived from images acquired with a BP292 which collects the fluorescence signal originating from the peak of the *p*-DFB spectrum. Measurements were carried out for Spray G conditions ( $3.5 \text{ kg/m}^3$  at 573 K) and variants ( $6$  and  $9 \text{ kg/m}^3$  at 700 and 800 K respectively). These conditions were investigated at different aSOI timings where the spray is fully vaporized. Figure 4-23 shows that at  $3.5 \text{ kg/m}^3$  the fuel mass distribution is quasi-homogenous, with averaged values of  $0.15$  and  $0.18 \text{ kg/m}^3$  at 2.7 and 3.2 ms aSOI respectively. At 3.7 ms aSOI, the fuel

mass distribution becomes even more homogenous. At  $6 \text{ kg/m}^3$ , the jet structure changes drastically. While the vapor plumes were globally aligned with the nozzle axis at  $3.5 \text{ kg/m}^3$ , forming an inversed V-shape, the higher penetration is now aligned with the injector axis, forming a central plume, with two wings remaining on the sides where the plume formed during injection were located, altogether forming an M-shape. At  $9 \text{ kg/m}^3$ , this transformation of the jet structure is even more pronounced.

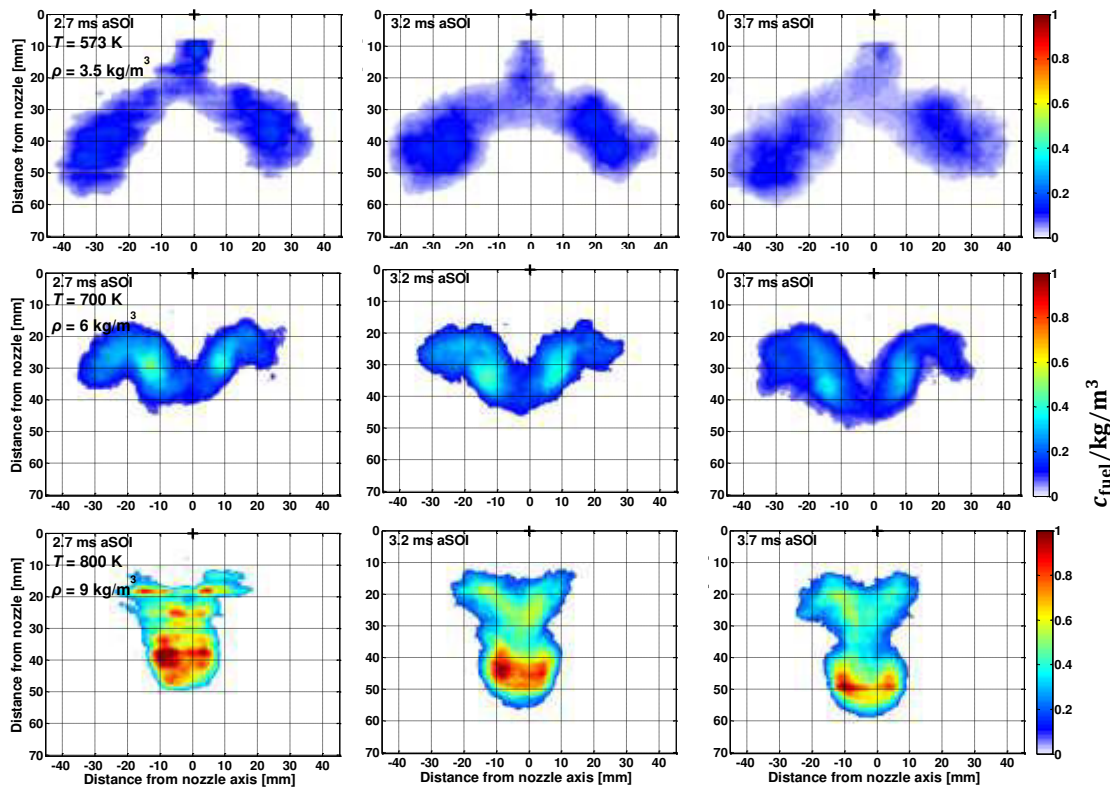


Figure 4-23: Fuel concentration fields at Spray G target conditions and at other parametric variations for various aSOI timings. The experimental conditions are given in the first image of each row. Each image is obtained from 15 instantaneous LIF image.

The jet at this condition mainly consists of a central plume aligned with the injector axis, while small wings are visible on the upper sides. This change in structure also generates higher fuel mass concentration gradients since the jet is more concentrated in the central plume.

Fuel concentration fields obtained at 3.7 ms aSOI were then used to derive the temperature fields across the spray by applying the adiabatic mixing model developed by Epsley et al. [72]. Initially, temperature was computed directly from spatially-resolved fuel-air ratio fields that were calculated from fuel mass concentration fields assuming constant

fluorescence quantum yield  $\Phi_{fl}$ . This results in zeroth-order temperature fields where the dependence on  $\Phi_{fl}$  is neglected. The left panel in Figure 4-24 shows spectrum of *p*-DFB for various ambient temperatures normalized at 400 K. These data are a courtesy of CORIA laboratory where these measurements were performed [75].

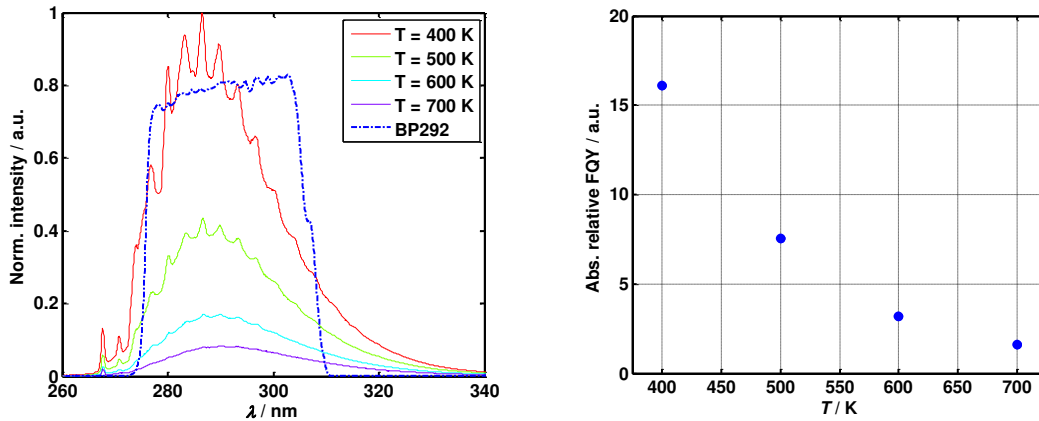


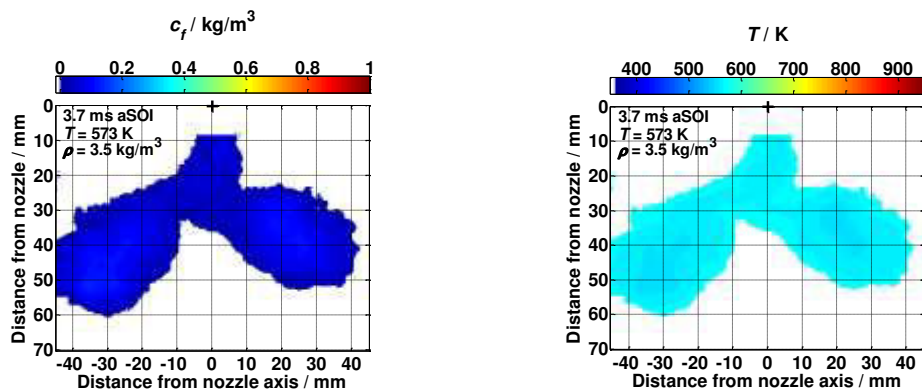
Figure 4-24: Absolute fluorescence spectrum of *p*-DFB for different bath gas temperatures at 1 bar in pure N<sub>2</sub> (left), courtesy of CORIA laboratory, and the absolute relative quantum yield of *p*-DFB as a function of temperature measured by thermocouples (right). Values were obtained by, firstly, convoluting the transmission curve of BP292 with the fluorescence spectrum of *p*-DFB.

To calculate the temperature dependence of  $\Phi_{fl}$ , the “convolution area” of optical filter BP292 and each spectrum is calculated and plotted in the right panel of Figure 4-24.  $\Phi_{fl}$  function is then applied on the uncorrected temperature field resulting in a relative fluorescence quantum yield map. The map is then normalized by the maximum  $\Phi_{fl}$ . The first-order fuel concentration maps are then obtained by dividing the zeroth-order fuel concentration by the normalized  $\Phi_{fl}$  map thus accounting for the temperature influence on fuel concentration. Lastly, the temperature distribution is recalculated from the first-order fuel concentration maps thus resulting in first-order temperature fields.

Figure 4-25 shows first-order approximation (i.e., corrected for variations in  $\Phi_{fl}$ ) fuel mass concentration fields and their corresponding temperature fields obtained by applying the adiabatic mixing model. Average temperature and its fluctuations were calculated over the whole jet area of the two-dimensional image. For 3.5 kg/m<sup>3</sup>, the temperature distribution was found to be homogenous ( $\pm 4$  K) across jet with temperature ranging between 563 $\pm 4$  K. At 6 kg/m<sup>3</sup>, temperature gradients start to appear especially in the jet core where vapor plumes merge to form a region characterized by having a relatively

high fuel mass concentration compared to the jet periphery. The average jet temperature was computed  $679 \pm 10$  K. The highest temperature gradients were found at  $9 \text{ kg/m}^3$  where the core temperature of the jet dropped to  $\sim 750$  K while the spray periphery temperature ( $\sim 780$  K) stayed relatively close to the ambient temperature (800 K). Regardless of this variation between core temperature and periphery temperature of the spray, the average temperature and the fluctuation calculated across the entire spray were found to be  $760 \pm 19$  K.

To assess the influence of the  $\Phi_{fl}$  on temperature calculation, the absolute and the relative difference in temperature resulting from the zeroth-order and first-order approximation of temperature fields were examined. Figure 4-26 shows the absolute (left panel) and the relative (right panel) temperature difference resulting from correcting for variation in  $\Phi_{fl}$  for ECN Spray G conditions and variants. For  $3.5 \text{ kg/m}^3$ , the absolute  $\Delta T$  does not exceed 1.25 K throughout the spray (i.e., relative variation of temperature  $\sim 1\%$ ) signifying a negligible impact of  $\Phi_{fl}$  on temperature calculation. For  $6 \text{ kg/m}^3$ , the absolute  $\Delta T$  increases at the periphery of the spray and in the areas surrounding the high fuel concentration regions. This increase, however, is still considered negligible since the resulting relative temperature difference across the whole spray is below 2%. Same conclusion applies to  $9 \text{ kg/m}^3$  as the absolute  $\Delta T$  increases to 16 K in the region surrounding the core of the jet where the absolute  $\Delta T \sim 7$  K. For all three Spray G conditions and variants that were investigated, the variation of  $\Phi_{fl}$  with temperature had negligible impact on the temperature fields since relative variations in  $\Delta T$  did not exceed 2% even at high-density conditions. Moreover, since  $\Phi_{fl}$  decreases with temperature, the zeroth-order approximation of fuel concentration was thus underestimated leading to an overestimation of jet temperature. After correcting for  $\Phi_{fl}$ , the first-order consequently leading to a first-order temperature approximation higher than that of the zeroth-order approximation.



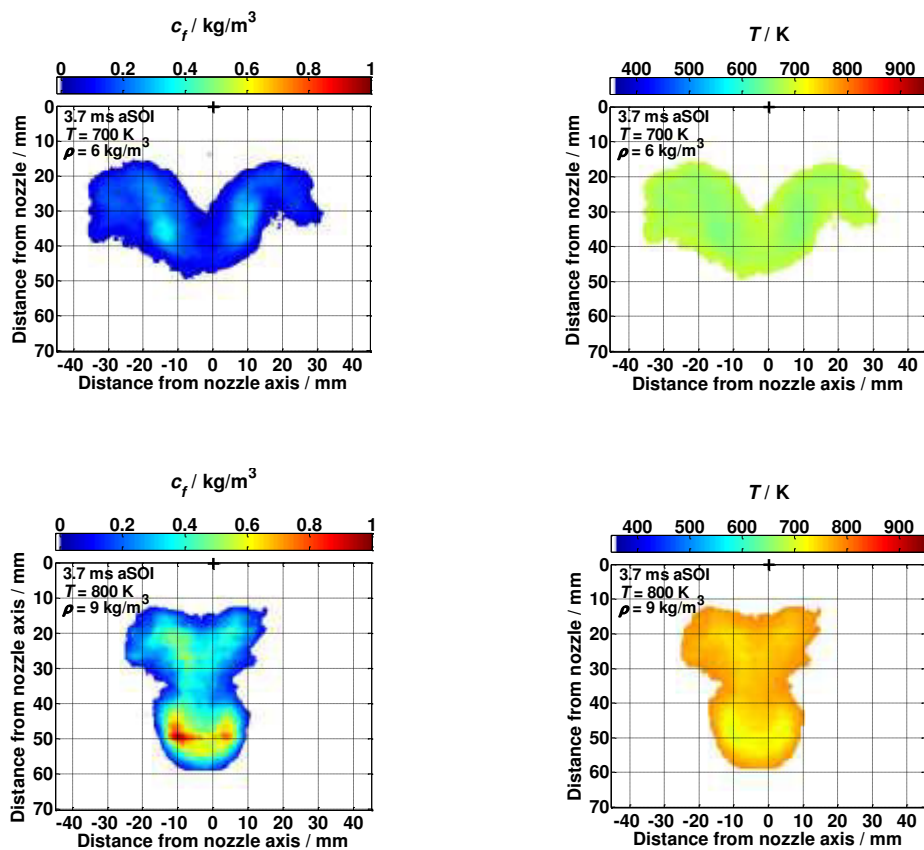
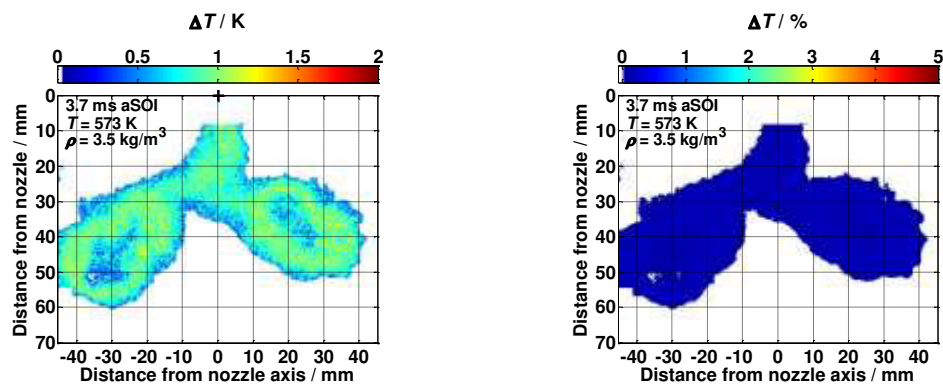


Figure 4-25: Fuel concentration fields (left) and their corresponding temperature fields (right) at Spray G conditions and variants at 3.7 ms aSOI. These experiments were performed with *iso*-octane as a surrogate fuel. The fuel concentration fields were calculated from images acquired by BP292 and then transformed to temperature fields by applying the adiabatic mixing model.



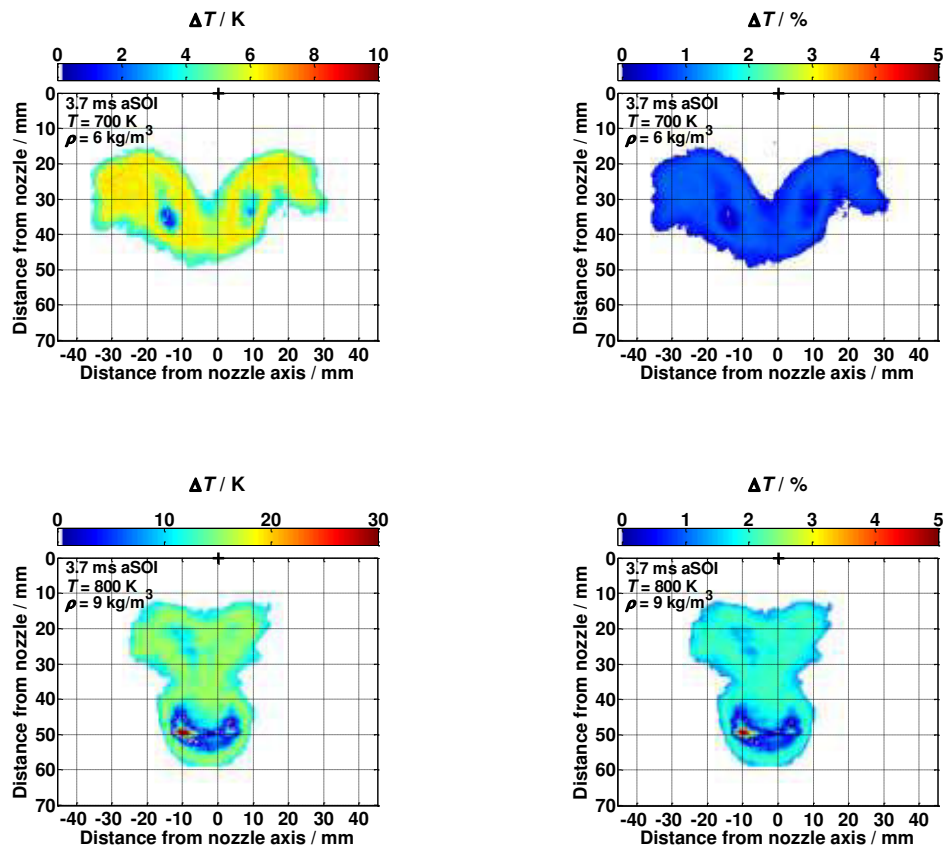


Figure 4-26: Absolute (left) and relative (right) temperature difference calculated from the uncorrected and corrected temperature fields for Spray G conditions and variants.

After deriving the adiabatic mixing temperature fields from fuel concentration maps, the former were compared to two-color LIF temperature fields. Figure 4-27 shows the temperature fields derived from LIF-ratio images of Spray G and variants by applying Eq.(4-8) which is the  $\rho$ -DFB temperature calibration equation derived from spectroscopy cell data. The left panel of Figure 4-27 shows that the temperature distribution across the spray is homogeneous for 3.5 kg/m<sup>3</sup> since variations ( $\pm 28$  K) are within the measurement precision ( $\pm 25$  K). For 6 kg/m<sup>3</sup>, temperature gradients start to appear in the core region of the spray where temperature ( $\sim 650$  K) is lower than that of the spray periphery ( $> 700$  K). The variation over the entire spray was found to be  $\pm 32$  K. The same observation applies to temperature fields obtained at 9 kg/m<sup>3</sup> where fluctuations were found to be  $\pm 34$  K. The temperature gradients of two-color  $\rho$ -DFB temperature fields are similar to the gradients observed on temperature fields derived from the adiabatic model partic-

ularly in high fuel vapor concentration regions. This result shows that the LIF thermometry measurements were capable to correctly capture temperature gradients across the spray.

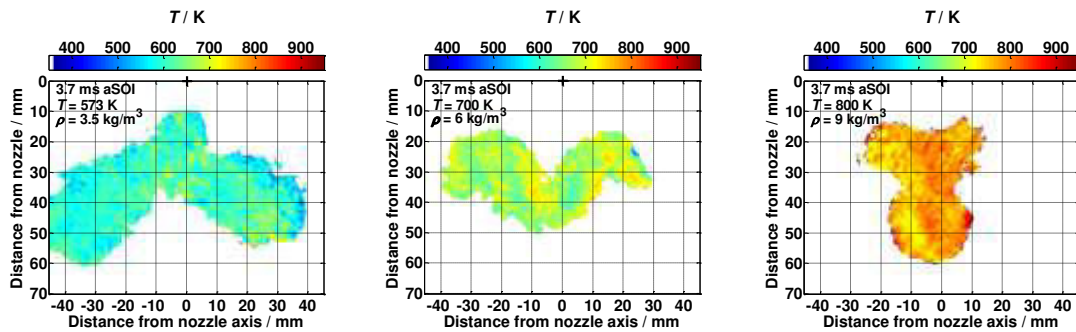
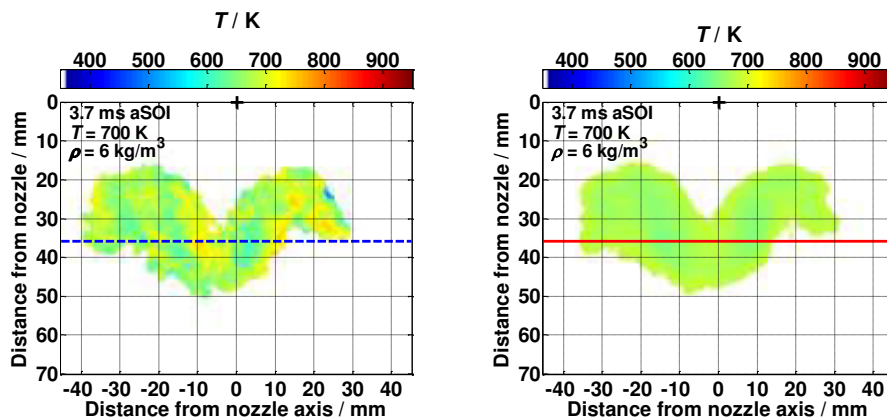


Figure 4-27: Temperature fields obtained by two-color  $p$ -DFB LIF with the Spray G injector and at Spray G conditions and variants at 3.7 ms aSOI for *iso*-octane. The cross in the images represents the nozzle position. The ambient conditions are given in the figure.

To further investigate the spray temperature obtained from the different measurement techniques, the temperature profiles at 38 mm away from the nozzle was plotted along with the ambient temperature measured by a thermocouple for 6 kg/m<sup>3</sup> as shown in Figure 4-28. The profiles at 38 mm away from nozzle are of interest because they display significant signal variations. The top panel of Figure 4-28 also shows temperature fields derived from absolute LIF-ratios (left panel) and fuel concentration fields. The profiles show that similar temperature gradients were captured by both LIF thermometry and adiabatic mixing technique. The LIF-ratio based results exceed the ambient core temperature in some areas. This can be due to imperfect image superposition and the improper correction of the differences in sensitivities of each camera (cf., section 4.3.1.1).



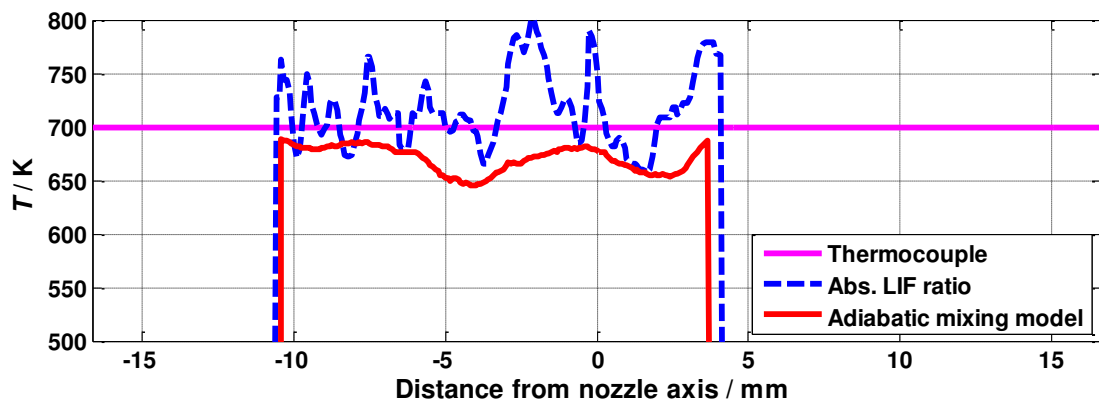


Figure 4-28: Temperature profile at a distance 38 mm from the nozzle for  $6 \text{ kg/m}^3$  at 700 K (magenta line) calculated from absolute two-color  $p$ -DFB LIF-ratio (blue dashed line and top left panel). The temperature profile representing the adiabatic mixing model (red line) was derived from the fuel concentration maps (top right panel).

Now that average adiabatic mixing temperature fields are available, a second and more refined determination of the accuracy can be carried out for the single-component fuel configuration by comparing mean temperatures of two-color LIF thermometry and adiabatic mixing temperature fields. In section 4.3.1, the LIF thermometry measurements of ECN Spray G compared the temperature values obtained by two-color LIF directly to the ambient vessel temperature acquired via thermocouples although the latter corresponds to the temperature outside of the jet. However, the temperature fields derived using the adiabatic mixing model use this ambient temperature as an input parameter while taking into account the mixing process in the jet since temperature calculations are derived from fuel concentration maps. Therefore, it is now possible to improve the comparison of the temperature obtained with the two methods by comparing the absolute two-color LIF thermometry to jet temperatures calculated from the adiabatic mixing temperature fields. Figure 4-29 presents the two methods used for determining the jet temperature. The calibration curve obtained from the spectral data (blue squares) is compared to the two-color LIF-ratios by two different approaches: (1) the measured average two-color LIF thermometry data is compared to ambient temperature determined by thermocouples (red circles). (2) The LIF data is compared to the average jet adiabatic mixing temperature (magenta circles). Results show that below 800 K, the two methods give similar results, and that the relative error between the LIF thermometry and the adiabatic mixing mode results corresponds to  $\sim 3\%$ . At 800 K, the deviation between the two methods start to be significant implying a decrease in measurement accuracy by  $\sim 7\%$ . Quantifying

measurement accuracy in such conditions remains intricate due to challenges in precisely identifying which of the two methods is more accurate in providing jet temperature estimation. However, there is a higher probability that the adiabatic mixing temperature is more accurate than that of thermocouple measurements since it accounts for evaporation and mixing.

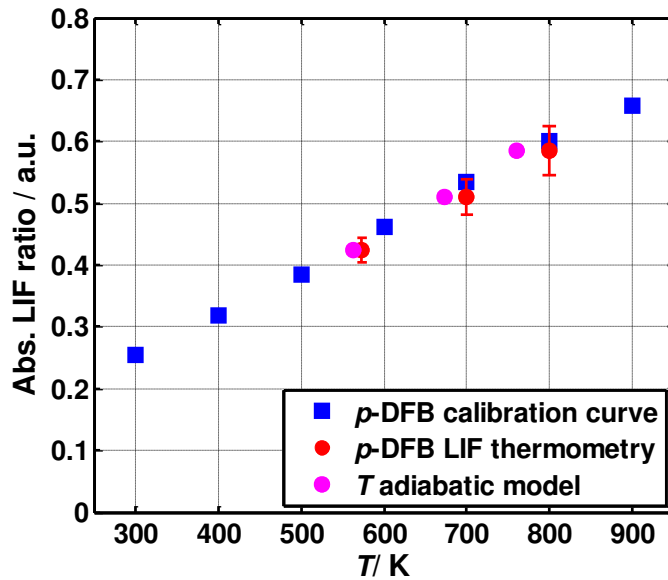


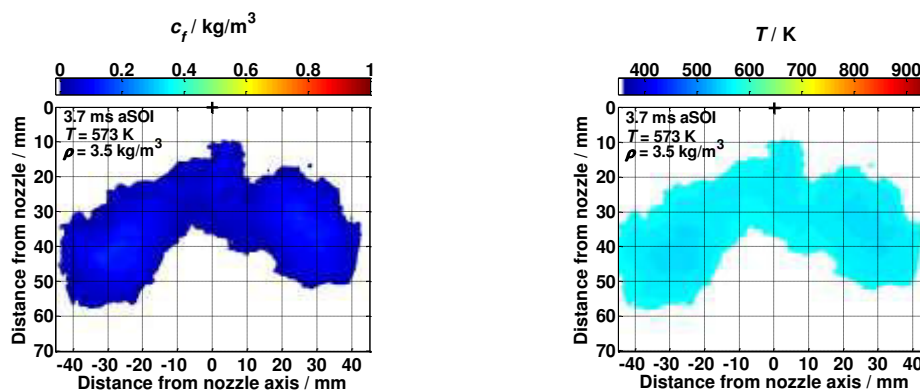
Figure 4-29: Measured BP320/BP292 signal ratio (red circles) as a function of ambient temperature in comparison to spectroscopy cell data (blue squares). The adiabatic mixing data (magenta circles) represent the absolute LIF-ratios attributed to average temperatures calculated from adiabatic mixing temperature fields. Error bars represent the measurement uncertainty [74].

In conclusion, the jet temperature was estimated by converting the fuel concentration fields to adiabatic mixing temperature fields and also by  $p$ -DFB two-color LIF thermometry. For the adiabatic mixing model, the ambient core temperature determined by thermocouples was used as an input parameter to calculate the temperature distribution in the jet. In this method, the evaporation and the mixing process were taken into account. For  $p$ -DFB two-color LIF, average ratio images were converted to temperature fields by using the calibration curve based on spectroscopy cell data. Therefore both approaches are capable of estimating the jet temperature and therefore the correct estimation probably lies somewhere between the temperatures determined via adiabatic mixing model and two-color LIF thermometry.

#### *Multi-component fuel experiments*

The change from single to multi-component fuel can affect the global jet mixture formation process because of the modification of the evaporation process. Before analyzing the effect of preferential evaporation, it is therefore important to understand if and how the multi-component fuel can affect the mixing process. However, investigating the mixture formation of multi-component fuels is more complex than that of single-component fuels because the definition of the fuel concentration becomes complicated when the mixture composition deviates from homogeneity due to preferential evaporation. In the present work, a simplified approach based on determining two fuel concentrations using the two collection channels corresponding to the two tracers was used. Therefore, each collection channel is analyzed separately to provide fuel concentration maps which are similar to the approach used for the single-component fuel. As it will be shown in this section, the differences in the results obtained with the two tracers are negligible compared to the measurement uncertainty implying that preferential evaporation has a second-order effect on the determination of the total fuel concentration. The fuel concentration can be therefore determined using only one of the two collection channels. This section firstly presents the results obtained with the 292-nm detection channel and then with 340-nm channel.

The left panel of Figure 4-30 displays the fuel mass concentration fields of Spray G at its conditions and variants for different aSOI timings, using the 292-nm channel. The overall jet shape and fuel distribution are similar to the ones observed and calculated from single-component fuel experiments. Like Spray G single-component fuel sprays, Spray G multi-component spray plumes start to merge at the nozzle axis as ambient



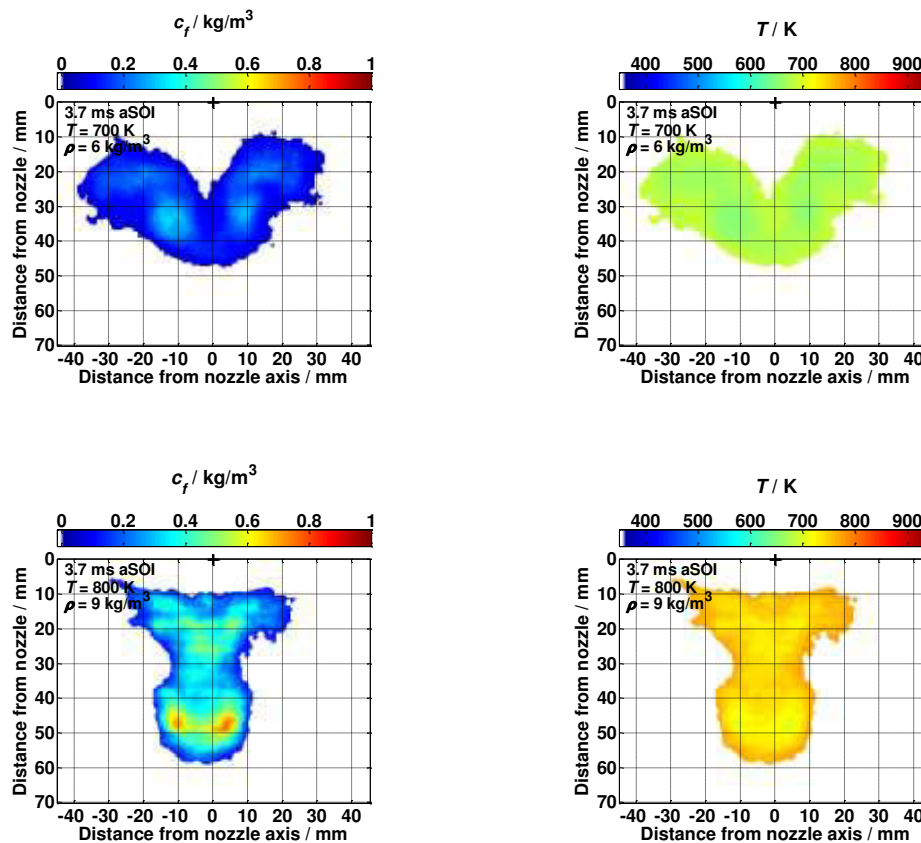


Figure 4-30: Fuel mass concentration fields (left) and their corresponding temperature fields (right) for an ECN Spray G injector at Spray G conditions and variants at 3.7 ms aSOI. These experiments were performed with the multi-component fuel. The fuel concentration fields were calculated from images acquired by BP292. The temperature distribution was derived from the fuel mass concentration field using an adiabatic mixing model.

density increases from 3.5 to 9 kg/m<sup>3</sup>. The fuel mass distribution was also found to be homogenous for low density conditions and became less so as ambient density increases. These findings show that for the investigated conditions, the shape of the fuel jet is independent of the type of surrogate fuel. By the same token, the fuel concentration fields derived from single- and multi-component fuel experiments show the same gradients which implies that the fuel concentration distribution of *iso*-octane is not affected by the presence of other fuel components (*n*-pentane and *n*-undecane).

Fuel concentration fields were used to calculate the temperature across the jet with the help of the adiabatic mixing model. The right panel of Figure 4-30 shows adiabatic mixing temperature fields for ECN Spray G injector at its conditions and variants. The average temperature values and their corresponding fluctuations agree well with values obtained from Spray G single-component fuel temperature fields (cf. Figure 4-25). Note that the

temperature fields are first-order estimations since the fuel concentration fields were corrected for variations in  $\Phi_{fl}$  with respect to temperature.

To analyze the temperature gradients of Spray G for single-component and multi-component fuel measurements, the horizontal temperature profiles were compared at 35 and 45 mm away from nozzle for 700 and 800 K respectively. These distances are of interest because they suffer from relatively high temperature gradients. Figure 4-31 shows that the derived temperature fields from fuel concentration fields of *iso*-octane and multi-component fuel agree in terms of absolute temperature. The two temperature fields (i.e., at 700 and 800 K) display a similar temperature fluctuation behavior (cf.,  $\pm 12$  cm and  $\pm 5$  mm from nozzle at 700 and 800 K, respectively).

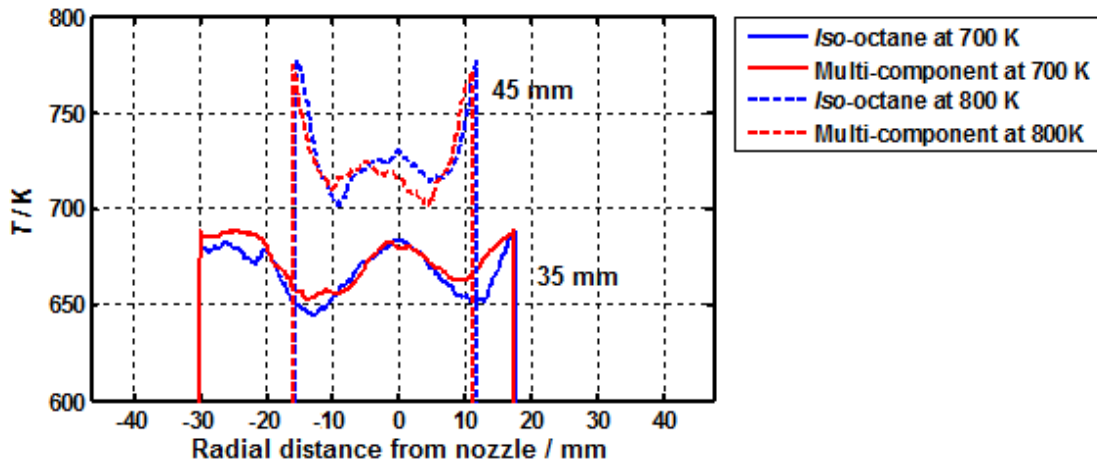


Figure 4-31: Temperature fields of Spray G derived from fuel mass concentration fields obtained at 6 and 9 kg/m<sup>3</sup> for 700 (solid line) and 800 K (dashed line) respectively. The values indicated on the figure represent the axial distance from the nozzle.

The same methodology was applied to the second 340-nm channel corresponding to the fluorescence signal emitted by 1-MN. Figure 4-32 shows the fuel mass concentration fields derived from BP340 images along with their corresponding adiabatic mixing

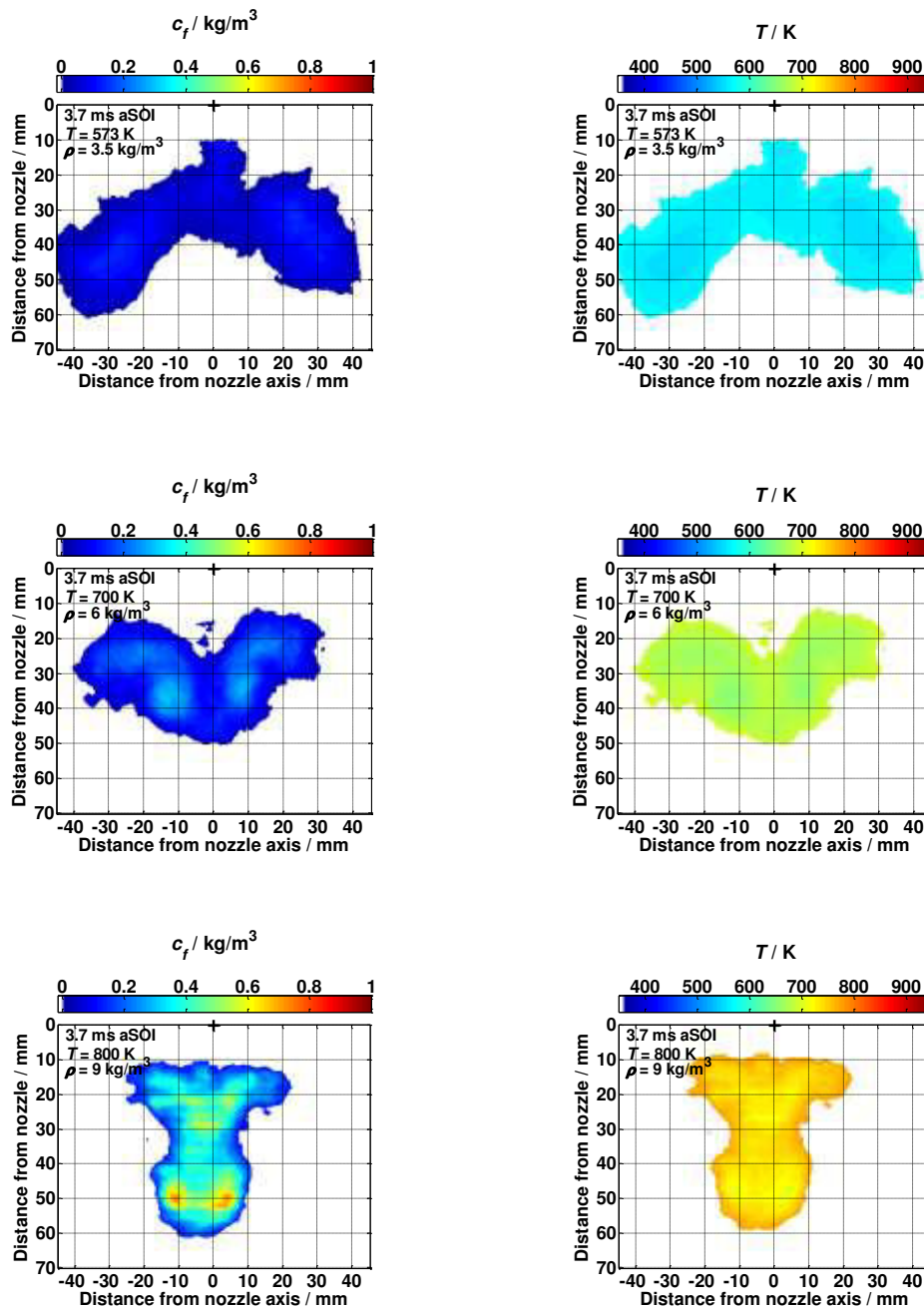


Figure 4-32: Fuel mass concentration fields (left) and their corresponding temperature (right) at Spray G conditions and variants at 3.7 ms aSOI. The fuel concentration fields were calculated from images acquired by BP340. The temperature distribution was derived from the fuel mass concentration field using an adiabatic mixing model.

temperature fields. The global fuel distribution and concentration of BP340 images are similar to that obtained from images recorded with BP292 optical filter which indicates that the potential presence of preferential evaporation has a second-order effect on the global fuel concentration (below the measurement uncertainty). As a result, any of the

two tracers channels can be used to determine the fuel concentration for the conditions investigated of this work.

## **Piezo-electric outward opening injector**

### *Multi-component fuel experiments*

So far, the fuel concentration fields of ECN Spray G injector were measured in both single- and multi-component fuel configurations. It was shown that the general jet structure is identical for both fuels. It was also observed that the distribution of *p*-DFB, which indicates the location of *iso*-octane, is the same for single- and multi-component fuel experiments when comparing images acquired by the same optical filter (BP292). Fuel concentration fields derived from BP340 images, which should indicate the location of 1-MN and thus *n*-undecane, did not show a significant difference in terms of fuel concentration gradients compared to fuel concentration fields obtained from BP292 images.

In this section, the fuel concentration fields derived from the 292-nm channel (only one channel was used here since the previous analysis showed that both channels give similar results) and their corresponding adiabatic mixing temperature fields will be determined for experiments performed with the piezo-electric injector in order to assess the temperature distribution across the spray and quantify the temperature measurement accuracy. The conditions tested with the piezo-electric injector aimed at examining the influence of nozzle geometry, ambient temperature, and density on the mixture formation.

- **ECN Spray G thermodynamic conditions**

Performing experiments with the piezo-electric injector under thermodynamic Spray G conditions and variants provide insight regarding the impact of nozzle geometry on mixture formation since the two injector technologies are compared at the same conditions in terms of ambient density and temperature.

Figure 4-33 shows fuel concentration maps and their corresponding adiabatic mixing temperature fields under these conditions. The timing corresponds to 3.7 ms aSOI, except for 9 kg/m<sup>3</sup> for which images were acquired at 3.2 ms aSOI. With 9 kg/m<sup>3</sup> and at 3.7 ms aSOI, the jet originating from the piezo-injector penetrates more deeply than a jet originating from an ECN injector and therefore part of the jet does surpass the boundaries of the laser sheet. In order to obtain an image where the jet is fully contained in the laser sheet, a shorter timing (3.2 ms aSOI) was used for 9 kg/m<sup>3</sup>.

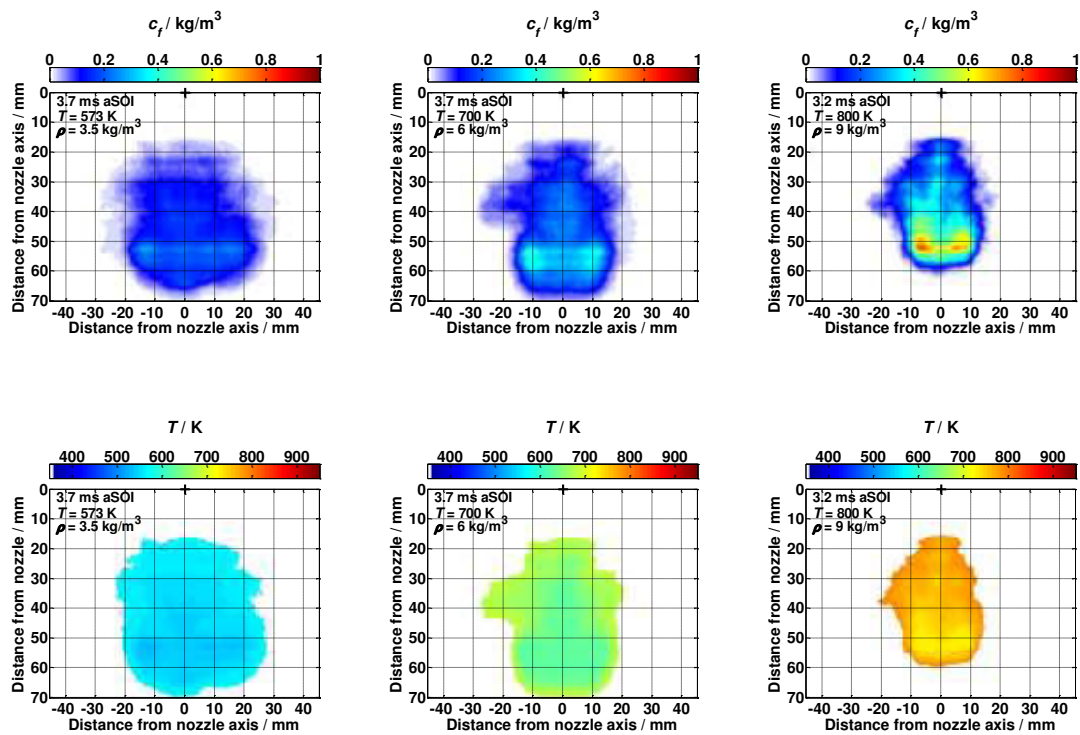


Figure 4-33: Fuel mass concentration fields (top row) for the piezo-electric injector at Spray G conditions and variants. The fuel concentration fields were calculated from 20 instantaneous images acquired by BP377 filter. The temperature distribution (bottom row) was derived from the fuel mass concentration fields using an adiabatic mixing model.

For  $3.5 \text{ kg/m}^3$ , the fuel vapor concentration is homogeneously distributed across the spray ( $\sim 0.2 \text{ kg/m}^3$ ) therefore resulting in small temperature variations in temperature ( $553 \pm 10 \text{ K}$ ). For  $6 \text{ kg/m}^3$ , the spray becomes more centered at the nozzle axis with a high concentration of fuel vapor residing in its central region ( $\sim 0.4 \text{ kg/m}^3$ ) compared to the spray periphery ( $\sim 0.2 \text{ kg/m}^3$ ). The increase in ambient density results in a significant decrease in spray width ( $\sim 10 \text{ mm}$ ). The relative temperature variation between the core and the spray periphery is  $\sim 6\%$ . For  $9 \text{ kg/m}^3$ , the spray becomes even narrower (i.e.,  $\sim 8 \text{ mm}$  decrease in spray width) and more centered at the nozzle axis. The fuel concentration in the central region of the spray increases to  $0.6 \text{ kg/m}^3$ . This creates a temperature gradient between the spray core and the spray periphery corresponding to a relative difference of  $\sim 7\%$ . Similarly to the ECN injector case, these temperature variations are relatively small when considering the effect of temperature on the fluorescence absorption and quantum yields. For this reason, the temperature distribution in this case can be considered homogenous within the jet when considering the effect of temperature on fluorescence quantum yields.

In conclusion, the spray structure originating from the Spray G and the piezo-electric injector obtained at the same thermodynamic conditions are significantly different. This implies that the jet structure is mainly driven by the nozzle geometry which has a significant impact on the mixing formation compared to thermodynamic conditions. However the same trend is observed when density and temperature are increased. The jet is more concentrated along the injector axis resulting in higher fuel concentration and temperature gradients.

- **Temperature variations at constant gas density**

The left panel of Figure 4-34 shows fuel concentration maps for an ambient density of  $5.2 \text{ kg/m}^3$  and an ambient temperature variation between 550–700 K that corresponds to a pressure range of 8–11 bar. For 550 and 600 K the fuel concentration is higher in the jet core than in the jet periphery by  $\sim 0.2$  and  $0.3 \text{ kg/m}^3$  respectively.

At the edges of the jet core, two regions appear having the highest fuel vapor concentration in the spray ( $0.6$  and  $0.7 \text{ kg/m}^3$  at 550 and 600 K, respectively). As temperature increases to 650 and 700 K, the fuel concentration across the entire jet becomes lower ( $0.28$  and  $0.27 \text{ kg/m}^3$  respectively) than the fuel concentration calculated at 550 and 600 K ( $0.31$  and  $0.32 \text{ kg/m}^3$ , respectively) thus implying a higher rate of evaporation. The general spray structure, however, is unaffected by the changes in temperature.

The high fuel concentration regions found at the edges of the jet are due the nozzle geometry. Piezo-injectors produce hollow-cone sprays that generate counter-rotating vortices at the inner and outer surfaces of the spray cone due to interactions with the surrounding gases [1, 10, 76, 77]. After the end of injection, these vortices transport the fuel vapor further downstream. For the sake of simplification, regions found on the spray edges will be referred to hereafter as vortices.

The right panel of Figure 4-34 shows the adiabatic mixing temperature fields derived from fuel concentration maps by using Espey's adiabatic mixing model. For each adiabatic mixing field, the average temperature and its variation was calculated by considering the entire 2D planar jet. Indeed, regions with higher fuel vapor concentration have

lower temperatures with respect to the ambient temperature. However, the temperature variations for all the investigated conditions are considered negligible since their relative variation is <3.5%.

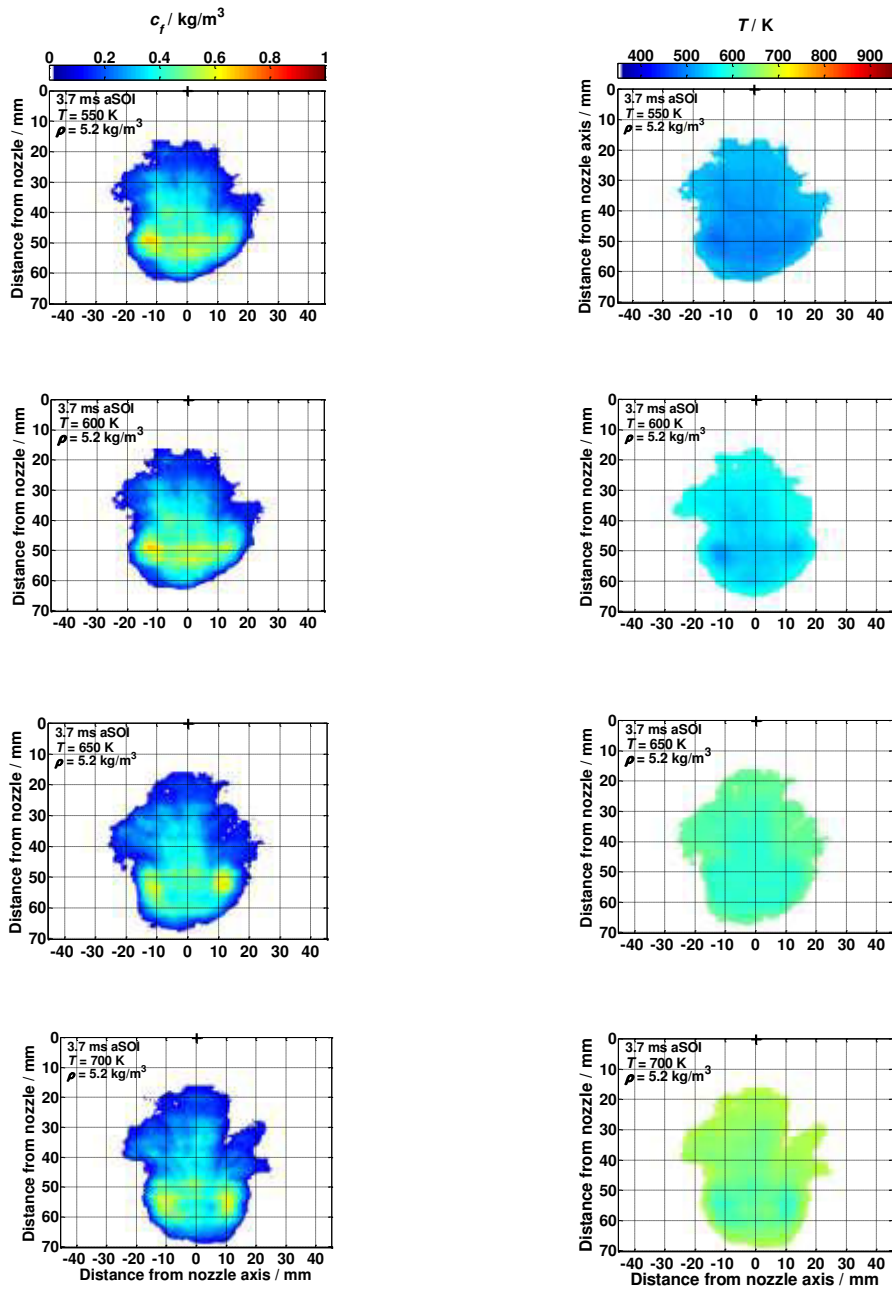


Figure 4-34: Fuel mass concentration fields (left) and their corresponding temperature fields (right) for piezo-electric injector at  $5.2 \text{ kg/m}^3$ . Temperature was varied between 550 and 700 K. The fuel concentration fields were calculated from 20 instantaneous images acquired by BP377 filter. The temperature distribution was derived from fuel mass concentration fields using an adiabatic mixing model.

Adiabatic mixing temperature fields can be once again utilized to improve the assessment of the accuracy of temperature measurements acquired by the multi-component fuel configuration. The approach adopted for improving the assessment of accuracy in single-component fuel configuration is also applied for multi-component fuel configuration. Figure 4-35 shows the calibration curve obtained from the spectral data (blue squares), two-color LIF thermometry ratios as a function of ambient temperature determined by thermocouples (red circles) and as function of average temperature derived from the adiabatic mixing temperature fields (magenta circles). Below 650 K, LIF-ratios assigned to ambient temperatures and adiabatic mixing temperatures show similar result, with a relative error being <3%. At temperatures higher than 650 K, the deviation between the two methods start to be significant (~13% at 700 K).

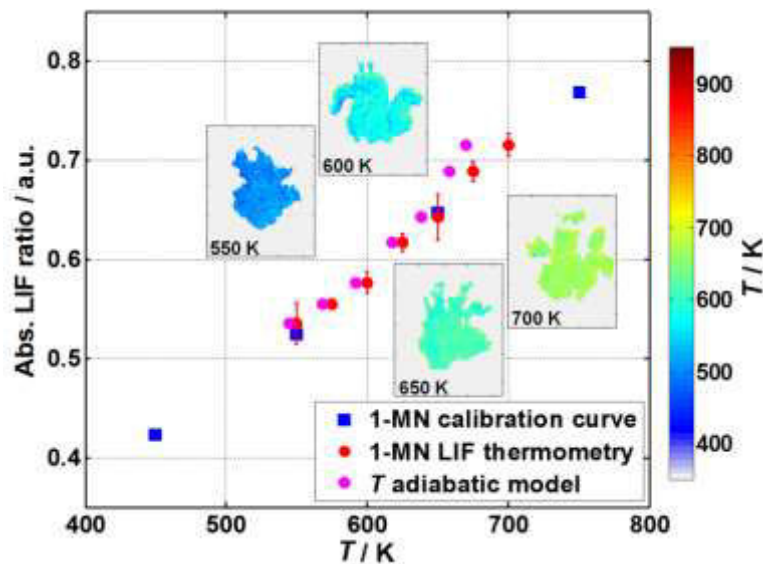


Figure 4-35: Measured two-color LIF-ratio from *Configuration*  $T_{BP377/[BP340]}$  (red circles) as a function of ambient temperature measured by thermocouples in comparison to spectroscopy cell data (blue squares). The adiabatic mixing model data (magenta circles) represent the absolute LIF-ratios attributed to average temperatures calculated from the adiabatic mixing assumption. Exemplary instantaneous measurements of the temperature distribution are given using the temperature calibration. Error bars represent the measurement uncertainty [74].

- **Gas density variations at constant temperature**

Figure 4-36 displays fuel concentration maps for an ambient temperature of 550 K and ambient densities between 6.3–12.5 kg/m<sup>3</sup> corresponding to a pressure range of 10–20 bar. For 6.3 kg/m<sup>3</sup>, the fuel distribution can be considered homogenous (~0.4 kg/m<sup>3</sup>) with the highest concentration being located at the center of the jet vortices (~0.6 kg/m<sup>3</sup>).

As density increases to  $10 \text{ kg/m}^3$ , vortices merge with the jet core and the jet becomes centered on the nozzle axis leading to a high fuel concentration in the central portion of the spray ( $\sim 0.75 \text{ kg/m}^3$ ). The vortices become smaller than those detected at  $6.3 \text{ kg/m}^3$ . However, their fuel concentration is still higher than the core of the jet ( $\sim 1 \text{ kg/m}^3$ ). For  $12.5 \text{ kg/m}^3$ , the jet becomes even more centered at the nozzle axis where the vortices combine to form a high concentration fuel cloud ( $\sim 1.25 \text{ kg/m}^3$ ). In conclusion, density increase has a severe impact on the jet structure, it becomes centered at the nozzle axis thus forming a high concentration fuel vapor area. Consequently, at high ambient densities, the jets are characterized by strong gradients in fuel concentration.

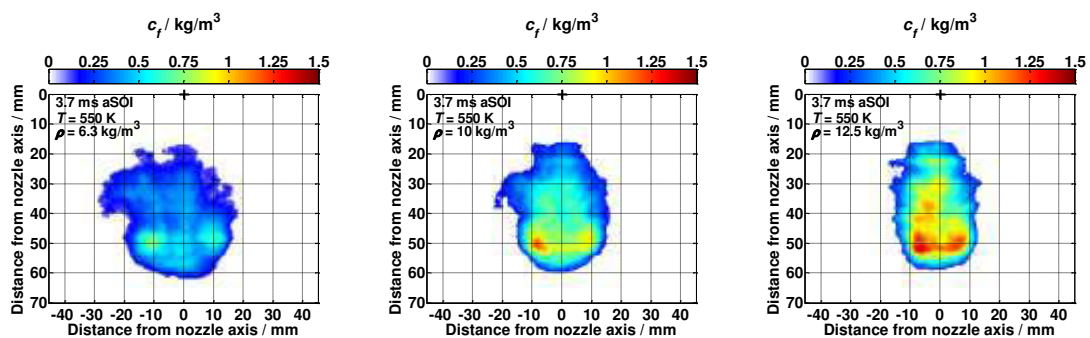


Figure 4-36: Fuel mass concentration fields for piezo-electric injector at 550 K. Ambient density ranges between  $6.3\text{--}12.5 \text{ kg/m}^3$  while temperature ranges between  $550\text{--}700 \text{ K}$ . The fuel concentration fields were calculated from 20 instantaneous images acquired with a BP377 filter. The temperature distribution was derived from the fuel mass concentration field using the adiabatic mixing model.

#### 4.3.3 Impact of nozzle geometry on preferential evaporation and spray formation

It was previously concluded from fuel concentration fields of ECN Spray G and piezo-electric injector experiments that the fuel jet structure is strongly influenced by the nozzle geometry. It is therefore of interest to analyze the impact of nozzle geometry on preferential evaporation. For this purpose, the signal fluorescence ratio of images acquired by the image doubler is investigated for both injectors at ECN conditions and variants.

The methodology adopted to detect the existence of preferential evaporation is based on quantitative measurements for which the measurement accuracy and precision are determined using the identical filters configuration (*Configuration I*<sub>[BP292/BP292]</sub>) before performing LIF-ratio measurements with filters centered at 292 and 340-nm (*Configuration E*<sub>[BP292/BP340]</sub>) in order to detect the signal emitted by *p*-DFB and 1-MN, respectively. For

more information regarding the methodology, refer to section 4.1. The  $2\sigma$  precision is determined by calculating the  $2\sigma$  (standard deviation) from a two-tracer LIF-ratio standard deviation image obtained from a set of jet images acquired by Configuration  $I_{[BP292/BP292]}$ . Similarly, the  $2\sigma$  (standard deviation) calculated from the average LIF-ratio image acquired by Configuration  $I_{[BP292/BP292]}$  is used to determine the measurement accuracy [78] .

The quantitative knowledge of precision and accuracy is then used to determine the significant results from the two-tracer LIF-ratio images obtained by *Configuration*  $E_{[BP292/BP340]}$ . In reality, instantaneous images are affected by the measurement precision as well as the accuracy and therefore areas where preferential evaporation occurs are those which are higher than  $1 \pm (2\sigma \text{ accuracy} + 2\sigma \text{ precision})$ . For the sake of simplification, only the precision information is used here on instantaneous two-color LIF-ratio images to detect regions where the deviation from unity is significant. The accuracy information is applied on averaged two-color LIF-ratio images to distinguish regions with deviations higher than the measurement accuracy. Those regions indicate the localization of preferential evaporation.

Figure 4-37 and Figure 4-38 show average and instantaneous images respectively that are obtained from *Configuration*  $E_{[BP292/BP340]}$  for the Spray G (top) and the piezo injector (bottom) for ECN conditions and variants. The iso-contours shown on the two-tracer LIF-ratio average images in Figure 4-37 indicate regions where the deviation from unity is significant (i.e., larger than the accuracy of the measurement ( $2\sigma$ ), i.e.  $\pm 0.12$ ). The iso-contours shown on instantaneous two-tracer LIF-ratio images in Figure 4-38 represent regions that are higher than the measurement precision  $2\sigma$  ( $\pm 0.10$ ). As previously mentioned, only precision was used to define iso-contours on instantaneous images to simplify the analysis. Since the LIF-ratio is the signal ratio of high-volatility tracer (BP292) to low-volatility tracer (BP340) the regions with results higher than unity indicate the location with accumulated high-volatility fuel components.

Consequently, regions with LIF-ratios lower than unity indicate where the low-volatility

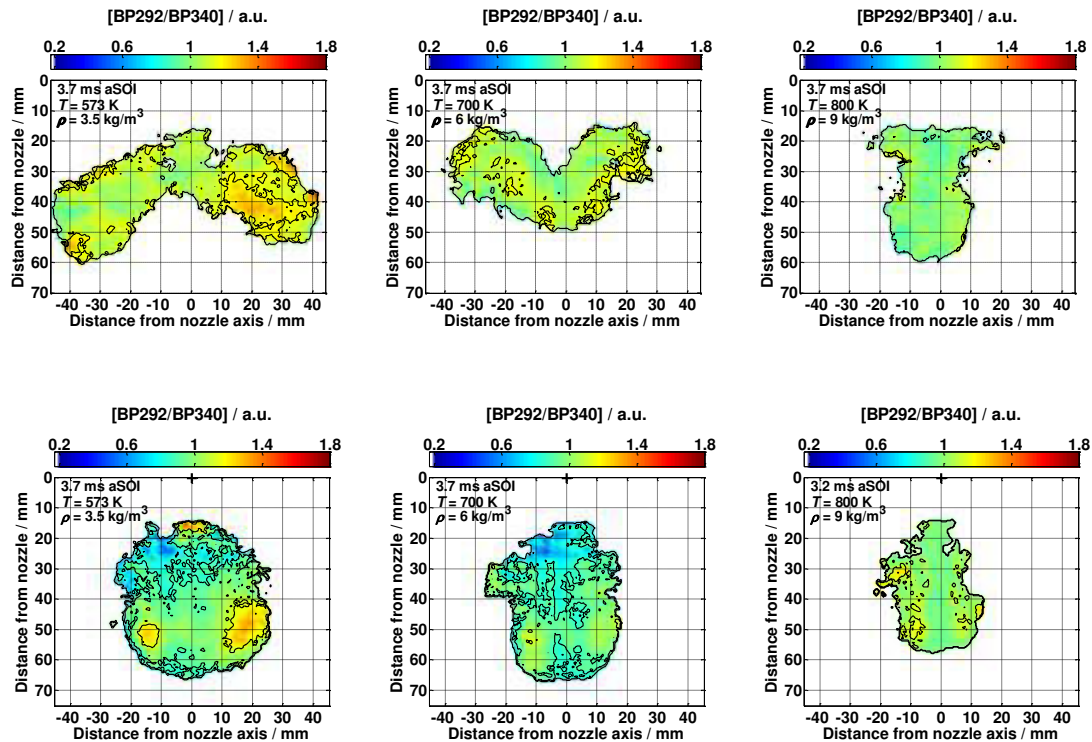


Figure 4-37: Averaged two-tracer LIF-ratio images obtained by *Configuration E*<sub>[BP292/BP340]</sub> with ECN Spray G (top) and the piezo-electric injector (bottom) under ECN conditions and variants. The images are based on averaging 15 instantaneous images. Iso-contours at 0.88 and 1.12 indicate the regions where the deviation from unity is significant (i.e., larger than the measurement accuracy ( $\pm 0.12$ )).

fuel component is localized. For ECN Spray G at  $3.5 \text{ kg/m}^3$  ambient gas density, Regions with LIF-ratios higher than unity are located at the lower portion of the jet plumes unlike in the cases with the piezo injector where they are located at the core of the jet vortices. Moreover, the LIF-ratios for Spray G are lower than those found for piezo-injector measurements implying a more pronounced preferential evaporation in the latter case. As ambient density increases to  $6 \text{ kg/m}^3$ , the LIF-ratios become homogeneous for Spray G. However, the effect of preferential evaporation is still significant, yet less pronounced than at  $3.5 \text{ kg/m}^3$ , for the piezo injector. At  $9 \text{ kg/m}^3$  both Spray G and piezo-injector measurements show a homogeneous distribution of the LIF-ratio, implying that preferential evaporation is no longer significant.

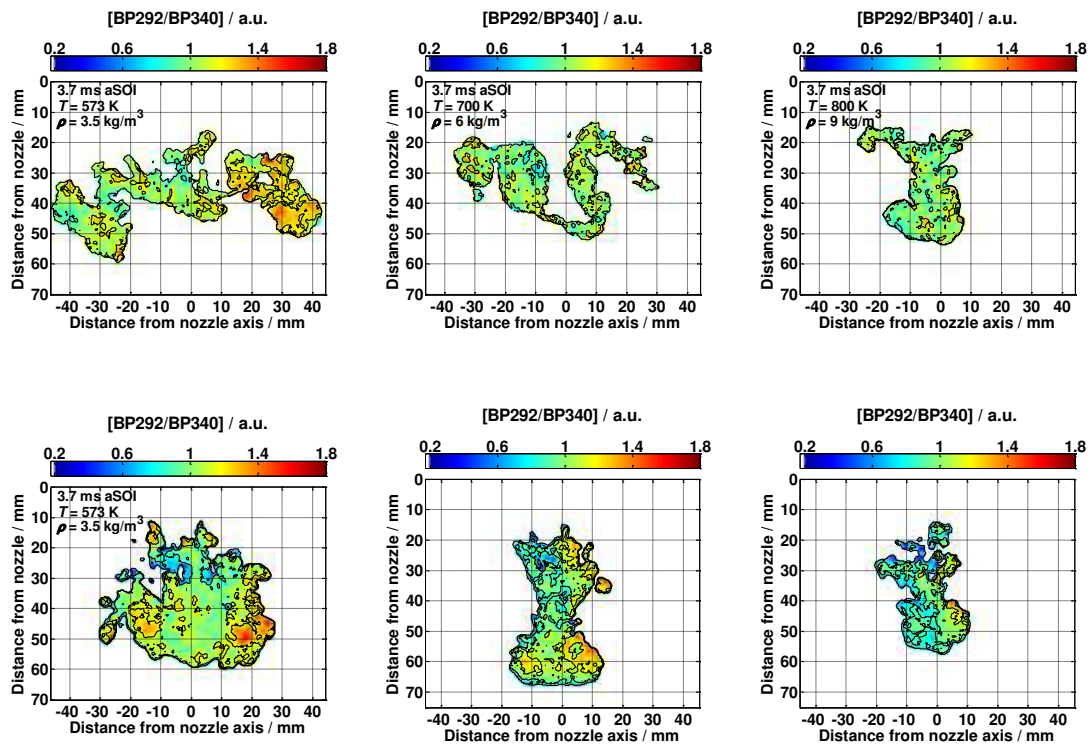


Figure 4-38: Instantaneous two-tracer LIF-ratio images obtained by *Configuration E*<sub>[BP292/BP340]</sub> with Spray G (top) and piezo injector (bottom) under ECN conditions and variants. Iso-contours at 0.90 and 1.10 indicate the regions where the deviation from unity is significant (i.e., larger than the measurement precision ( $\pm 0.10$ )).

In conclusion, preferential evaporation is present for Spray G and the piezo-injector jets, however with different spatial distribution. The injector type and the ambient gas density have a significant impact on the jet structure which can influence fuel vaporization. Based on the analysis of the injection process, an explanation for the localization of preferential evaporation is suggested:

- The Spray G injector is a multi-hole injector that produces a full-cone spray. The injection pressure is the main driver that initially propels the spray allowing liquid penetration to take place at early injection timings. During injection, a strong aerodynamic motion is generated by air entrainment which persists after the end of injection. This motion becomes the main driver for the propagation of the vaporized fuel jet [79]. Since the high-volatility components evaporate more rapidly than the low-volatility components, the former are vaporized and preferentially entrained by the aerodynamic motion at a time when the low-volatility components are still liquid. As a result, the high-volatility components are located at the

tip of the jet while the low-volatility components remain in the upper part of the jet.

- The piezo-electric injector, on the other hand, generates a hollow-cone spray where tangential forces of the entrained air create a momentum flux towards the centerline of the jet thus forming a circular vortex. Droplets are located in the periphery of the vortex because of centrifugal forces while vapor is mainly located in its center [10, 67]. This distribution of droplets and vapor results in a corresponding segregation of the low and high-volatility components at the periphery and center of the vortex, respectively.

Knowing that the two jets were investigated under the same ambient conditions, it can be concluded that the injector technology has a strong impact on the localization and the magnitude of preferential evaporation. The piezo injector amplifies this effect as even at high densities (i.e.,  $6 \text{ kg/m}^3$ ) preferential evaporation was detected.

#### **4.3.4 Impact of temperature on preferential evaporation**

For the standard Spray G conditions, temperature and gas density are varied at the same time which complicates the assessment of the influence of each quantity on preferential evaporation. To investigate the effect of temperature independently, experiments were therefore carried out here with the piezo-electric injector at a constant gas density of  $5.2 \text{ kg/m}^3$  while varying the temperature between 550–700 K .

In section 4.3.2, adiabatic mixing temperature fields showed small fluctuations across the spray even at the highest investigated ambient temperature (i.e.,  $\pm 19 \text{ K}$  corresponding to a relative error of  $\sim 3\%$  at 700 K). Moreover, LIF thermometry measurements displayed a quasi-homogenous temperature distribution across the spray since temperature fluctuations for all the investigated temperature conditions (550–700 K) falls within the measurement uncertainty ( $\pm 28 \text{ K}$ ). Therefore, the interpretation of two-tracer LIF-ratios is independent of temperature distribution across the spray since the latter was shown to be homogenous.

The measurement precision and accuracy were also determined for both detection channels of the image doubler using the identical filters configuration (*Configuration I<sub>{BP292/BP292}</sub>*). The precision and accuracy were  $\pm 0.10$  and  $\pm 0.12$ , respectively.

After assessing the temperature distribution in the jet and the sensitivity of the whole detection system, the two-color LIF-ratio images were investigated again using the information from the temperature measurements. Figure 4-39 shows average (left panel) and

instantaneous (right panel) images of two-tracer LIF-ratios obtained by *Configuration*  $E_{[BP292/BP340]}$  for various ambient temperatures. Average images are obtained from 15 instantaneous images. Iso-contours indicate regions where the deviation from unity is higher than the measurement precision ( $\pm 0.10$ ) for instantaneous images and accuracy ( $\pm 0.12$ ) for average images. At 550 and 600 K, instantaneous and average images exhibit a significant inhomogeneity of the fluorescence ratio. The LIF-ratios are above unity in the vortex core but are lower in the central portion of the fuel jet. Here, the high-volatility components of the multi-component fuel are preferentially located in the vortex cores while low-volatility component remain in the central portion of the jet as discussed before in section 4.3.3. At 700 K, however, the effect is less significant and regions where the deviation from unity is significant in the context of the precision of the measurement become rare. This result is consistent with the fact that at higher temperatures, evaporation is faster and therefore preferential evaporation effects are less pronounced.

In conclusion, quantitative measurements of preferential evaporation of multi-component fuels at engine-relevant conditions showed that high temperatures ( $>600$  K) reduce the effect of preferential evaporation, which is consistent with the fact that evaporation is faster for higher ambient temperatures. At low temperatures (550–600 K), evaporation is slower giving time for each fuel component to evaporate at a different rate which then enhances the effects of preferential evaporation.

In conclusion, quantitative measurements of preferential evaporation of multi-component fuels at engine-relevant conditions showed that high temperatures ( $>600$  K) reduce the effect of preferential evaporation, which is consistent with the fact that evaporation is faster for higher ambient temperatures. At low temperatures (550–600 K), evaporation is slower giving time for each fuel component to evaporate at a different rate which then enhances the effects of preferential evaporation.

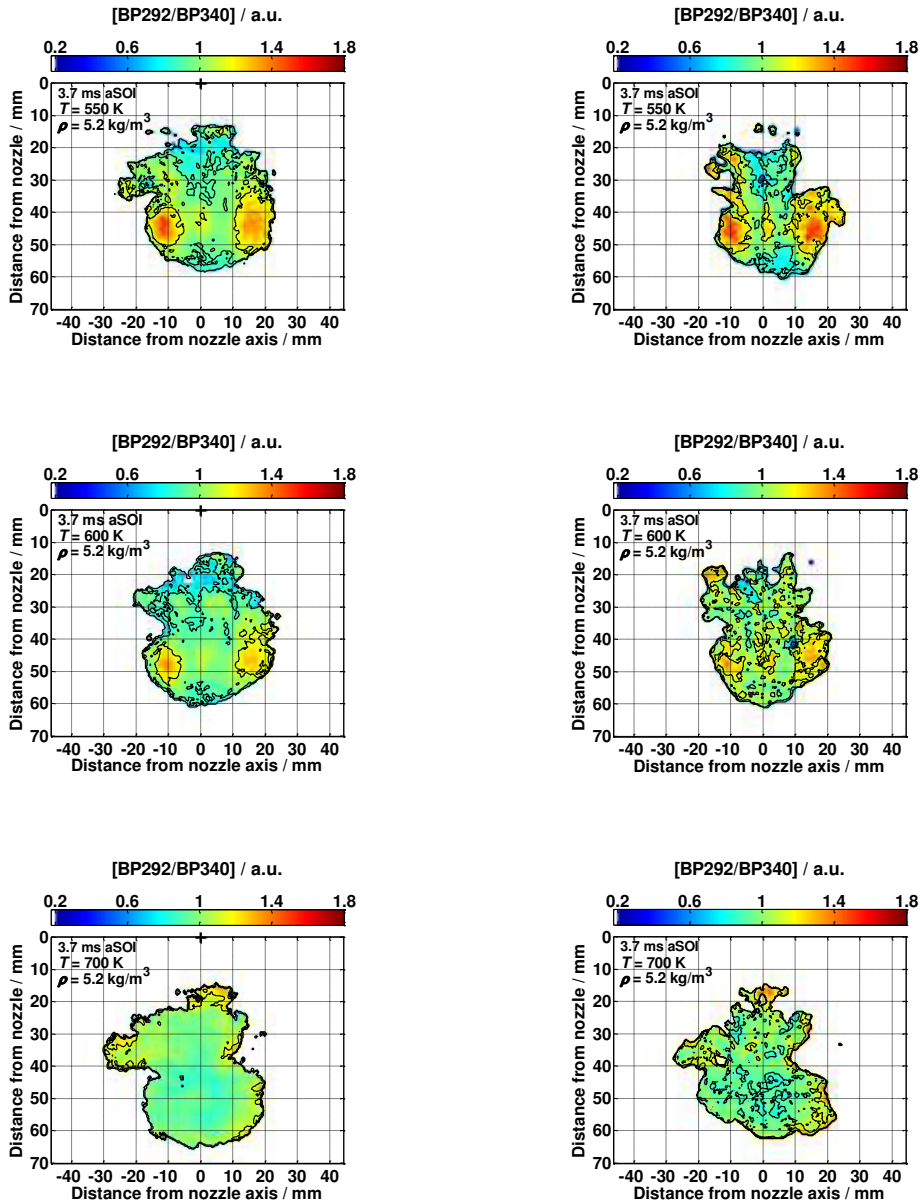


Figure 4-39: Two-tracer LIF-ratio images taken from *Configuration*  $E_{[BP292/BP340]}$ . Left: Average from 15 single-shot images. Right: Instantaneous images. For average images, iso-contours at 0.88 and 1.12 indicate the regions where the deviation from unity is significant (higher than the measurement accuracy ( $\pm 0.12$ )). For instantaneous images, iso-contours at 0.90 and 1.10 indicates the regions where the deviation from unity is higher than the measurement precision ( $\pm 0.10$ ).

#### 4.3.5 Impact of density on preferential evaporation

Experiments have shown that preferential evaporation is highly influenced by the jet structure and also by the ambient temperature. The jet structure mainly influences the localization of areas that are unmixed as a consequence of preferential evaporation while ambient temperature impacts its magnitude. Gas density also influences preferential evaporation. Note that a change in density consequently leads to an increase in ambient pressure. Density mainly influences the jet form while pressure has an impact on the evaporation process.

The impact of density on preferential evaporation was evaluated with the piezo-electric injector since this injector was found to generate the strongest preferential evaporation effect. Therefore, ambient density was varied between 6.3–12 kg/m<sup>3</sup> while keeping the ambient temperature at 550 K. Note that at 550 K significant preferential evaporation effects were observed, showing that this condition makes a good reference temperature for these experiments. Increasing the density consequently leads to an increase in ambient pressure (10–20 bar).

Figure 4-40 shows the instantaneous two-color LIF-ratio images at 550 K and at various density conditions. Iso-contours at 0.88 and 1.12 indicate the regions where the deviation from unity is higher than the measurement accuracy ( $\pm 0.12$ ). For 6.3 kg/m<sup>3</sup> (~10 bar) the jet structure is similar to the one observed at 5.2 kg/m<sup>3</sup> (550 K), with pronounced LIF gradients at the vortex core and the central portion of the jet. This means that the high-volatility component is situated at the vortex core while the low-volatility component is found at the spray center. As ambient density increases to 10 kg/m<sup>3</sup> (~15 bar), the jet becomes more concentrated at the nozzle axis with the vortices merging in the central portion of the jet hence decreasing the magnitude of the effect of preferential evaporation. For 12.5 kg/m<sup>3</sup>, the spray becomes even narrower and the LIF-ratio distribution becomes homogeneous (i.e., absence of preferential evaporation). The increase in density is known to promote high rates of air entrainment which consequently result in faster evaporation of fuel components. The boiling temperature, however, increases with increasing pressure delaying evaporation.

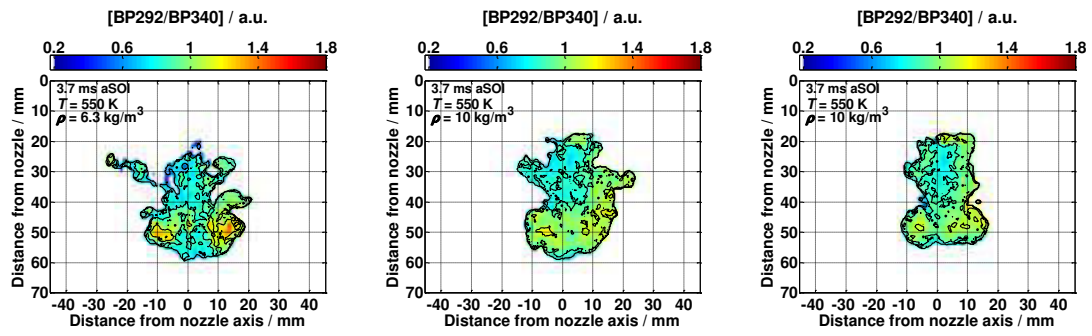


Figure 4-40: Instantaneous two-tracer LIF-ratio images taken from Configuration  $E_{[BP292/BP340]}$  and their corresponding temperature fields for various ambient densities ranging between 6.3–12 kg/m<sup>3</sup>. Iso-contours at 0.90 and 1.10 indicate the regions where the deviation from unity is significant (higher than the measurement precision of  $\pm 0.10$ ).

## 5 Outlook

The objective of this work was to examine the effects of preferential evaporation on the mixture formation during the injection of multi-component fuels for two injector technologies. The impact of temperature and gas density on preferential evaporation was investigated. Regardless of the effectiveness of the methodology established in this work and its findings, some areas still require further investigations and improvements. The following perspectives are suggested:

- The temperature measurement precision of the three-detection channel configuration had a precision lower than that of the two-detection channel configuration. This is due to the use of an image doubler in front of one of the cameras which decreases the precision of the measurement due to reduced signal-to-noise ratios and can reduce the accuracy through vignetting. Using an additional camera instead would improve the results.
- Both *p*-difluorobenzene and 1-methylnaphthalene two-color LIF thermometry are based on the red-shift of the fluorescence spectra with increasing temperature. Measurements performed at high-temperature (>700 K) and high-pressure (>10 bar) conditions suffered from poor signal-to-noise ratios. The laser fluence used for measurements under these conditions was based on limits for linear response determined at 7 bar for 453 K. For high temperature conditions, however, the linear range extends to higher fluences that could be used in future measurements to further improve the image quality.
- All experiments were performed in an O<sub>2</sub>-free environment. This is, however, not representative of real-life engine conditions. Measurements in the presence of O<sub>2</sub> require further photophysical characterization of both tracers for a range of O<sub>2</sub> partial pressure in the pressure and temperature range of interest.
- Spray G experiments showed a severe change in jet structure with increasing gas density as the jet collapsed and became centered at the nozzle axis. In this work, the change in structure was attributed to the increase in air entrainment which generated aerodynamic forces eventually leading to the collapse of the jet. The same forces are responsible for the presence of steep gradients in the LIF ratio in the lower part of the jet plumes. To further understand the jet movement, velocity fields across the jet would need to be measured. These velocity fields could be obtained via particle image velocimetry (PIV).

## 6 Conclusions

For the design of future internal combustion engines and engine optimization, it is crucial to understand fuel evaporation and mixture formation in the combustion chamber. A detailed knowledge of the underlying processes enhances the capability of simulations. Most simulations so far treat fuel evaporation based on single-component mechanisms due to the lack of experimental data based on the evaporation and mixing of multi-component fuels. The primary issue addressed in this work is related to preferential evaporation which occurs under certain operating conditions due to the presence of various volatility classes in gasoline. Other properties like the temperature distribution and the distribution of the fuel vapor across the jet must also be assessed to describe the process of interest.

For this purpose, the work presented in this PhD focuses on developing a non-intrusive laser diagnostics technique for the simultaneous imaging measurement of preferential evaporation, temperature, and fuel concentration across vaporized fuel jets representative of engine conditions. The developed technique is based on two-tracer laser-induced fluorescence (LIF) with single-wavelength excitation. Measurements were performed by using a three-component fuel with evaporation characteristics similar to gasoline. A pair of aromatic tracers, *p*-difluorobenzene (*p*-DFB) and 1-methylnaphthalene (1-MN) capable of co-evaporating with the high-to-medium and the low-volatility end of the fuel respectively, was selected based on equilibrium evaporation calculations. This tracer pair also enabled temperature measurements via two-color LIF thermometry due to the high sensitivity of 1-MN LIF to temperature. Aromatic tracers were selected to avoid photophysical interaction between the two tracers that can be severe in case of combination of aromatics and ketones. The spectral properties of *p*-DFB and 1-MN were analyzed for various temperatures, pressures, and bath gas compositions. The calibration curves of temperature measurements from photophysical data were obtained at various temperatures (300–900 K) in 1 bar N<sub>2</sub> and for different O<sub>2</sub> partial pressures. The low level of photophysical interaction between the two tracers was also verified by characterizing the tracer mixture with fluorescence lifetime measurements. The photophysical measurements are important because a major part of this study was to perform quantitative LIF measurements where the assessment of measurement accuracy and precision is key.

Jet imaging measurements were carried out in an O<sub>2</sub>-free environment in a high-pressure high-temperature vessel capable of reproducing pressure and temperature conditions

typical for IC engines. The use of three detection channels was necessary for the application of the two-tracer technique to determine temperature and preferential evaporation from the ratio of two signals. The investigation focused on two types of fuel jets generated by (1) a full-cone spray from an ECN Spray G injector and (2) a hollow-cone spray from a piezo-electric injector. Experiments were performed with single- and multi-component fuels. For the single-component fuel, a two-detection channel setup was used to image the temperature distribution via two-color  $p$ -DFB LIF. One channel was also used for calculating the fuel vapor concentration distribution. The measured fuel concentration fields were also used to calculate the temperature distribution across the jet by applying the adiabatic mixing model. The results were then compared to those obtained via two-color LIF thermometry to determine the accuracy of the temperature measurement.

The red-shift of DFB and 1-MN spectra with increasing temperature enabled the determination of the temperature distribution with a precision of  $\pm 25$  and  $\pm 28$  K for DFB and 1-MN LIF thermometry, respectively. The  $\pm 3$  K discrepancy in precision is due to the different experimental configurations used. LIF thermometry measurements displayed a quasi-homogenous temperature distribution across the spray since temperature fluctuations for the investigated temperature range fall within the measurement precision. Therefore, the interpretation of two-tracer LIF ratios is independent of temperature distribution across the spray since the latter was shown to be homogenous.

The temperature measurement accuracy was determined by comparing LIF thermometry results with mean temperature data derived from temperatures calculated from measured fuel concentration using an adiabatic evaporation and mixing assumption. The measurement accuracy deteriorates with increasing temperature and the deviation between both methods reached 13% at 800 K.

The accuracy and the precision of the preferential evaporation measurement technique was first determined from a configuration with two cameras detecting signal in identical wavelength bands. The accuracy and precision was  $\pm 0.12$  and  $\pm 0.10$ , respectively. The quantitative examination of preferential evaporation using two-tracer LIF under engine-relevant conditions was carried out for a Spray G and a piezo-electric injector at 3.5, 6 and 9 kg/m<sup>3</sup> at 573, 700, and 800 K, respectively. These investigations aimed at studying the impact of nozzle geometry and jet structure on mixture formation and preferential evaporation. For Spray G, high LIF-ratio intensities (indicating high amounts of low-volatility component) were found in the lower end of the jet while for the piezo injector hollow-cone jet, the high LIF-ratios were found preferentially in the vortices.

The impact of gas temperature on preferential evaporation was examined for fuel jets issued from the piezo-electric injector. The temperature was varied between 550–700 K while keeping the gas density constant at 5.2 kg/m<sup>3</sup>. Fluctuations in the LIF-ratio were prominent at 550–600 K. At higher temperatures the LIF-ratio distribution became homogeneous implying the disappearance of preferential evaporation. The influence of the gas density was analyzed in the 6.3–12 kg/m<sup>3</sup> range while keeping the temperature at 550 K. High fluctuations in the LIF-ratios were present at 6.3 kg/m<sup>3</sup>, whereas at higher densities, fluctuations became negligible due to the increase of air entrainment which consequently increased the rate of evaporation.

The findings of this work show that preferential evaporation does exist at engine-relevant conditions which can have an impact on the mixing process and can be investigated with the developed method. The results presented in this dissertation can be used to verify CFD models that are based on multi-component fuels providing that injectors are fully characterized.

## 7 References

- [1] Baumgarten, C. "Mixture Formation in Internal Combustion Engine," Heat, Mass Transfer, Springer Berlin Heidelberg, 2006.
- [2] Mitroglou, N., Nouri, J.M., Gavaises, M., and Arcoumanis, C., "Spray characteristics of a multi-hole injector for direct-injection gasoline engines," International Journal of Engine Research 7:255–270, 2006.
- [3] Hoffmann, K.H., Schwerdt, P., and Huber, G., "Piezo-control valve for fuel injection systems of internal combustion engines," Patents, 1998, US5740969.
- [4] Bosch, "High-pressure piezo injector HDEV4: Gasoline Systems," Stuttgart, Germany, [http://products.bosch-mobility-solutions.com/media/en/ubk\\_europe/db\\_application/downloads/pdf/antrieb/de\\_5/gs\\_datenblatt\\_piezo\\_hochdruck\\_einspritzventil\\_hdev4\\_de.pdf](http://products.bosch-mobility-solutions.com/media/en/ubk_europe/db_application/downloads/pdf/antrieb/de_5/gs_datenblatt_piezo_hochdruck_einspritzventil_hdev4_de.pdf).
- [5] Gupta, H.N., "Fundamentals of Internal Combustion Engines," PHI Learning, 2012.
- [6] Schulz, C. and Sick, V., "Tracer-LIF diagnostics: quantitative measurement of fuel concentration, temperature and fuel/air ratio in practical combustion systems," Progress in Energy and Combustion Science 31:75–121, 2005.
- [7] James Speight, "Synthetic Fuels Handbook," McGraw-Hill, 2008.
- [8] Styron, J.P., Kelly-Zion, P.L., Lee, C.F., Peters, J.E., White, R.A., Lucht, R.P., "Multicomponent liquid and vapor fuel distribution measurements in the cylinder of a port-injected, spark-ignition engine," SAE Technical Paper Series 2001-01-0243, 2000.
- [9] Scholz, J., Wiersbinski, T., and Beushausen, V., "Planar Fuel-Air-Ratio-LIF with Gasoline for Dynamic Mixture-Formation Investigations," SAE Technical Paper Series 2007-01-0645, 2007.
- [10] Zigan, L., Schmitz, I., Flügel, A., Wensing, M., Leipertz, A., "Structure of evaporating single- and multicomponent fuel sprays for 2nd generation gasoline direct injection," Fuel 90:348–363, 2011.
- [11] Kelly-Zion, P.L., Styron, J.P., Lee, C.F., Lucht, R.P., Peters, P.E., White, R.A., "Multicomponent liquid and vapor fuel measurements in the cylinder of a port-injected, spark ignition engine," Proceedings of the Combustion Institute 27:2111–2117, 1998.

- [12] Han, D. and Steeper, R.R., "An LIF equivalence ratio imaging technique for multi-component fuels in an IC engine," *Proceedings of the Combustion Institute* 29:727–734, 2002.
- [13] Williams, B., Ewart, P., Stone, R., Ma, H., Walmsley, H., Cracknell, R., Stevens, R., Richardson, D., Qiao, J., Wallace, S., "Multi-Component Quantitative PLIF: Robust Engineering Measurements of Cyclic Variation in a Firing Spray-Guided Gasoline Direct Injection Engine," *SAE Technical Paper Series* 2008-01-1073, 2008.
- [14] Krämer, H., Einecke, S., Schulz, C., Sick, V., Natrass, S.R., Kitching, J.S., "Simultaneous Mapping of the Distribution of Different Fuel Volatility Classes Using Tracer-LIF Tomography in an IC Engine," *SAE Technical Paper Series* 982467, 1998.
- [15] Egermann, J. and Leipertz, A., "Influence of Fuel Properties on Mixture Formation: An Experimental Analysis for High Pressure Swirl Injectors," *SAE Technical Paper Series* 2000-01-2863, 2000.
- [16] Myong, K.J., Suzuki, H., Senda, J., and Fujimoto, H., "Spray inner structure of evaporating multi-component fuel," *Fuel* 87:202–210, 2008.
- [17] Myong, K.J., Arai, M., Tanaka, T., Senda, J., Fujimoto, H., "An experimental investigation and numerical analysis of multi-component fuel spray," *JSME International Journal B* 47:200–206, 2004.
- [18] Idicheria, Cherian A. and Pickett, Lyle M., "Quantitative Mixing Measurements in a Vaporizing Diesel Spray by Rayleigh Imaging," *SAE Technical Paper Series* 2007-01-0647 (2007).
- [19] Brenn, G., "Handbook of Experimental Fluid Mechanics, C. Tropea, A.L. Yarin, J.F. Foss (Eds.), Springer (2007).
- [20] Schulz, C., "Laser-based imaging measurements in combustion: New results for fuel/air mixture and temperature diagnostics," *Journal of Physics: Conference Series* 45:27, 2006.
- [21] Koban, W., Koch, J.D., Hanson, R.K., and Schulz, C., "Toluene LIF at elevated temperatures: Implications for fuel-air ratio measurements," *Applied Physics B* 80:147–150, 2005.

- [22] Thurber, M.C. and Hanson, R.K., "Pressure and composition dependences of acetone laser-induced fluorescence with excitation at 248, 266, and 308 nm," *Applied Physics B* 69:229–240, 1999.
- [23] Einecke, S., Schulz, C., and Sick, V., "Measurement of temperature, fuel concentration and equivalence ratio fields using tracer LIF in IC engine combustion," *Applied Physics B* 71:717–723, 2000.
- [24] Peterson, B. and Sick, V., "Simultaneous flow field and fuel concentration imaging at 4.8 kHz in an operating engine," *Applied Physics B* 97:887–895, 2009.
- [25] Choi, D.S., Choi, G.M., and Kim, D.J., "Spray structures and vaporizing characteristics of a GDI fuel spray," *KSME International Journal* 16:999–1008, 2002.
- [26] Schulz, F., Schmidt, J., and Beyrau, F., "Development of a sensitive experimental set-up for LIF fuel wall film measurements in a pressure vessel," *Experiments in Fluids* 56:56–98, 2015.
- [27] Trost, J., Zigan, L., and Leipertz, A., "Quantitative vapor temperature imaging in DISI-sprays at elevated pressures and temperatures using two-line excitation laser-induced fluorescence," *Proceedings of the Combustion Institute* 34:3645–3652, 2013.
- [28] Zegers, R.P., Yu, M., Bekdemir, C., Dam, N.J., Luijten, C.C.M., De Goey, L.P.H., "Temperature measurements of the gas-phase during surrogate diesel injection using two-color toluene LIF," *Applied Physics B* 112:7–23, 2013.
- [29] Bengt Johansson, Hans Neij, Marcus Aid, Greger Juhlin (ed.), "Investigations of the Influence of Mixture Preparation on Cyclic Variations in a SI-Engine, Using Laser Induced Fluorescence," ISBN 0148-7191.
- [30] Kaiser, S.A. and Long, M.B., "Quantitative planar laser-induced fluorescence of naphthalenes as fuel tracers," *Proceedings of the Combustion Institute* 30:1555–1563, 2005.
- [31] Sponer, H., "Wavelength shifts in the near ultraviolet spectra of fluorinated benzenes," *Journal of Chemical Physics* 22:234–235, 1954.
- [32] Steer, R.P., Swords, M.D., and Phillips, D., "Vibrational relaxation in first electronically excited singlet state of fluorobenzenes," *Chemical Physics* 34:95–102, 1978.
- [33] Matheson, M.S. and Zabor, J.W., "Fluorescence of carbonyl compounds in the gas phase," *Journal of Chemical Physics* 7:536–538, 1939.

- [34] Lozano, A., Yip, B., and Hanson, R.K., "Acetone: a tracer for concentration measurements in gaseous flows by planar laser-induced fluorescence," *Experiments in Fluids* 13:369–376, 1992.
- [35] Neij, H., Johansson, B., Aldén, M., "Development and demonstration of 2D-LIF for studies of mixture preparation in SI engines," *Combustion and Flame* 99:449–457, 1994.
- [36] Koch, J.D., "Fuel Tracer Photophysics for Quantitative Planar Laser-Induced Fluorescence," PhD Thesis, Stanford University, 2005.
- [37] Boekman, R.F. and Kearns, D.R., "Electronic-relaxation processes in acetone," *Journal of Chemical Physics* 44:945–949, 1966.
- [38] Koch, J.D., Gronki, J., and Hanson, R.K., "Measurements of near-UV absorption spectra of acetone and 3-pentanone at high temperatures," *Journal of Quantitative Spectroscopy and Radiative Transfer* 109:2037–2044, 2008.
- [39] Rossow, B., "Processus photophysiques de molecules organiques uorescentes et du kerosene applications aux foyers de combustion: applications aux foyers de combustion," PhD Thesis, Pairs-Sud University, 2014.
- [40] Grossmann, F., Monkhouse, P.B., Ridder, M., Sick, V., Wolfrum, J., "Temperature and pressure dependences of the laser-induced fluorescence of gas-phase acetone and 3-pentanone," *Applied Physics B* 62:249–253, 1996.
- [41] Faust, S., "Characterisation of organic fuel tracers for laser-based quantitative diagnostics of fuel concentration, temperature, and equivalence ratio in practical combustion processes," PhD Thesis, University of Duisburg-Essen, 2013.
- [42] Braeuer, A., Beyrau, F., and Leipertz, A., "Laser-induced fluorescence of ketones at elevated temperatures for pressures up to 20 bars by using a 248 nm excitation laser wavelength: Experiments and model improvements," *Applied Optics* 45:4982–4989, 2006.
- [43] Förster, T., "Zwischenmolekulare Energiewanderung und Fluoreszenz," *Annalen der Physik* 437:55–75, 1948.
- [44] Dexter, D.L., "A theory of sensitized luminescence in solids," *The Journal of Chemical Physics* 21:836–850, 1953.

- [45] Birks, J.B., Salet, M., and Leite, S.C., "Energy transfer in organic systems. VIII. Quenching of naphthalene fluorescence by biacetyl," *Journal of Physics B* 3:417–424, 1970.
- [46] Brown, R.G. and Phillips, D., "Quenching of the first excited singlet state of substituted benzenes by molecular oxygen," *Journal of the Chemical Society, Faraday Transactions 2: Molecular and Chemical Physics* 70:630–636, 1974.
- [47] Nau, W.M. and Scaiano, J.C., "Oxygen quenching of excited aliphatic ketones and diketones," *Journal of Physical Chemistry* 100:11360–11367, 1996.
- [48] Kikuchi, K., Sato, C., Watabe, M., Ikeda, H., Takafashi, Y., Miyashi, T., "New aspects on fluorescence quenching by molecular oxygen," *Journal of the American Chemical Society* 115:5180–5184, 1993.
- [49] Yip, B., Lozano, A., and Hanson, R.K., "Sensitized phosphorescence: a gas phase molecular mixing diagnostic," *Experiments in Fluids* 17:16–23, 1994.
- [50] Andersson, M., Warnberg, J., Hemdal, S., Dahlander, P., Denbratt, I., "Evaporation of Gasoline-Like and Ethanol-Based Fuels in Hollow-Cone Sprays Investigated by Planar Laser-Induced Fluorescence and Mie Scattering," *SAE Technical Paper Series* 2011-01-1889, 2011.
- [51] Ma, X., He, X., Wang, J.-x., and Shuai, S., "Co-evaporative multi-component fuel design for in-cylinder PLIF measurement and application in gasoline direct injection research," *Applied Energy* 88:2617–2627, 2011.
- [52] van Romunde, Z., Aleiferis, P. G., Cracknell, R. F., and Walmsley, H. L., "Effect of Fuel Properties on Spray Development from a Multi-Hole DISI Engine Injector," *SAE Technical Paper Series* 2007-01-4032, 2007.
- [53] VanDerWege, Brad A. and Hochgreb, S., "Effects of Fuel Volatility and Operating Conditions on Fuel Sprays in DISI Engines: (1) Imaging Investigation," *SAE Technical Paper Series* 2000-01-0535, 2000.
- [54] Bruneaux, G., "Mixing Process in High Pressure Diesel Jets by Normalized Laser Induced Exciplex Fluorescence Part I: Free Jet," *SAE Technical Paper Series* 2005-01-2100, 2005.
- [55] Ossler, F. and Aldén, M., "Measurements of picosecond laser induced fluorescence from gas phase 3-pentanone and acetone: Implications to combustion diagnostics," *Applied Physics B* 64:493–502, 1997.

- [56] Orain, M., Baranger, P., Rossow, B., and Grisch, F., "Fluorescence spectroscopy of 1,2,4-trimethylbenzene at high temperatures and pressures: Application to temperature measurements," *Applied Physics B* 100:945–952, 2010.
- [57] Zabeti, S., Drakon, A., Faust, S., Dreier, T., Welz, O., Fikri, M., Schulz, C., "Temporally and spectrally resolved UV absorption and laser-induced fluorescence measurements during the pyrolysis of toluene behind reflected shock waves," *Applied Physics B* 118:295–307, 2014.
- [58] Tea, G., "Development and exploitation of optical diagnostic techniques for simultaneous 2D temperature and equivalence ratio measurements for the understanding of combustion phenomena in reciprocating engine," PhD thesis, University of Duisburg-Essen, 2014.
- [59] Settersten, T.B., Dreizler, A., and Farrow, R.L., "Temperature- and species-dependent quenching of CO B probed by two-photon laser-induced fluorescence using a picosecond laser," *Journal of Chemical Physics* 117:3173–3179, 2002.
- [60] Koban, W., Koch, J.D., Hanson, R.K., and Schulz, C., "Oxygen quenching of toluene fluorescence at elevated temperatures," *Applied Physics B* 80:777–784, 2005.
- [61] Otis, C.E., Knee, J.L., and Johnson, P.M., "The identification of channel three in isolated benzene," *Journal of Chemical Physics* 78:2091–2092, 1983.
- [62] Luong, M., Koban, W., and Schulz, C., "Novel strategies for imaging temperature distribution using Toluene LIF," *Journal of Physics: Conference Series* 45:133–139, 2006.
- [63] Engine Combustion Network, "Spray G Operating Condition," Last update, December 3, 2014, <http://www.sandia.gov/ecn/G/targetCondition/sprayG.php>.
- [64] Bardi, M., Payri, R., Malbec, L.M., Bruneaux, G., Pickett, L.M., Manin, J., Bazyn, T., Genzale, C.L., "Engine combustion network: Comparison of spray development, vaporization, and combustion in different combustion vessels," *Atomization and Sprays* 22:807–842, 2012.
- [65] Fansler, T.D., Reuss, D.L., Sick, V., and Dahms, R.N., "Combustion instability in spray-guided stratified-charge engines: A review," *International Journal of Engine Research* 16:260–305, 2015.

- [66] Marchi, A., Nouri, J., Yan, Y., and Arcoumanis, C., "Spray stability of outwards opening pintle injectors for stratified direct injection spark ignition engine operation," *International Journal of Engine Research* 11:413–437, 2010.
- [67] Zhang, M., and, M.X., S, D.L., Xu, M., "Simultaneous two-phase flow measurement of spray mixing process by means of high-speed two-color PIV," *Measurement Science and Technology* 25:095204, 2014.
- [68] Holderbaum, T. and Gmehling, J., "PSRK: A Group Contribution Equation of State Based on UNIFAC," *Fluid Phase Equilibria* 70:251–265, 1991.
- [69] Faust, S., Tea, G., Dreier, T., and Schulz, C., "Temperature, pressure, and bath gas composition dependence of fluorescence spectra and fluorescence lifetimes of toluene and naphthalene," *Appl. Phys. B* 110:81-93, 2013.
- [70] Blessinger, M., Manin, J., Skeen, S., Meijer, M., Parrish, S., Pickett, L.M., "Quantitative mixing measurements and stochastic variability of a vaporizing gasoline direct-injection spray," *International Journal of Engine Research* 16:238–252, 2015.
- [71] Pickett, L.M., Genzale, C.L., Bruneaux, G., Malbec, L.-M., Hermant, L., Christiansen, C., Sschramm, J., "Comparison of diesel spray combustion in different high-temperature, high-pressure facilities," *SAE International Journal of Engines* 3:156–181, 2010.
- [72] Espey, C., Dec, J.E., Litzinger, T.A., and Santavicca, D.A., "Planar laser Rayleigh scattering for quantitative vapor-fuel imaging in a diesel jet," *Combustion and Flame* 109:65–86, 1997.
- [73] Tea, G., Bruneaux, G., Kashdan, J., and Schulz, C., "Unburned gas temperature measurements in a surrogate Diesel jet via two-color toluene-LIF imaging," *Proceedings of the Combustion Institute* 33:783–790, 2011.
- [74] Moffat, R.J., "Describing the uncertainties in experimental results," *Experimental Thermal and Fluid Science* 1:3–17, 1988.
- [75] Bjorn Rossow, Federic Grisch, "Photophysical measurements of p-difluorobenzene and 1-methylnaphthalene,"
- [76] Schmid, A., Schneider, B., Boulouchos, K., and Wigley, G., "Experimental investigations on a piezo-activated hollowcone injector - Part I: Measurement of needle lift and its influence on spray morphology," *Atomization and Sprays* 24:841–857, 2014.

- [77] Schmid, A., Schneider, B., Boulouchos, K., and Wigley, G., "Experimental investigations on a piezo-activated hollowcone injector - Part II: The influence of needle lift on droplet size distributions and vortex formation," *Atomization and Sprays* 24:859–871, 2014.
- [78] Itani, L.M., Bruneaux, G., Di Lella, A., and Schulz, C., "Two-tracer LIF imaging of preferential evaporation of multi-component gasoline fuel sprays under engine conditions," *Proceedings of the Combustion Institute* 35:2915–2922, 2015.
- [79] Fansler, T.D., Parrish, S.E., "Spray measurement technology: A review," *Measurement Science and Technology* 26: 012002, 2015.

